Title
Mature retina is resilient to profound input loss

Author
Care, Rachel

Publication Date
2019

Peer reviewed|Thesis/dissertation

Mature retina is resilient to profound input loss

by
Rachel Care

DISSERTATION
Submitted in partial satisfaction of the requirements for degree of
DOCTOR OF PHILOSOPHY

in

Neuroscience

in the

GRADUATE DIVISION
of the
UNIVERSITY OF CALIFORNIA, SAN FRANCISCO

Approved:

DocuSigned by:
Michael P. Stryker
6F464CB16FDD412...

Michael P. Stryker
Chair

DocuSigned by:
David R. Copenhagen
D42F5D2E42...

David R. Copenhagen

DocuSigned by:
Jonathan C. Horton
DA4E5BA672...

Jonathan C. Horton

DocuSigned by:
Felice A. Dunn
6A844AAC58D5405...

Felice A. Dunn

Committee Members

DEDICATION

This dissertation is dedicated to Felice A. Dunn, my thesis advisor.

Felice's impact on my life is immeasurable and all I have to offer her is this work.

CONTRIBUTIONS

The work presented in Chapter 1 of this dissertation is a reprint of the material as it appears in:

Care RA, Kastner DB, De la Huerta I, Pan S, Khoche A, Della Santina L, Gamlin C, Santo Thomas C, Ngo J, Chen A, Kuo YM, Ou Y, Dunn FA (2019). Partial cone loss triggers synapse-specific remodeling and spatial receptive field rearrangements in a mature retinal circuit. *Cell Reports,* 27, 2171–2183.e5.

The work presented in Chapter 2 of this dissertation has been prepared in the following manuscript:

Care RA, Anastassov IA, Della Santina L, Kuo YM, Dunn FA. Mature retina compensates functionally for partial loss of rod photoreceptors. *In preparation.*

As primary author, Rachel Care has contributed the majority of the work in these manuscripts including: experimental design, execution of experiments, analysis, visualization, writing, and editing. No other author in the listed publication contributed to all aspects of the project. This work has been approved by the thesis committee as satisfying and exceeding the expectations for a standard dissertation.

Mature retina is resilient to profound input loss

Rachel Care

ABSTRACT

The full or partial deafferentation of neural circuits is an inevitability in the life of an organism. The mature nervous system is thus tasked with maintaining a stable output in the face of lost input. Deafferentation has been studied in numerous sensory systems, but nowhere is the problem so well defined and controllable as in the visual system. Despite a deep literature on deafferentation in visual cortex, it remains unknown how the retina contributes to this plasticity. In this dissertation, I show that the mature retinal circuit compensates for input lost after half of either the cone or rod photoreceptors have been ablated. In Chapter 1, I demonstrate that after loss of half of the cone population, functional compensation arises via inhibitory currents onto ganglion cells. In Chapter 2, I demonstrate that after loss of half of the rod population, functional compensation arises via inhibitory currents onto rod bipolar cells. In both studies, I examine morphology and physiology and use partial stimulation of control retina to dissociate response properties resulting from decreased input and response properties resulting from subsequent plasticity within the circuit. In Chapter 3, I discuss principles that emerge from comparing these two studies and how these results may inform current efforts to develop diagnostic tools and therapies to restore vision.

TABLE OF CONTENTS

LIST OF FIGURES

LIST OF TABLES

CHAPTER 1: PARTIAL CONE LOSS TRIGGERS SYNAPSE-SPECIFIC REMODELING AND SPATIAL RECEPTIVE FIELD REARRANGEMENTS IN A MATURE RETINAL CIRCUIT

Summary

Resilience of neural circuits has been observed in the persistence of function despite neuronal loss. In vision, acuity and sensitivity can be retained after 50% loss of cones. While neurons in cortex can remodel after input loss, the contributions of cell-type specific circuits to resilience are unknown. Here, we study the effects of partial cone loss in mature mouse retina where cell types and connections are known. At first-order synapses, bipolar cell dendrites remodel and synaptic proteins diminish at sites of input loss. Sites of remaining inputs preserve synaptic proteins. Second-order synapses between bipolar and ganglion cells remain stable. Functionally, ganglion cell spatio-temporal receptive fields retain center-surround structure following partial cone loss. We find evidence for slower temporal filters and expanded receptive field surrounds, derived mainly from inhibitory inputs. Surround expansion is absent in partially-stimulated control retina. Results demonstrate functional resilience to input loss beyond pre-existing mechanisms in control retina.

Introduction

Loss of neuronal input can occur in injury, degenerative disease, and aging. The consequences of such loss are often not functionally perceived. For example, it has been estimated that Parkinson's patients can lose 70% of dopaminergic neurons before showing clinical signs (Naoi and Maruyama, 1999). Similarly, live imaging of cone photoreceptors in human retina coupled with psychophysical examination suggests that visual acuity and sensitivity are minimally compromised even following loss of 50% of the cone population (Ratnam et al., 2013). It is unclear what contributes to behavioral resilience to input loss. Either or both of the following possibilities could contribute: the sensory circuit has pre-existing mechanisms, e.g., highly overlapping circuits or adaptation, built in to withstand partial input loss and/or has *de novo* mechanisms that react to input loss (Keck et al., 2008; 2011; 2013). Distinguishing between these possibilities requires a system with access to well-defined sensory circuits and precise control over input loss.

Such a well-defined circuit can be found in the central nervous system's retina, where specific types of photoreceptors, bipolar cells, and ganglion cells connect in sequence. In the retina, previous models of photoreceptor disease consist of genetic insults that disrupt function during development or physical ablation that destroys spatially contiguous populations of photoreceptors (Strettoi et al., 2002; 2003; Haverkamp et al., 2006; Sher et al., 2013; Vessey et al., 2014). However, in diseases such as age-related macular degeneration, photoreceptor cell loss often starts during adulthood and is initially sparse (Zayit-Soudry et al., 2013).

Here we use transgenic mouse lines that selectively express the diphtheria toxin receptor in cones, allowing for temporal control of ablation mediated by diphtheria toxin. We ablated subsets of cones, allowing us to assess the retina's potential for modifying existing synapses and/or making new

synapses with the remaining cones. We then examined the effects of this limited cone loss on the morphology of well-characterized connections from the cones to the type 6 ON cone bipolar cells to their major postsynaptic partners, the alpha ON-sustained ganglion cells ($A_{ON\text{-}S}$). At the level of bipolar cells, we examined input (first order) and output (second order) synapses to identify sites of resilience to cone loss. At the level of ganglion cells, we examined morphological and functional resilience. We find that type 6 bipolar cell dendrites remodel following cone death in mature retina; however, the number of output synapses in the bipolar cell is invariant to input loss. Despite this structural stability, we uncovered functional changes in ganglion cell spatio-temporal receptive fields. With diminished cone inputs, $A_{ON\text{-}S}$ exhibit slower temporal filters and wider receptive field surrounds. Changes to the spatial receptive field are distinct from partial stimulation of control retina, suggesting *de novo* changes within the retinal circuit following cone loss. This study provides the evidence for resilience within mature retina that could explain the lack of functional deficit associated with partial cone loss.

Results

Selective ablation of majority of cones in adult mouse retina within three days

To ablate the presynaptic cone population after development of the retina, we injected diphtheria toxin (DT) intramuscularly at postnatal day 30 in diphtheria toxin receptor (DTR)-positive and DTR-negative control animals (Figure 1.1A). We observed retinas at 3 to 60 days following diphtheria toxin injection (Figure 1.1B). Cone death was complete within three days and no further cone loss was observed up to 60 days after DT injection (Figure S1.1F). This rapid reduction in cone density is consistent with the mechanism of diphtheria toxin, which initiates apoptosis within three days (Buch et al., 2005). We used two mouse lines throughout our study: the *OPN1SW-Cre* line

expresses Cre-recombinase under the S-opsin promoter and the *OPN1MW-Cre* line expresses Cre-recombinase under the M-opsin promoter (Akimoto, 2004; Le et al., 2004). Because most mouse cones co-express both S- and M-opsin (Applebury et al., 2000), both Cre lines target a large population of cones that express both S- and M-opsin (Figure S1.1A-E). Variability in efficacy of injection and expression of DTR caused a range of cone loss (Figure 1.1C, D). Throughout the study we found no significant differences between results from the *OPN1SW-Cre x DTR* and *OPN1MW-Cre x DTR* lines, and so we have combined the results and refer to them as *DTR*. Despite the dorsal-ventral gradient of S- and M-opsin expression in the mouse retina, we found no significant difference in surviving cone density between dorsal and ventral regions after DT injection (dorsal: 5320±3080, n=14; ventral 5199±2592 cones/mm^2, n=42; median±interquartile range (IQR), p=0.36, rank sum). The cone densities in control animals are comparable to previous reports of mouse cone density (Jeon et al., 1998).

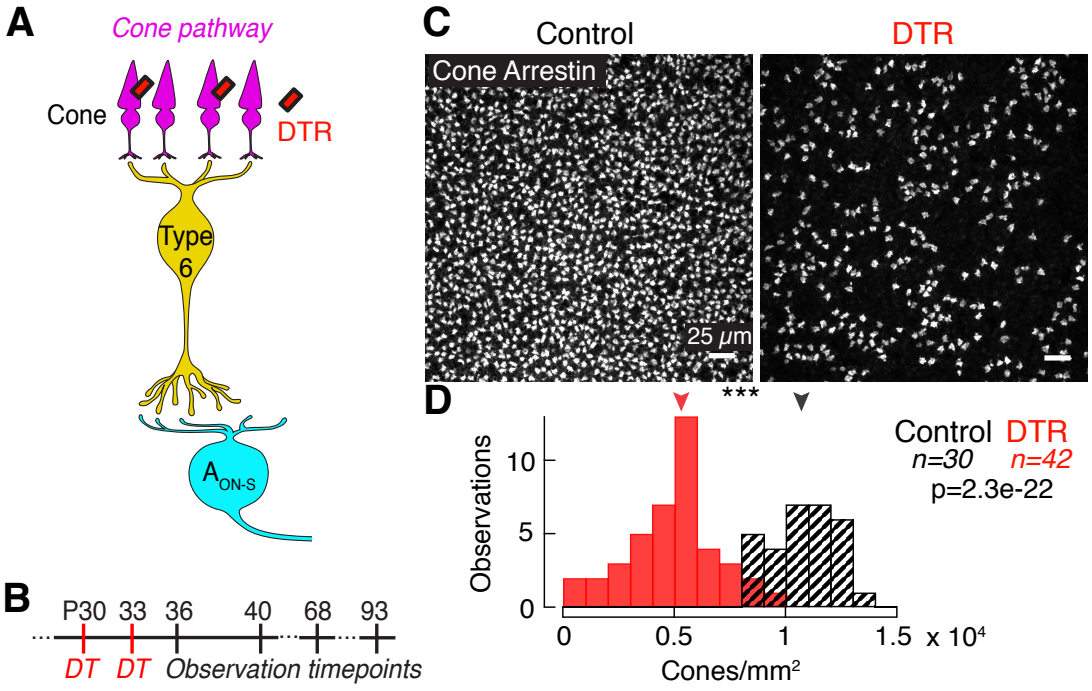

Figure 1.1. Diphtheria toxin receptor system ablates the majority of cones in the mature mouse retina.
(A) Schematic of the direct cone pathway (magenta): cones → type 6 ON cone bipolar cell → $A_{ON\text{-}S}$ ganglion cell. Color of the cells in the cone pathway are consistent with colors used in latter figures. The diphtheria toxin receptor (DTR) is expressed in a subset of cones driven under either the promoter for short- or middle-wavelength opsin (see Figure S1.1).
(B) Timeline of experiments indicating diphtheria toxin (DT) injections and observation timepoints in postnatal (P) days. The time points were chosen to capture early responses to cone death before gross retinal remodeling previously observed at >3 months following photoreceptor loss (see Figure S1.2, Table S1.1).
(C) Confocal images of the cone pedicles labeled by immunostaining for cone arrestin in control and DTR conditions in ventral retina.
(D) Histogram of cone densities in control and DTR conditions across all intervals between diphtheria toxin injection and quantification. Arrowheads indicate median of each population. Asterisks indicate significance (see Results). See also Figures S1.1, S1.2, Table S1.1.

To determine whether other retinal cell types were affected by DT injection, we quantified populations of retinal cells. We found no reduction in the rod population after partial cone loss (Figure S1.1I, Q-T). We also found no reduction in the amacrine and bipolar cell populations in the inner nuclear layer (Figure S1.1T), nor in populations of horizontal cells, ganglion cells, microglia and Müller glia (Figure S1.2, Table S1.1). Partial cone loss did not activate microglia or Müller glia as determined by absence of the protein Cluster of Differentiation 68 (CD68) and glial fibrillary acidic protein (GFAP; data not shown). Together, these results demonstrate that our diphtheria toxin system eliminates a majority of cones regardless of their opsin expression within three days after toxin injection, while sparing other retinal cell types. We leveraged this system to examine structural and functional changes in a well-defined microcircuit following acute cone loss.

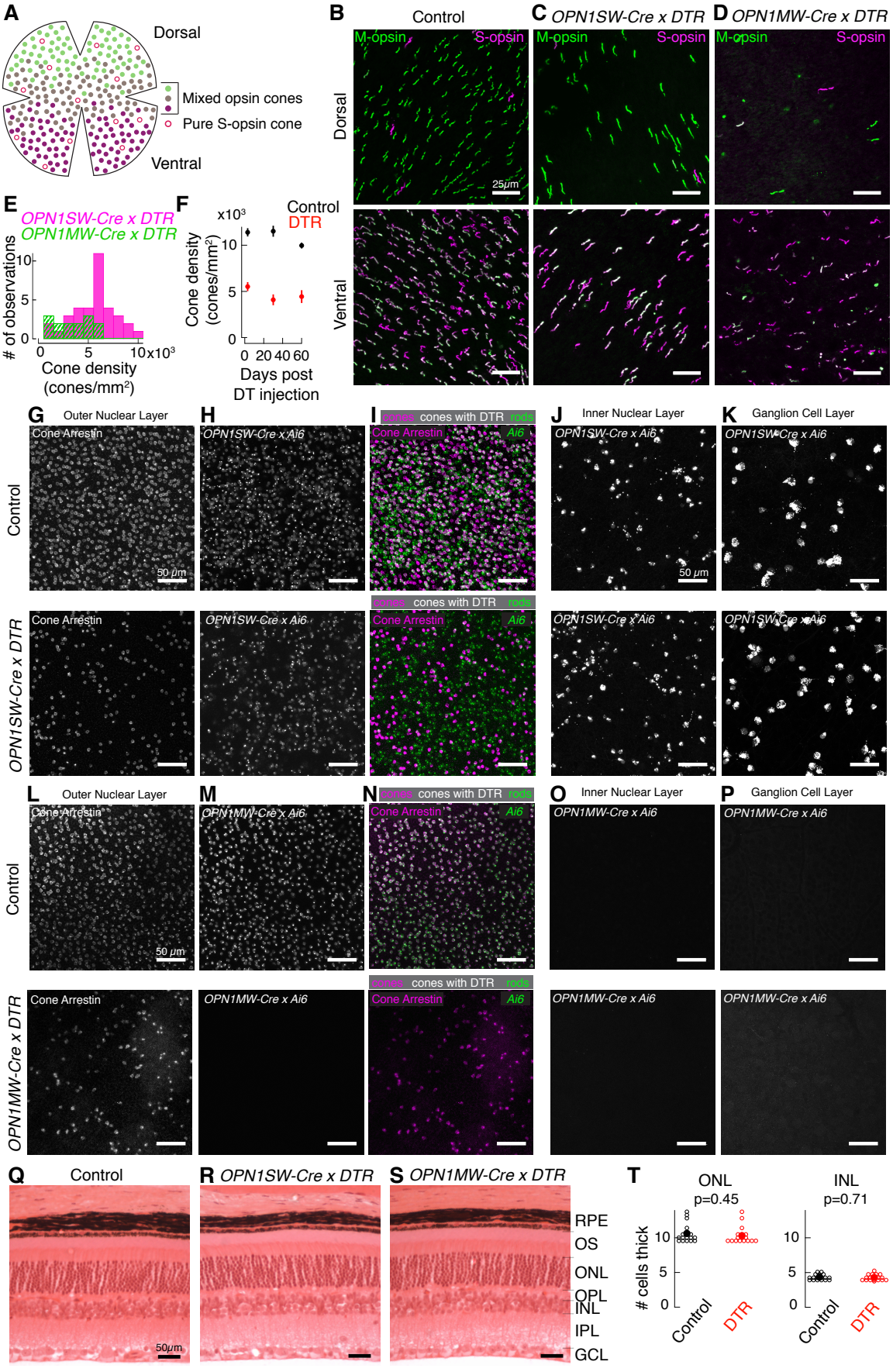
A
Dorsal
Mixed opsin cones
Pure S-opsin cone
Ventral
B Control
C OPN1SW-Cre x DTR
D OPN1MW-Cre x DTR
M-opsin
S-opsin
Dorsal
Ventral
25μm
E
OPN1SW-Cre x DTR
OPN1MW-Cre x DTR
# of observations
Cone density (cones/mm²)
F
Control
DTR
Cone density (cones/mm²)
Days post DT injection
G Outer Nuclear Layer
H
I
J Inner Nuclear Layer
K Ganglion Cell Layer
Control
OPN1SW-Cre x DTR
Cone Arrestin
OPN1SW-Cre x Ai6
cones with DTR
Ai6
50 μm
L Outer Nuclear Layer
M
N
O Inner Nuclear Layer
P Ganglion Cell Layer
OPN1MW-Cre x DTR
OPN1MW-Cre x Ai6
Q Control
R OPN1SW-Cre x DTR
S OPN1MW-Cre x DTR
50μm
RPE
OS
ONL
OPL
INL
IPL
GCL
T
ONL
p=0.45
INL
p=0.71
# cells thick
Control
DTR

Figure S1.1. Diphtheria toxin system does not significantly affect other retinal cell types. Related to Figure 1.1.

(A) Schematic of the cone opsin distribution in mice in which middle wavelength (M) opsin is rich in dorsal retina (green), short wavelength (S) opsin is rich in ventral retina (magenta), and mixed opsins are found throughout retina.

(B-D) Confocal images of cone outer segments labeled in dorsal (top) and ventral (bottom) regions by the M opsin antibody (green) and S opsin antibody (magenta) in (B) control, (C) *OPN1SW-Cre x DTR*, and (D) *OPN1MW-Cre x DTR* retina. Both DTR lines spare cones with M and S opsin as shown by the persistence of cones containing M and S opsins.

(E) Histogram of cone density in *OPN1SW-Cre x DTR* (magenta) and *OPN1MW-Cre x DTR* (green) retina after DT injection. OPN1SW n = 35 retinas; OPN1MW n = 14 retinas.

(F) Cone density in control and DTR retina as a function of time since DT injection. One-way ANOVA was used to test for differences in cone density across intervals: Control $F(2, 31)=2.57$, $p=0.09$; DTR $F(2, 31)=1.2$, $p=0.32$.

(G-K) Confocal images of cell somas in the indicated layer from the *OPN1SW-Cre x Ai6* mouse line. (G) Cone somas labeled by cone arrestin in the outer nuclear layer. (H) Cone and rod somas that express Ai6 fluorescence. (I) Overlay of cone arrestin (magenta) and Ai6 fluorescence (green). Cones labeled with cone arrestin and not expressing Ai6 are magenta, cones labeled with cone arrestin and expressing Ai6 are white, and rods expressing Ai6 are green. Cones expressing Ai6 (white) are numerous in control retina (top row) and diminish in DTR retina (bottom row) after DT administration, while photoreceptors not expressing Ai6 (cones = magenta; rods = green) are unaffected by DT administration.

(J,K) Maximum intensity projections of the (J) inner nuclear layer and (K) ganglion cell layer show that Ai6 fluorescence in bipolar and amacrine cells (J) and displaced amacrine cells and ganglion cells (K) does not decrease after DT administration, indicating that these cell populations survive our dosage of DT.

(L-P) Confocal images of cell somas in the indicated layer from the *OPN1MW-Cre x Ai6* mouse line. (L) Cone somas labeled by cone arrestin in the outer nuclear layer. Cones remain in DTR retina (bottom row). (M) Cone somas that express Ai6 fluorescence. (N) Overlay of cone arrestin (magenta) and Ai6 fluorescence (green). Most cones express Ai6 (white, top), and no rods express Ai6 (absence of green). Cones expressing Ai6 (white) are numerous in control retina (top row) and completely killed in DTR retina (bottom row).

(O,P) Maximum intensity projections of the (O) inner nuclear layer and (P) ganglion cell layer show no Ai6 fluorescence in bipolar and amacrine cells (O) nor in displaced amacrine cells and ganglion cells (P). Retinal location was determined by Syt2 and SMI-32 staining.

(Q-S) Plastic sections from (Q) control, (R) *OPN1SW x DTR*, (S) *OPN1MW-Cre x DTR* retina. Sections stained with Hematoxylin and Eosin. Layers of the retina are labeled on the right: RPE = retinal pigment epithelium, OS = outer segments, ONL = outer nuclear layer containing 97% rod cell bodies and 3% cone cell bodies (Jeon et al., 1998), OPL = outer plexiform layer, INL = inner nuclear layer containing bipolar cell and amacrine cell bodies, IPL = inner plexiform layer, and GCL = ganglion cell layer.

(T) Quantification of number of cell bodies in each column of the OPL and INL in retinal sections cut close to the optic nerve head. Quantification taken at multiple locations within and across retinal

sections. No significant difference in the number of photoreceptor cell bodies in ONL nor in the number of bipolar and amacrine cell bodies in the INL between control and DTR retinas (rank sum).

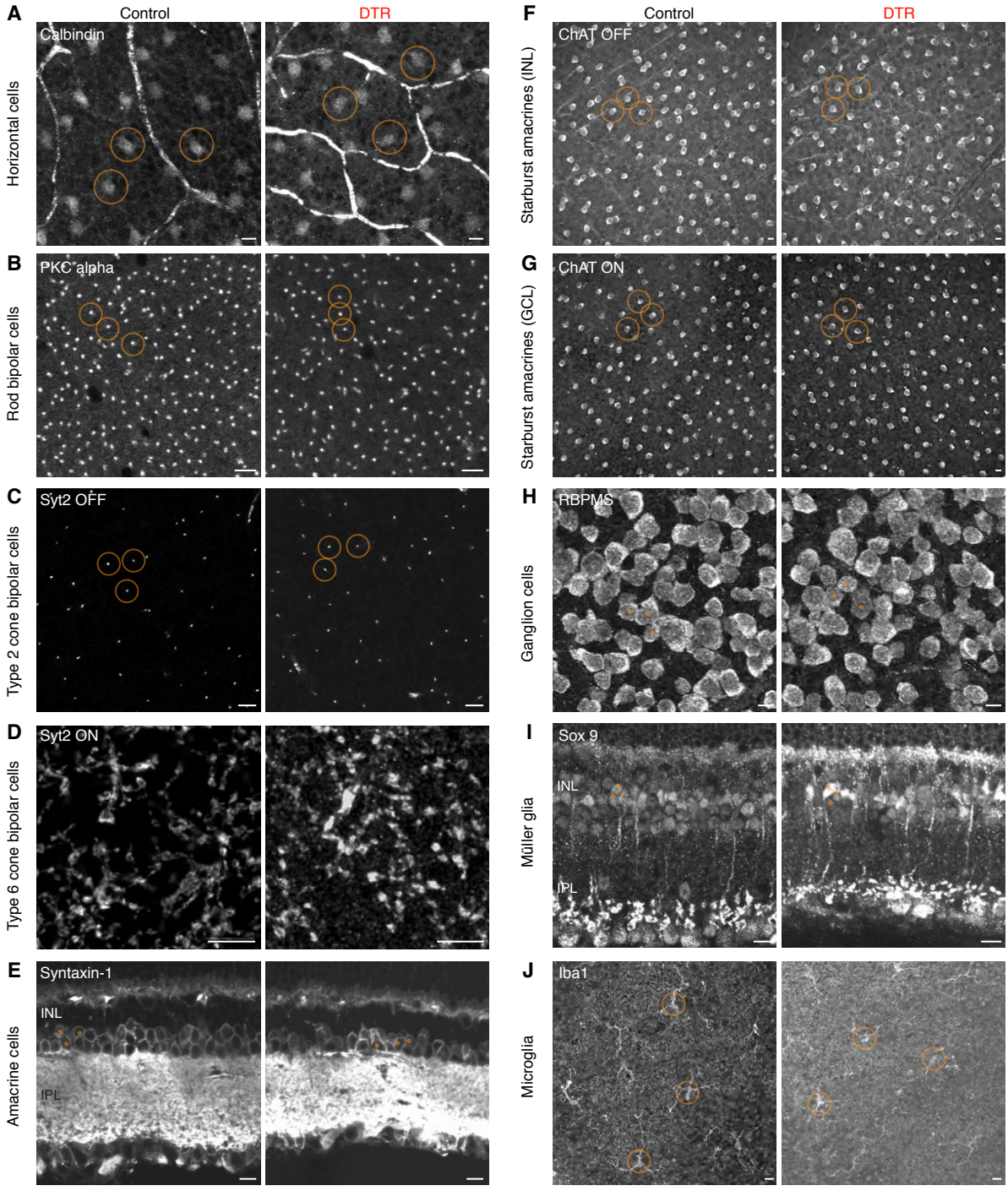

Figure S1.2. Effects of the diphtheria toxin system on non-cone retinal cell types. Related to Figure 1.1.

Example images of cell types under control and DTR conditions. When labeling was quantified, images show 3 examples of counts either by orange circles or dots. Quantification was done on areas larger than shown images (Table S1.1).

(A) Horizontal cell somas labeled by calbindin in flat mount.

(B) Rod bipolar cell axons stalks labeled by PKC alpha in flat mount.

(C) Type 2 OFF cone bipolar cell axon stalks labeled by Syt2 in flat mount.

(D) Type 6 ON cone bipolar cell axons labeled by Syt2 in flat mount. Syt2 labeling was variable between retinas and did not label the axon stalk and hence was not quantified.

(E) Amacrine cell somas labeled by syntaxin-1 in sections.

(F) Starburst amacrine cell somas in the inner nuclear layer (INL) labeled by ChAT in flat mount.

(G) Starburst amacrine cell somas in the ganglion cell layer (GCL) labeled by ChAT in flat mount.

(H) Ganglion cell somas labeled by RBPMS in flat mount.

(I) Müller glia labeled by Sox 9 in sections.

(J) Microglia labeled by Iba1 at the level of the OPL in flat mount. All scale bars = 10μm.

Table S1.1. Effects of the diphtheria toxin system on the densities of non-cone retinal cell types. Related to Figure 1.1.

Cell Type	Methods: antibody, retinal layer imaged, flat mount or section, retinal topography	Control Density (median±IQR)	DTR Density (median±IQR)	n = images for control (& DTR) N = mice for control (& DTR)	Rank sum test p-value
Horizontal cells	Calbindin, ONL, flat mount, dorsal-nasal	1011.7±372.7 cells/mm^2	842.0±83.2 cells/mm^2	n = 6 (4) N = 3 (2)	p = 0.17
Rod bipolar cells	PKCalpha, IPL, flat mount, dorsal-nasal	16474±2127 cells/mm^2	15146±945 cells/mm^2	n = 8 (6) N = 3 (3)	p = 0.23
Type 2 OFF cone bipolar cells	Syt2, IPL, flat mount, dorsal-nasal	2983.6±189.8 cells/mm^2	2630.6±279.7 cells/mm^2	n = 4 (6) N = 2 (3)	p = 0.019
Amacrine cells	Syntaxin-1, INL, sections	280.0±59.8 cells/mm	278.8±54.0 cells/mm	n = 4 (4) N = 2 (2)	p = 0.69
Starburst amacrine cells (OFF)	ChAT, INL, flat mount, dorsal-nasal	1202.1±163.2 cells/mm^2	1168.8±326.3 cells/mm^2	n = 4 (6) N = 2 (3)	p = 0.50
Starburst amacrine cells (ON)	ChAT, GCL, flat mount, dorsal-nasal	1142.1±183.1 cells/mm^2	1092.2±166.5 cells/mm^2	n = 4 (6) N = 2 (3)	p = 0.50
Ganglion cells	RBPMS, GCL, flat mount, dorsal-nasal	3346.5±978.0 cells/mm^2	2967.3±1403.8 cells/mm^2	n = 7 (6) N = 3 (3)	p = 0.73
Muller glia	Sox9, INL, sections	414.2±62.7 cells/mm	246.5±164.0 cells/mm	n = 4 (4) N = 2 (2)	p = 0.06
Microglia	Iba1, OPL, flat mount, dorsal-nasal	103.2±23.2 cells/mm	109.9±10.0 cells/mm	n = 4 (4) N = 2 (2)	p = 0.83

First-order synapse: Type 6 cone bipolar cell dendrites do not require a cone for stability

Previous work provides evidence that developing postsynaptic dendrites sprout in the absence of the dominant presynaptic partner (Haverkamp et al., 2006; Michalakis et al., 2012). To examine the impact of presynaptic partner loss on postsynaptic dendritic morphology in the mature retina, we measured the number of primary dendrites and cone contacts in bipolar cells. We took advantage of the type 6 bipolar cell's stereotyped morphology and simple connectivity pattern of receiving input from the four nearest cones, regardless of opsin expression (Dunn and Wong, 2012). Isolated type 6 bipolar cells were visualized in the *Grm6-TdTomato* line (Kerschensteiner et al., 2009). After determining that bipolar cells were unaffected by DT injection (Figure S1.1), we were able to identify type 6 bipolar cells in control and DTR retina by their axon terminals, which co-localize with the innermost band of Syt2 labeling (Figure 1.2A; Wässle et al., 2009).

We imaged type 6 bipolar cell dendrites (Figure 1.2B) and the cones within their dendritic fields (Figure 1.2C-D). No differences were observed between the shortest and longest time points, so the data were pooled (number of primary dendrites in DTR retina for 5 days vs. 60 days: 3.0±2.0 vs. 3.0±1.5 dendrites, median±IQR, p=0.46, rank sum; length of primary dendrites in DTR retina for 5 days vs. 60 days: 10.03±5.13 vs. 10.34±5.35µm, median±IQR, p=0.89, rank sum). We identified synaptic contact between bipolar cell dendrites and cones by volume overlap (Figure 1.2D-E). While type 6 bipolar cells in control retina had 4±1 cone contacts (*n*=44 bipolar cells), after cone loss, type 6 bipolar cell dendrites in DTR retina contacted 2±1 cones (*n*=76 bipolar cells) (median±IQR, p=2.78e-10, rank sum). This reduction in cone contacts by half is in accordance with the cone death we induced and suggests that most type 6 bipolar cells do not make new cone contacts to replace those lost.

To understand how dendrites respond to loss of cone contacts, we counted the number of dendrites per type 6 (Figure 1.2F). Dendrites at least 1 μm long off the soma were considered primary dendrites. After cone loss, the number of primary dendrites is maintained (Control 3±1, n=44; DTR 3±2 primary dendrites, n=76; median±IQR, p=0.99, rank sum), despite the decrease in cone contacts. Representative images of dendrites remaining without cone contacts are shown in Figure 1.2B-D, and dendrites without cone contacts were present even 60 days after cone loss (not shown). These data indicate that cone input is not required for a dendrite to persist.

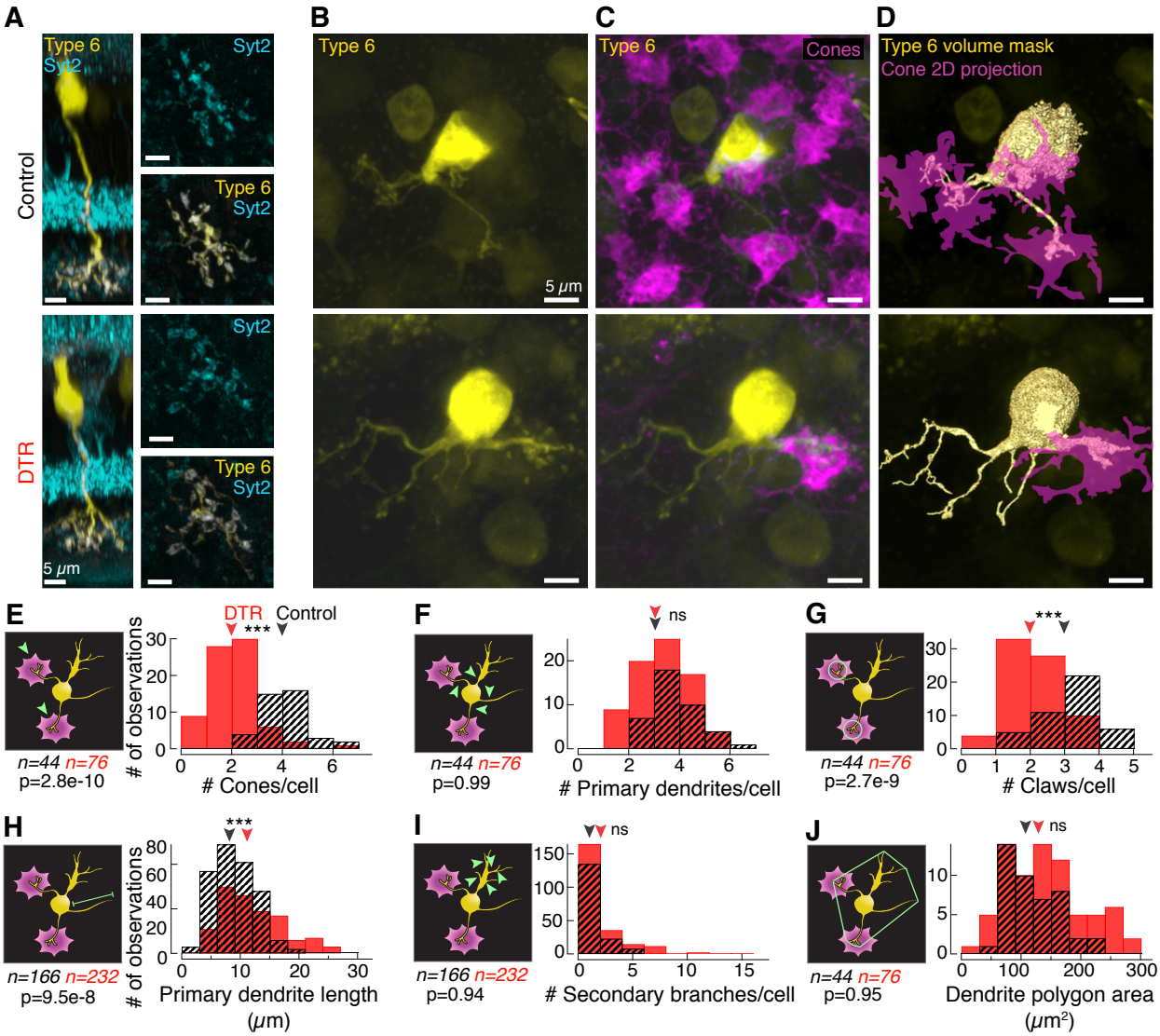

Figure 1.2. At the first-order synapse, postsynaptic type 6 cone bipolar cell dendrites remodel after cone loss in mature retina.
(A) Confocal images of type 6 cone bipolar cells labeled in the transgenic *Grm6-TdTomato* line. Side views of the isolated type 6 bipolar cells with Syt2 labeling of the type 2 and 6 bipolar cell axons. (right) *En face* views of the bipolar cell axon terminal showing overlap with Syt2 within the axon in control (top) and DTR (bottom) retina.
(B, C) *En face* views of the type 6 cone bipolar cell (B) dendrites alone and (C) with cone pedicles labeled by cone arrestin in control (top) and DTR (bottom) retina.
(D) Rendered images of the type 6 bipolar cell dendrites (yellow) and associated cone pedicles (magenta). Such binary images of the bipolar cell dendrites and cones were used to determine volume overlap between the two structures.
(E-J) Histograms of (E) the number of cones that each type 6 bipolar cell contacts as determined by nonzero volume overlap between bipolar cell dendrites and cones; (F) the number of primary dendrites branching directly off the bipolar cell soma; (G) the number of claws per bipolar cell, defined by >3 secondary branches within a 10μm diameter circle; (H) the length of primary dendrites from the soma to the longest dendritic tip; (I) the number of ≥ secondary branches coming from a primary branch that are not part of a claw structure; (J) the area of the polygon drawn around the vertices of the dendritic tips. Arrowheads point to median. Asterisks indicate significance (see Results). Measurement examined is indicated on the schematic in green (left of each histogram). In the control condition, claws were seldom found without a cone contact. In the DTR condition, claws existed at terminals both with and without a cone contact. We cannot distinguish whether the claws in the absence of cones linger from previous cone contacts or are newly formed claws. Data combined across time points because there was no significant difference between shortest and longest time points (see Results). Number of samples (*n*) and p value for rank sum test noted in each panel.

First-order synapse: Remaining type 6 cone bipolar dendrites extend and lose terminal morphology

While dendrites in the developing retina exhibit remodeling after input loss, no reports have been made of remodeling in mature cone bipolar cells. To determine how dendrite morphology was influenced by cone loss in adulthood, we quantified the presence of specialized dendritic terminals, the length of primary dendrites, and dendritic complexity.

Most type 6 bipolar cell dendrites in control retina contact cones via specialized terminals, i.e. claws. The number of claws per bipolar cell was significantly less in DTR retina compared to control retina

(Figure 1.2G; Control: 3±1; DTR: 2±1 claws; median±IQR, p=2.73e-9, rank sum). These results suggest that claw loss follows cone loss and is evidence of remodeling. However, the diameters of remaining claws were not different from control, which indicates that remaining claws do not expand their synaptic contact area (Control: 3.3±4.2; DTR: 2.7±4.9μm; median±IQR, p=0.56, rank sum). The next indicator of remodeling was primary dendritic length. In DTR retina, dendrite lengths extended significantly beyond those from control retina (Figure 1.2H; Control: 8.7±8.0, *n*=166 dendrites; DTR: 11.4±5.2μm, *n*=232 dendrites; median±IQR, p=9.5e-8, rank sum). The longest branch lengths were associated with branches terminating in cone contacts. Such results suggest that either new contacts were made with cones outside of the bipolar cell's original dendritic field or that dendrites with existing cone contacts extended to follow cones that may have translocated in the sparser cone mosaic.

From each primary dendrite, we quantified the branches of secondary order or greater, excluding those within a claw. We found no significant difference in branching patterns (Figure 1.2I; Control: 0±1; DTR: 1±2 branches; median±IQR, p=0.94, rank sum). Similarly, we found no change in the dendritic territories (Figure 1.2J; Control: 113.9±69; DTR: 137.5±97μm^2; median±IQR, p=0.95, rank sum). Such results suggest that the complexity and area of bipolar cell dendritic branches is maintained in the face of cone loss.

Across our morphological measurements, we find that type 6 bipolar cells remodel dendrites to dismantle terminal specializations that have lost cone partners while extending primary dendrites, potentially in search of new synaptic cone partners. Taken together, these results show that type 6 cone bipolar cells in the mature retina are capable of remodeling, but that within 60 days, this remodeling does not compensate for the number of lost cone inputs.

First-order synapse: Postsynaptic glutamate receptors are localized to cone contacts after partial cone loss

To understand whether these remodeled bipolar cell dendrites contain the appropriate synaptic machinery for functional connectivity, we next investigated how the glutamate receptor localization changes in these type 6 bipolar cells following cone ablation. We immunostained for the postsynaptic metabotropic glutamate receptor 6 (mGluR6) and measured fluorescence intensity along line segments that followed primary dendrites from the dendritic base (next to soma) to tip (Figures 1.3A lines, 3B). We normalized this distance and plotted the location of the peak mGluR6 fluorescence to compare across cells (Figure 1.3C). For both control and DTR conditions with cone contacts, peak mGluR6 fluorescence was found in the distal quarter of the dendrite, towards the synapse (Figure 1.3B, C, top, middle; Control with cone: 0.82±0.19, n=100 dendrites; DTR with cone: 0.89±0.29, n=73 dendrites; median±IQR, p=0.49, rank sum). In the DTR condition without a cone contact, mGluR6 localization was variable and significantly different from DTR branches with a cone contact (Figure 1.3B, C, bottom; DTR without cone: 0.51±0.57μm, n=82 dendrites; median±IQR, p=6.18e-7, rank sum) and from control branches with a cone contact (p=5.63e-9, rank sum). This demonstrates that the presence of the cone stabilizes the mGluR6 protein to the bipolar cell dendritic terminals; in the absence of a cone, the mGluR6 becomes mislocalized. Within a single bipolar cell, dendritic branches exhibited cone-dependent mGluR6 distributions, indicating that mGluR6 localization is regulated in a branch-specific manner. This mislocalization is consistent with our previous findings (Dunn, 2015) and indicates that these mGluR6 rearrangements are stable for 60 days after cone loss. In addition to mGluR6, the transduction channel Trpm1 also colocalized mGluR6, such that both proteins are either present with a cone or absent without a cone (Figure S1.3).

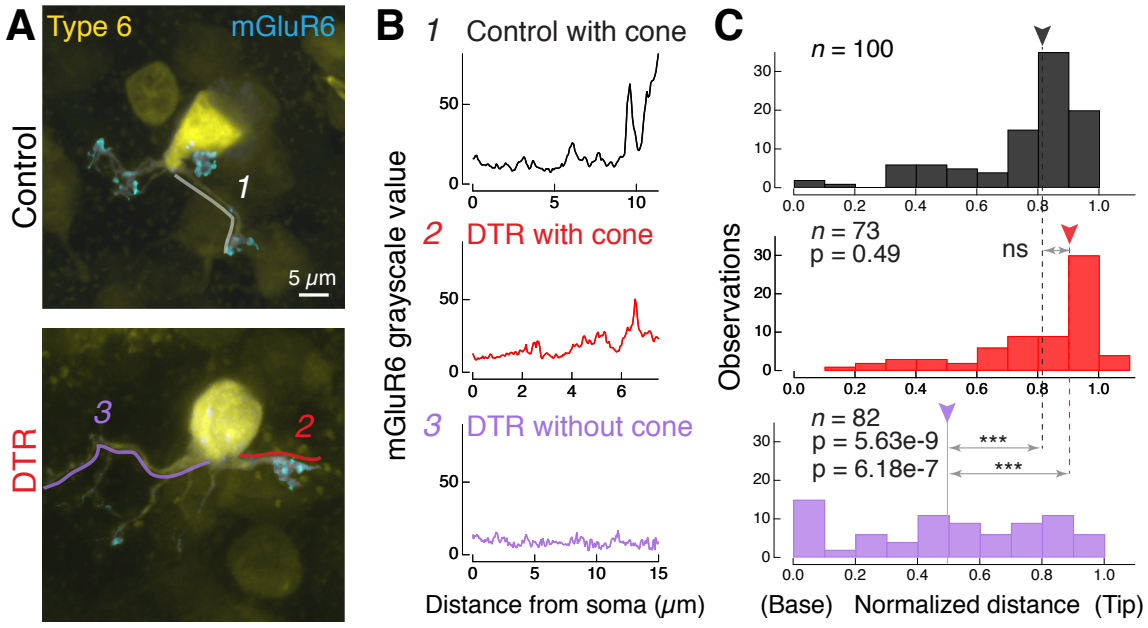

Figure 1.3. At the first-order synapse, glutamate receptor mGluR6 is regulated in a cone-dependent and branch-specific manner after cone loss.
(A) Confocal images of the type 6 bipolar cell dendrites labeled in the *Grm6-TdTomato* line (yellow) and the associated postsynaptic glutamate receptor mGluR6, labeled by immunostaining, within the dendrites (cyan). Same bipolar cells depicted in Figure 1.2D where cone locations are shown. Examples of line segments (1, 2, 3) traced from the soma to the dendritic tip. These line segments were used to quantify the grayscale value of mGluR6. Image of the mGluR6 within the bipolar cell has been adjusted to accentuate the location of synaptic puncta, but images analyzed for intensity values were not adjusted.
(B) Grayscale intensity value of mGluR6 channel for a (1) dendrite in control retina that contacts a cone, (2) dendrite in DTR retina that contacts a cone, and (3) dendrite in DTR retina that does not contact a cone.
(C) Histogram of peak location of mGluR6 from all line segments in control (black) and DTR bipolar cell dendrites, either ending with a cone (red) or without a cone (lavender). Number of dendrites within categories of mGluR6 peak location at the base next to the soma (0) to the tip (normalized to 1). Arrowheads point to the median. Horizontal arrows indicate comparisons made in each panel. Asterisks indicate significance (see Results). In control, only three line segments ended without a cone (data not shown). Data combined across time intervals. Number of dendritic line segments drawn for each condition (*n*). See also Figure S1.3.

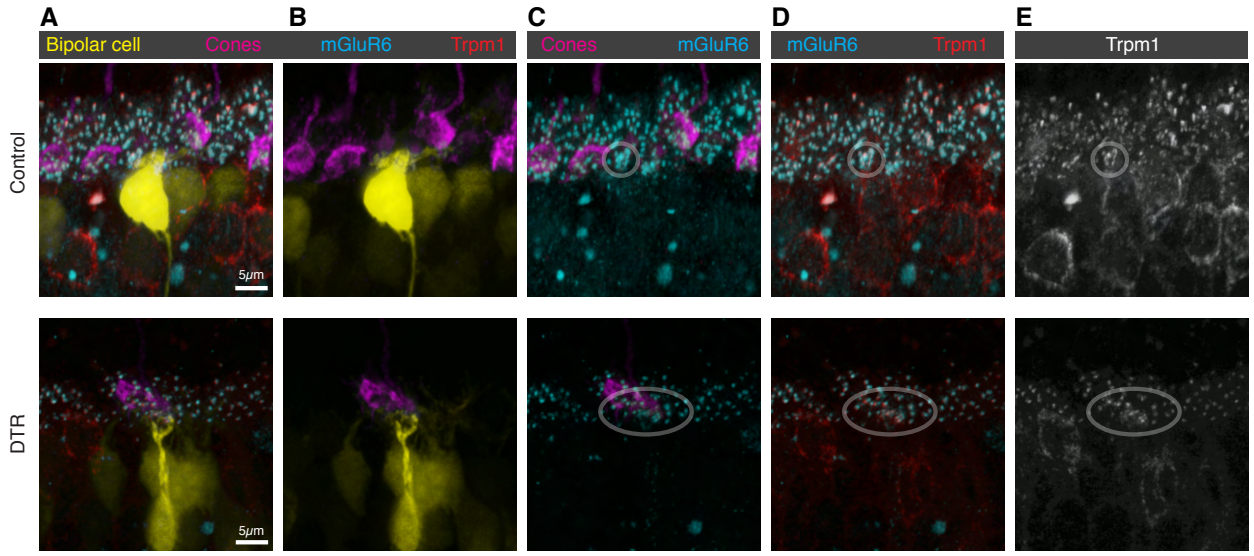

Figure S1.3. Transduction channel Trpm1 colocalizes with mGluR6. Related to Figure 1.3.
(A) Sections of (top) control and (bottom) DTR retina. Confocal images of a type 6 cone bipolar cell labeled by *Grm6-TdTomato* (yellow), cones labeled by cone arrestin (magenta), glutamate receptor labeled by mGluR6 (cyan), and transduction channel labeled by Trpm1 (red).
(B) Bipolar cell dendrites contacting nearby cones. In the DTR retina, only a single cone remains in the vicinity.
(C) mGluR6 is present in clusters at the pedicles of cones (ovals), whereas rod-associated mGluR6 is present as discrete puncta.
(D) mGluR6 and Trpm1 colocalize both at the cone-associated clusters (ovals) and at the rod-associated puncta. (Bottom) In the absence of other cones, we find no evidence for clusters of cone-associated mGluR6 or Trpm1 alone, suggesting that both proteins are either present or absent.
(E) Trpm1 colocalizes at cone-associated clusters, rod-associated puncta, and around the somas of ON bipolar cells.

Second-order synapse: Bipolar cell output synapses and major ganglion cell partners remain morphologically stable

Previous work demonstrates that the dendritic inputs and axonal outputs of bipolar cells are coordinated in their growth during development (Soto et al., 2012; Johnson et al., 2017). Given the rearrangements we observed in the bipolar cell inputs, we next aimed to understand whether there

were corresponding changes in their output. For a subset of the type 6 bipolar cells whose dendrites we had analyzed, we measured the area of their axon territory and found no significant differences between type 6 bipolar cells in control and DTR retina (Control: 181±48.1, *n*=19 bipolar cells; DTR: 232±106.5µm², *n*=23 bipolar cells; median±IQR; p=0.06, rank sum; data not shown). These findings indicate that type 6 bipolar cell axonal territory does not reflect the extension observed at the dendrites.

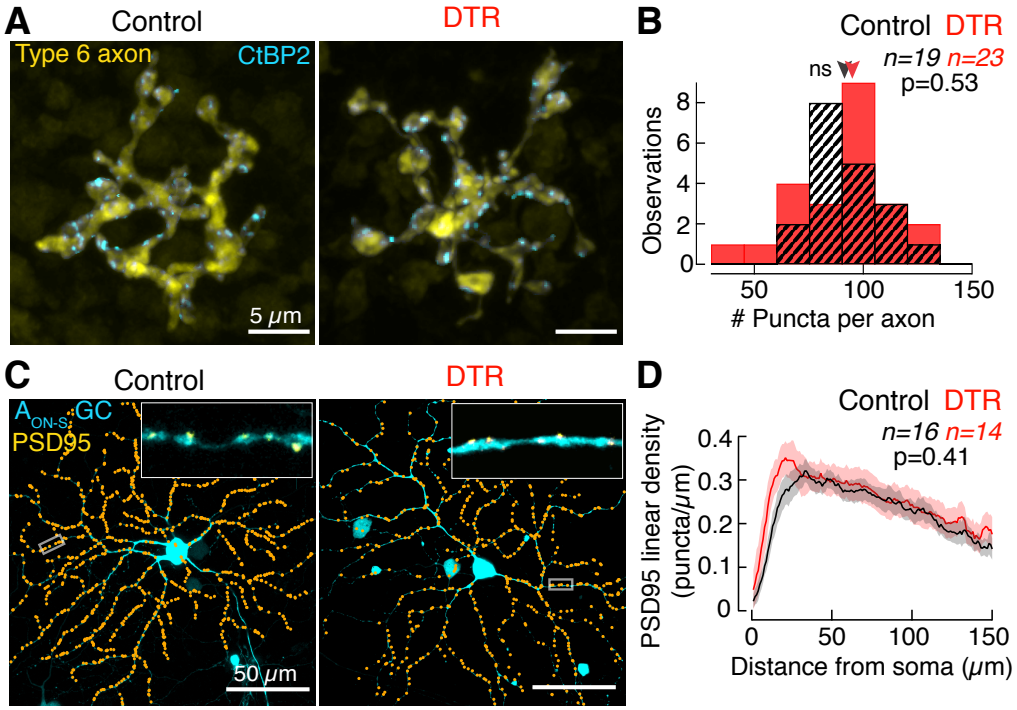

Figure 1.4. At the second-order synapse, type 6 cone bipolar cell glutamate release sites and $A_{ON\text{-}S}$ ganglion cell postsynaptic densities are stable after cone loss.
(A) *En face* confocal images of type 6 cone bipolar cell axons labeled in the *Grm6-TdTomato* line (yellow). Glutamate release sites are labeled by immunostaining for CtBP2 (cyan). Only CtBP2 associated with the bipolar cell axon is shown.
(B) Histogram of the number of CtBP2 puncta within each type 6 cone bipolar cell axon terminal See also Figure S1.4.
(C) *En face* images of the $A_{ON\text{-}S}$ ganglion cell labeled by a cell fill (cyan) and by postsynaptic density PSD95 fluorescent protein. The plasmids encoding these fluorescent proteins were introduced by gene gun. Upper right inset shows a stretch of dendrite with the raw PSD95 puncta (yellow). Main image shows the identified locations of PSD95 (orange dots).
(D) Linear density of PSD95 puncta across dendritic distance from the soma to the periphery. Data represented as mean±sem. See also Figure S1.4.

Next, we counted the number of presynaptic ribbon release sites within individual type 6 bipolar cell axon terminals. To do this we immunostained for the ribbon synapse-associated protein C-terminal binding protein-2 (CtBP2; Figure 1.4A). The number of ribbons in type 6 bipolar cells did not differ between DTR and control retina (Figure 1.4B; Control: 89±22, *n*=19 bipolar cells; DTR: 92±26, *n*=23 bipolar cells; median±IQR; p=0.53, rank sum). This indicates that the number of release sites in type 6 bipolar cells was not affected by the reduced number of cone inputs nor the reduced mGluR6 expression at the dendrites of these same cells.

To measure the functional impact of partial cone loss on bipolar cell responses, we recorded the *in vivo* electroretinogram (ERG) (Figure S1.4). While the ERG was unchanged at rod light levels ("Dark-adapted", left), both the a-wave, driven by photoreceptors, and the b-wave, driven by ON bipolar cells, were significantly reduced at cone light levels ("Light-adapted", right). This indicates that the population voltage responses of ON cone bipolar cells reflect the loss of cone input. The morphological loss of cone inputs to the type 6 cone bipolar cell dendrites and the stability of its output synapses are consistent with the reduction in the collective ON cone bipolar cell functional output after cone loss. However, the extent to which the perturbations of the type 6 cone bipolar cell dendrites is reflected in the population ERG is unknown.

While synapses with type 6 bipolar cells are stable, $A_{ON\text{-}S}$ ganglion cells could potentially change synapses with other bipolar cell partners (Schwartz et al., 2012; Okawa et al., 2014; Tien et al., 2017). To visualize synapses in these ganglion cells, we biolistically transfected control and DTR retinas with a plasmid encoding fluorescently tagged postsynaptic density (PSD95), a key postsynaptic component of the synapse (Figure 1.4C). We quantified the density of PSD95 within the dendrites of $A_{ON\text{-}S}$ ganglion cells and found no significant difference between control and DTR retinas (Figure 1.4D). We also found no change in $A_{ON\text{-}S}$ ganglion cell dendritic arbor complexity as

measured by Sholl analysis (data not shown). Despite the loss of synaptic contacts onto the dendrites of type 6 bipolar cells, synapses in the $A_{ON\text{-}S}$ ganglion cells remained morphologically stable. Such morphological stability provides evidence against *de novo* changes arising at the synapses between cone bipolar and ganglion cells after cone loss.

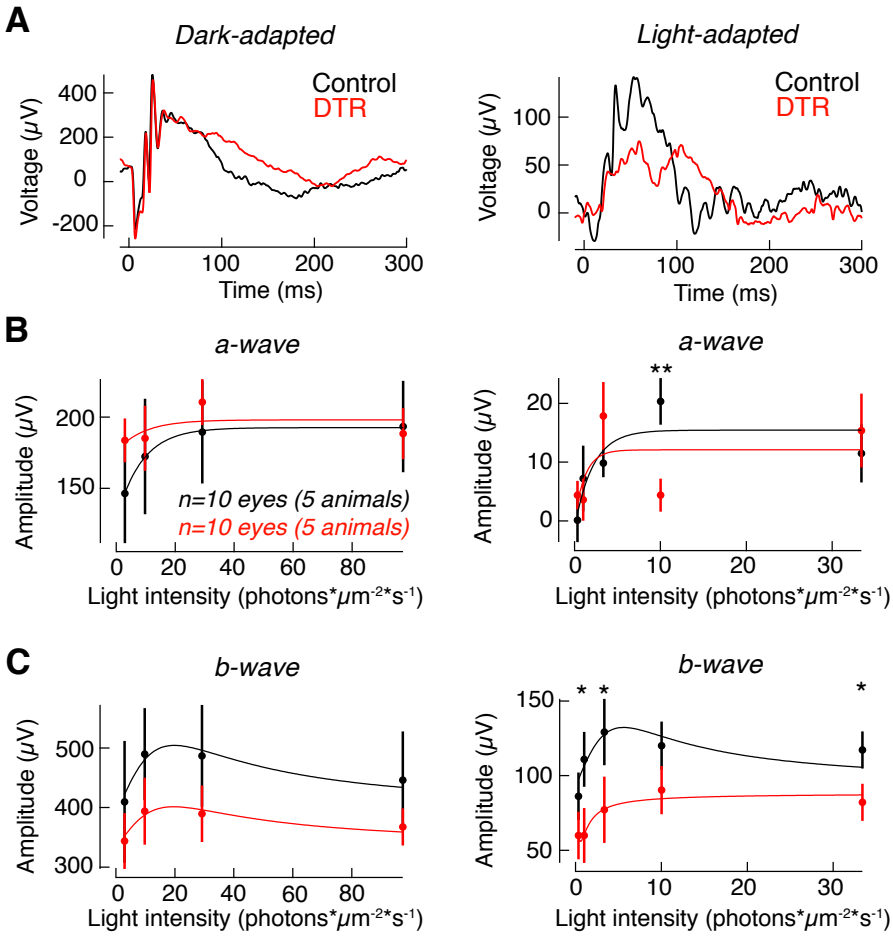

Figure S1.4. The photopic, but not scotopic, electroretinogram response is decreased after partial cone ablation. Related to Figure 1.4.

(A) Example traces of ERGs from control (black) and DTR (red) mice show an intact response at scotopic light levels (left) and a diminished response at photopic light levels (right). Traces shown are averages of recordings from the right and left eyes, which were made simultaneously.

(B) Amplitude of the a-wave, a measure of photoreceptor activity, across a range of light levels is maintained at scotopic light levels (left) but reduced in photopic light levels (right). Data fit with a single exponential function. (In light-adapted condition at 10.02 photons/μm^2*s^{-1}: Control: -20.36±4.0μV, *n*=10 eyes from 5 animals; DTR: -4.39±2.8μV, *n*=10 eyes from 5 animals; mean±sem; p=0.0077, t-test).

(C) Amplitude of the b-wave, a measure of ON bipolar cell activity, across a range of light levels is maintained at scotopic light levels (left) but reduced in photopic light levels (right). Data fit with a serpentine function. (In light-adapted condition: at 1.00 photons/$\mu m^{2}*s^{-1}$: Control: 110.94±18.4μV; DTR: 59.98±11.1μV; p=0.0332; at 3.34 photons/$\mu m^{2}*s^{-1}$: Control: 129.19±22.3μV; DTR: 77.14±6.9μV; p=0.0387; at 33.4 photons/$\mu m^{2}*s^{-1}$: Control: 117.27±12.43μV; DTR: 82.19±9.5μV; p=0.0431; *n*=10 eyes from 5 animals; mean±sem; t-test).

Spatio-temporal receptive fields of $A_{ON\text{-}S}$ ganglion cells widen spatially and slow temporally after cone loss

Next we examined functional properties at the level of the retinal output. We recorded the light responses of dorsal-nasal $A_{ON\text{-}S}$ ganglion cells in whole-cell current clamp. We measured the spatio-temporal receptive fields by presenting a white noise flickering bar stimulus in an intensity range that stimulated cones and recorded membrane voltage (Figure 1.5A-B). Linear-nonlinear modeling was used to calculate temporal filters for the cell's response at the location of each bar in space, thereby generating a spatio-temporal receptive field map (Figure 1.5C-E). The spatial receptive field was extracted by projecting each point in space onto the first temporal principal component (Figure 1.5F). Under control conditions, $A_{ON\text{-}S}$ ganglion cells have a narrow depolarizing center and wider hyperpolarizing surround. This basic receptive field structure persists in $A_{ON\text{-}S}$ ganglion cells in DTR retina. To compare the center and surround components, individual spatial receptive fields were fit by a difference of Gaussians (Figure 1.5F, insets). The receptive fields of ganglion cells in DTR retina had significantly narrower centers (Figure 1.5H; Control: 0.0973±0.046, *n*=24 ganglion cells; DTR: 0.0846±0.025mm, *n*=30 ganglion cells; median±IQR; p=0.0061, rank sum), wider surrounds (Figure 1.5I; Control: 0.247±0.17; DTR: 0.377±0.043 mm; median±IQR; p=0.0044, rank sum), and unchanged center-to-surround weight ratios (Figure 1.5J; Control: 3.41±2.95; DTR: 3.72±2.89; median±IQR; p=0.15, rank sum). Additionally, the temporal filters of cells from DTR retina were

significantly slower than those of cells from control retina, as measured by an increase in the time to peak of the first temporal principal component (Figure 1.5G, K; Control: 0.09±0.02; DTR: 0.10±0.03 sec; median±IQR; p=0.0049, rank sum). These data provide evidence for functional changes in the receptive fields of ganglion cells after input loss.

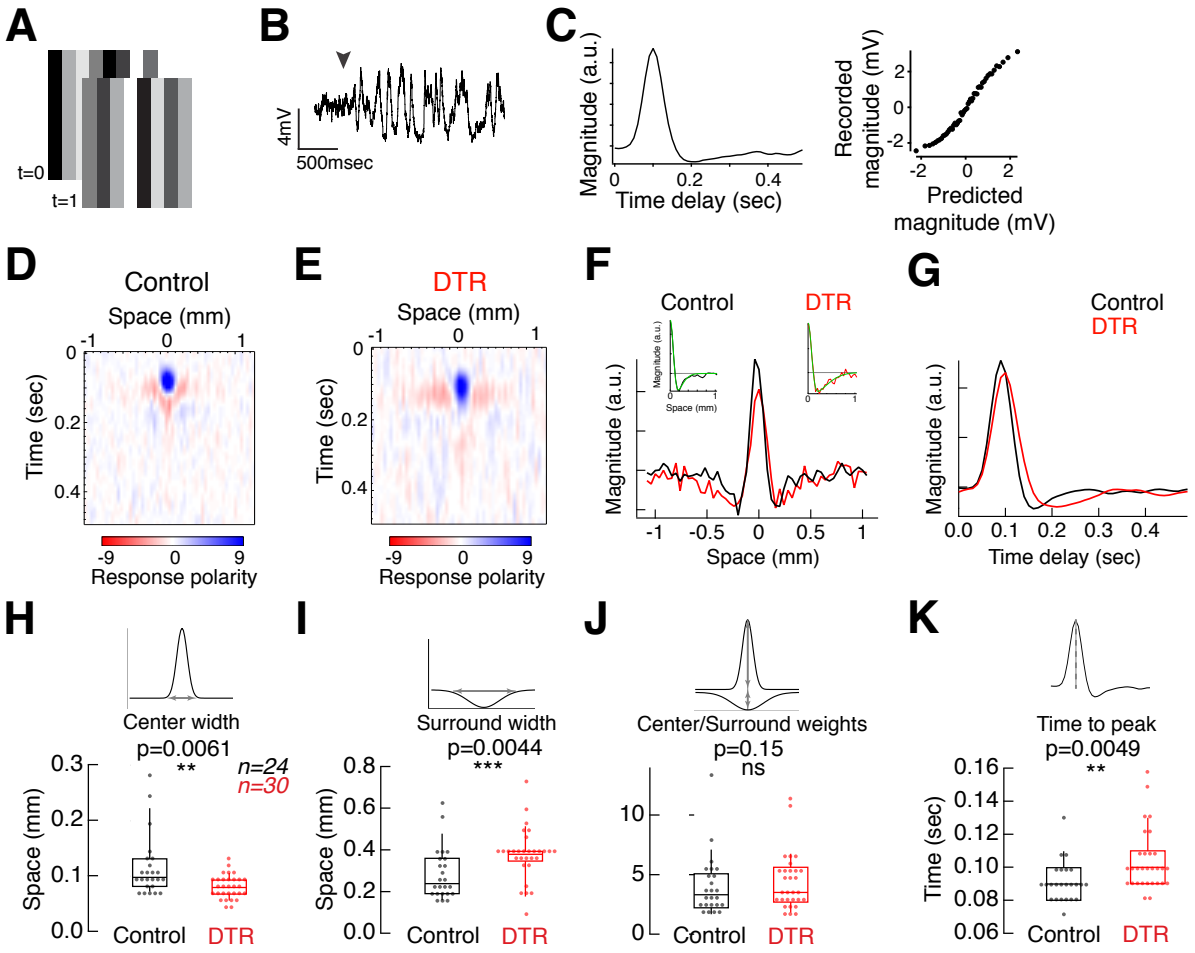

Figure 1.5. $A_{ON\text{-}S}$ ganglion cell spatio-temporal receptive fields widen spatially and slow temporally after cone loss.
(A) Example stimuli at 2 points in time where the intensity of each bar is randomly drawn from a Gaussian distribution.
(B) Voltage response of an $A_{ON\text{-}S}$ ganglion cell in current clamp. Arrowhead indicates the onset of the stimulus fluctuations on a mean background.
(C) One spatial slice of the temporal filter (left) and nonlinearity (right) calculated for a cell from control retina.

(D, E) Spatio-temporal receptive field obtained from a correlation of the response with the stimulus where red and blue represent opposite polarity responses.
(F) Spatial receptive field for the cells shown in D, E taken for dominant principal components. (inset) Difference of Gaussians fit (green) for each cell.
(G) Temporal filters from the first principal components of the cells from D, E.
(H, I) Parameters of the difference of Gaussians fit show significantly narrower centers and wider surrounds for DTR receptive fields. Asterisks indicate significance (see Results). Box plots show median with interquartile range and whiskers from 10% to 90% of the data. See also Figure S1.5.
(J) No significant difference was observed in the ratio of center and surround weights between control and DTR.
(K) Time to peak of the temporal receptive fields for DTR cells are significantly slower than control cells. See also Figure S1.5.

While the majority of control cells had receptive fields that were described by principal components which accounted for more than 80% of the variance of the cell's response, this was not true for DTR cells (Figure S1.5A). Responses with increased variance may result from decreased input due to cone ablation, but they still reflected center-surround organization and could be fit with a difference of Gaussians (Figure S1.5B). However, 35% of DTR cells had receptive fields without spatial center-surround organization and which could not be fit with a difference of Gaussians (Figure S1.5C). All of these cells had more than 50% cone loss within their dendritic fields. In contrast, all cells we recorded with less than 50% cone loss in their dendritic fields had receptive fields that could be fit with a difference of Gaussians. These results demonstrate that, up to 50% loss of cones, the general center-surround structure of ganglion cell receptive fields remains intact, while changes do occur in spatial and temporal filtering.

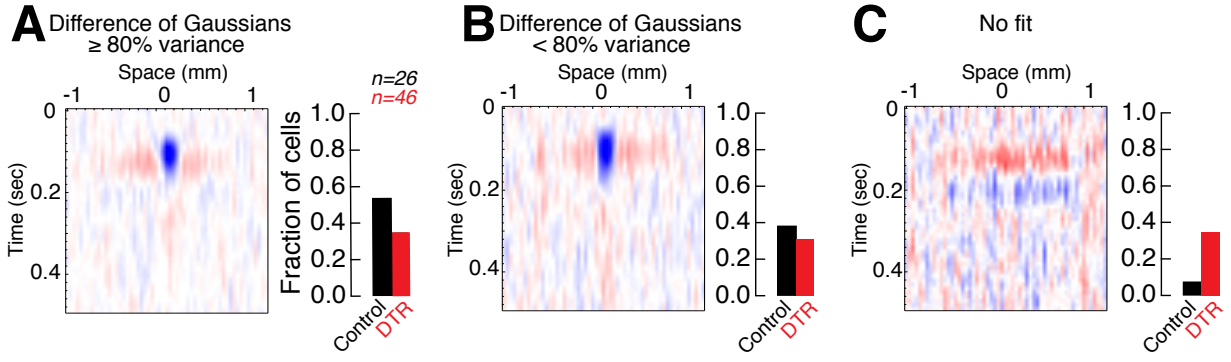

Figure S1.5. $A_{ON\text{-}S}$ ganglion cell from DTR retina exhibit a range of receptive field structures. Related to Figure 1.5.

(A) Spatio-temporal receptive field for a cell from DTR retina which was fit by a difference of Gaussians and for which ≥80% of the response variance in time was described by the first principal component. Bar graph (right) indicates that 53.8% of control and 34.8% of DTR cells fell into this category. Total number of ganglion cells in control and DTR retina indicated by *n*.

(B) Spatio-temporal receptive field for a cell from DTR retina which was fit by a difference of Gaussians and for which <80% of the response variance in time was described by the first principal component. Bar graph (right) indicates that 38.5% of control and 30.4% of DTR cells fell into this category.

(C) Spatio-temporal receptive field for a cell from DTR retina which was not fit by a difference of Gaussians. Bar graph (right) indicates that 7.7% of control and 34.8% of DTR cells fell into this category. These cells were not included in the receptive field analysis in Figure 1.5.

Spatial receptive field adjustments in DTR retina are distinct from partial stimulation of control retina

Having found changes in the receptive field center and surround widths, we next examined whether such receptive field adjustments could be recapitulated with partial stimulation of the cone mosaic in control retina. If partial stimulation of the cone mosaic in control retina produces similar adjustments in the receptive field as cone loss, then we would conclude that the circuit within DTR retina is like that of control, e.g., these adjustments occur by pre-existing mechanisms of adaptation acting on the receptive field (Enroth-Cugell and Freeman, 1987). In this case, control and DTR retina would be capable of expressing the same receptive field adjustments with either cone loss or partial cone stimulation because the rest of the retinal circuit, aside from the cones, is identical. However, if partial stimulation of the cone mosaic in control retina cannot recapitulate the adjustments observed following cone loss, then we would conclude that the DTR retinal circuit has changed in ways distinct from control retina, i.e., by *de novo* mechanisms not activated by partial stimulation in control retina. To test these two hypotheses, we presented the bar noise stimuli described above and then blanked 50% of the bars to simulate unresponsive cones within the

receptive field of $A_{ON\text{-}S}$ ganglion cells. Blanked bars constantly displayed the intensity of the stimulus mean to hold cones at a uniform level of adaptation.

Comparison between the receptive field profile obtained with full and partial stimulation revealed characteristics distinct from DTR retina (Figure 1.6A-B). Partial stimulation resulted in constant widths for the center (Figure 1.6C; full: 0.08±0.02; partial: 0.08±0.01mm; n=19 ganglion cells; median±IQR; n=19; p=0.07; sign rank) and surround (Figure 1.6D; full: 0.24±0.10; partial: 0.20±0.12mm; median±IQR; p=1; sign rank), and no change in the center-to-surround weights of the receptive fields (Figure 1.6E; full: 5.5±4.38; partial: 4.31±6.29; median±IQR; p=1; sign rank). The lack of change in receptive field parameters observed with partial stimulation in control retina is distinct from the narrowing of the center and widening of the surround that was observed in DTR retina (Figure 1.5H-J). These results suggest that the DTR retinal circuit exhibits *de novo* changes distinct from the control retinal circuit. Partial stimulation also resulted in a slower temporal filter as compared to full stimulation (Figure 1.6F; full: 0.09±0.01; partial: 0.1±0.01sec; median±IQR; n=19; p=0.011; sign rank). This change is congruent with the slower temporal filter observed in DTR vs. control retina (Figure 1.5K). This suggests that the temporal changes to ganglion cell receptive fields are the product of a mechanism pre-existing within the mature retinal circuit. Taken together, these results indicate that the mature retinal circuit exhibits both *de novo* changes after input loss which affect spatial processing and pre-existing mechanisms that affect temporal processing.

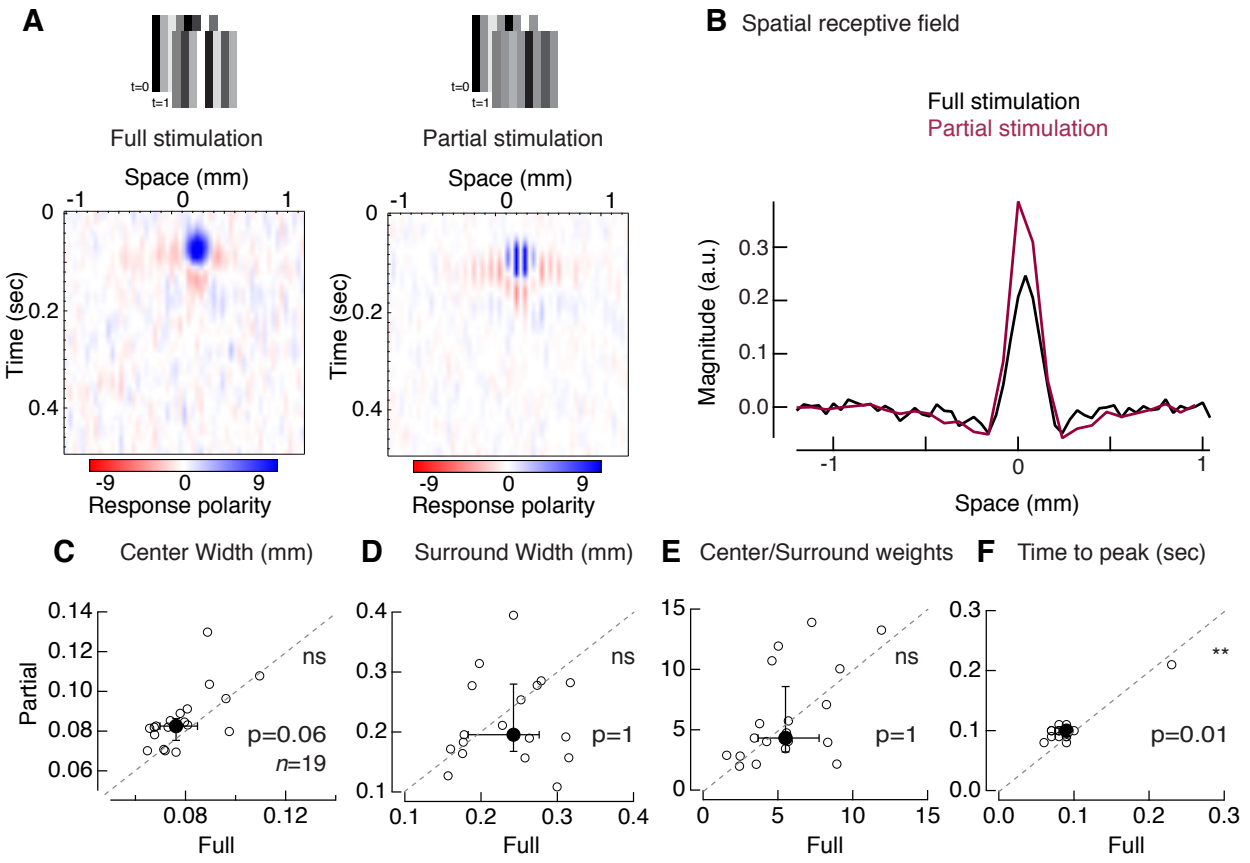

Figure 1.6. Control $A_{ON\text{-}S}$ ganglion cell receptive fields retain widths with partial stimulation.
(A) Spatio-temporal receptive field obtained from voltage responses of a control $A_{ON\text{-}S}$ ganglion cell in current clamp. Receptive field obtained with a (left) full bar noise stimulus and (right) partial bar noise stimulus with 50% of the bars held constant at the mean intensity. Receptive fields measured from the same cell. Red and blue represent opposite polarity responses.
(B) Spatial receptive field for the same $A_{ON\text{-}S}$ ganglion cell depicted in (A) either with full (black) or partial (maroon) stimulation.
(C-E) Gaussian fit parameters for receptive fields measured with full and partial stimulation within the same control $A_{ON\text{-}S}$ ganglion cells: (C) one standard deviation center width, (D) one standard deviation surround width, and (E) center-to-surround weights.
(F) Time to peak of temporal receptive fields. Individual cells (open circles) and median±IQR (closed circles±error bars). Dotted line represents line of slope unity.

To understand where in the retinal circuit these *de novo* changes in receptive field arise, we recorded the excitatory and inhibitory input currents onto $A_{ON\text{-}S}$ ganglion cells from control and DTR retina in response to the full receptive field stimulus (Figure 1.7). We found that the two characteristic changes we observed in the voltage receptive fields each derived from a different source: the

decrease in center width was present in only the excitatory current receptive fields (Figure 1.7E), and the increase in surround width was present only in the inhibitory current receptive fields (Figure 1.7F, J). This indicates that the narrower center is inherited through excitation onto the ganglion cell, i.e., bipolar cell input, while the wider surround is inherited through direct inhibition onto the ganglion cell, i.e., through amacrine cell input. We also found that the center-to-surround weight ratio for excitation is significantly higher in DTR retina than in control retina, unlike in either the voltage or the inhibitory receptive fields (Figure 1.7G, K). This change in ratio is driven by weaker surround weights, suggesting that horizontal cell contribution to the surround is weaker after cone loss. However, the voltage receptive fields do not exhibit this change in ratio, suggesting that the center-to-surround balance is restored by the retinal output. Both excitation and inhibition displayed the slower time to peak seen in voltages from DTR retina and partially stimulated control retina (Figure 1.7H, L). These results identify the excitatory and inhibitory pathways converging onto the ganglion cell as both contributing to the receptive field changes following partial cone loss.

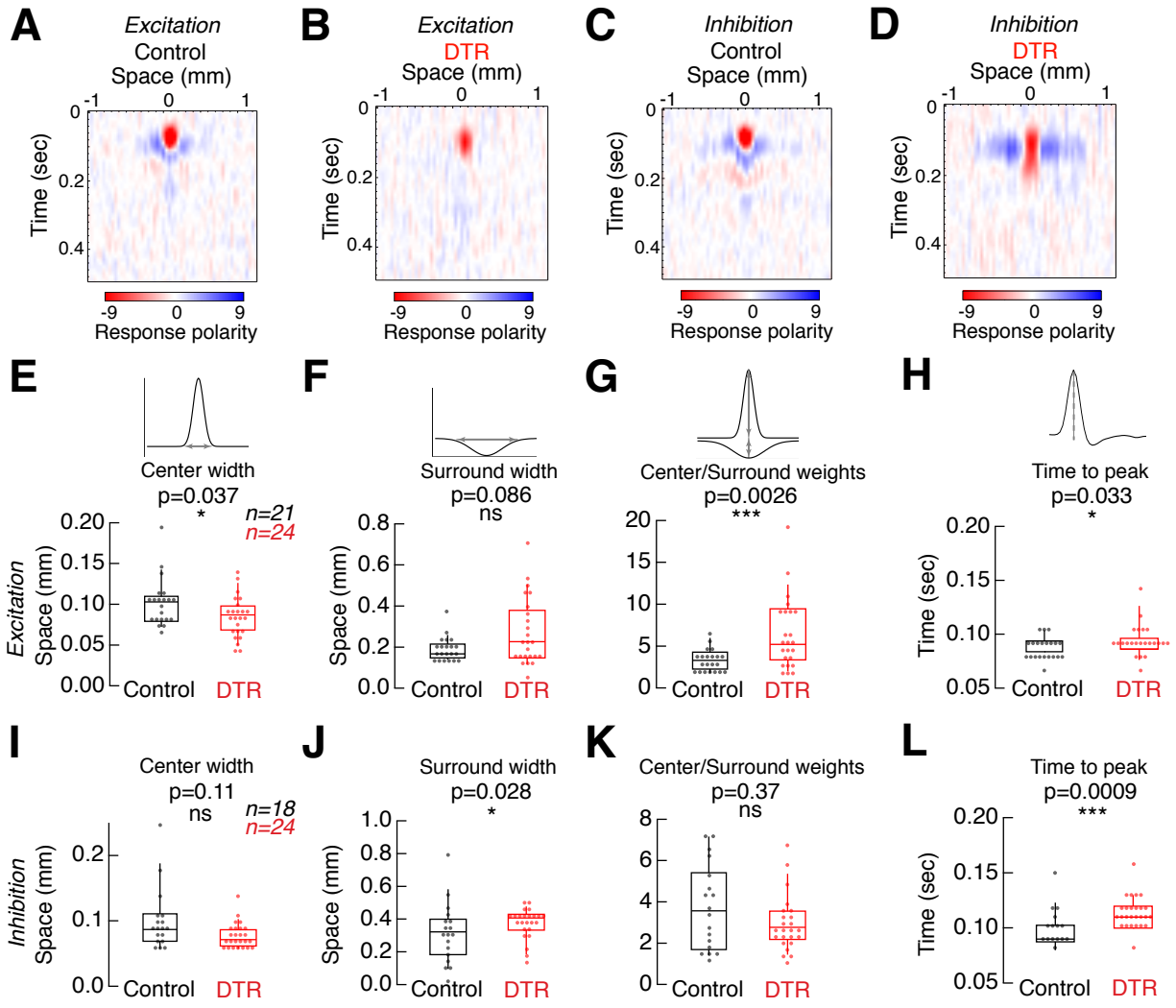

Figure 1.7. Excitation and inhibition drive different components of $A_{ON\text{-}S}$ ganglion cell receptive field changes after cone loss.

(A, B) Spatio-temporal receptive field obtained from excitatory currents onto an $A_{ON\text{-}S}$ ganglion cell recorded in voltage clamp at -60mV.

(C, D) Spatio-temporal receptive field obtained from inhibitory currents onto an $A_{ON\text{-}S}$ ganglion cell recorded in voltage clamp at +10mV.

(E-G) Gaussian fit parameters for receptive fields measured from excitatory currents. (E) Excitatory currents show significantly narrower centers after cone loss, though (F) no change in surround widths. (G) The center-to-surround weights increase after cone loss.

(H) Time to peak of the temporal receptive fields is significantly slower.

(I-K) Gaussian fit parameters for receptive fields measured from inhibitory currents. (I) Inhibitory currents show no change in center width after cone loss, though (J) significantly wider surrounds. (K) The center-to-surround weights are unchanged.

(L) Time to peak of the temporal receptive fields is significantly slower. Asterisks indicate significance (see Results). Box plots show median with interquartile range and whiskers from 10% to 90% of the data.

Discussion

Understanding the mature retinal circuit's response to loss of cones requires temporal control over cone death. In our previous work with laser ablation of cones, we found that mGluR6 disappears selectively from the dendritic terminals where cones have been lost within the first 24 hours (Dunn, 2015). In the present work, with the DTR model, we extend our window of observation by ablating cones *in vivo* and waiting 3 to 60 days before examining the retina (Figure 1.1). In this longer time window, we observe that within three days of cone ablation, type 6 cone bipolar cell dendrites remodel. Some type 6 bipolar dendrites that lose cone contact simplify while others extend and possibly form new synapses (Figure 1.2). We also observe that the mGluR6 distribution is still dendrite-specific and cone-dependent (Figure 1.3). These changes are consistent with a mechanism that independently regulates each dendrite and depends on the presence or absence of a cone contact on that dendrite. Despite this rearrangement of the first-order synapse in the cone pathway, we observed structural stability in the morphology and the number of presynaptic release sites in the type 6 bipolar cell axons (Figure 1.4). This suggests that changes in the number and spatial arrangement of inputs to type 6 bipolar cells are not reflected in the number and spatial arrangement of their outputs. Furthermore, we found postsynaptic densities were maintained within the $A_{ON\text{-}S}$ ganglion cells that receive the majority of their input from type 6 cone bipolar cells (Figure 1.4). Despite this stability of the second-order synapse of the cone pathway, we found $A_{ON\text{-}S}$ ganglion cells exhibited adjustments in their cone-mediated voltage responses (Figure 1.5). $A_{ON\text{-}S}$ ganglion cells had significant changes to their spatial receptive fields. These spatial changes in DTR retina were distinct from those observed in control retina with partial stimulation (Figure 1.6), suggesting that the mechanism(s) are *de novo* rather than pre-existing within the retinal circuit. Indeed, when we examined the input currents to $A_{ON\text{-}S}$ ganglion cells, we found that a dominant

underlying mechanism for the expansion of the receptive field surround involves inhibitory circuits (Figure 1.7).

Developmental vs. mature reactions to input loss

Here we report that the loss of cones is capable of triggering postsynaptic dendritic remodeling, including growth, in type 6 bipolar cells. The mechanism that induces growth in these dendrites remains unknown. Neurotransmission has been demonstrated throughout the nervous system to be capable of inducing calcium-mediated cytoskeletal changes and subsequent dendritic remodeling (Sorensen, 2006; reviewed in Wong and Ghosh, 2002). Membrane-bound factors such as cell adhesion and chemotactic molecules can also modulate dendritic morphology (Sweeney et al., 2011).

In a recent study using photocoagulation in mature rabbit retina, Beier and colleagues reported a capacity for rod bipolar cells to form synapses with photoreceptors outside the lesion; however the cone bipolar cells they examined did not exhibit the same remodeling capacity (Beier et al., 2017). With our different method of ablation and visualization of cone bipolar cells, we did observe remodeling. If we had observed only retraction of dendrites, that would have been evidence for gradual degradation of bipolar cells and their circuits. Instead we see retraction of some dendrites alongside the persistence and growth of other dendrites, indicating that bipolar cell dendrites may be seeking viable synaptic partners. Indeed, we found abnormally long dendrites in DTR retina contacting cones with mGluR6 localized to the contact site, suggesting that dendrites may have formed new synapses with more distant cones, though we cannot rule out the possibility that these synapses were pre-existing and have simply translocated away from the bipolar cell; however, translocation of photoreceptors has not been observed (Han et al., 2012; Sher et al., 2013). A previous study eliminating cone transduction demonstrated that cone bipolar cells will make ectopic

synapses with existing rods (Haverkamp et al., 2006). However, the study did not distinguish whether these synapses were formed during development or in the fully mature retina. Because we ablated cones in mature retina, we conclude that dendritic growth can be induced in bipolar cells after initial synapse development, as type 6 ON cone bipolar cells find their appropriate synaptic partners by P13 in the mouse (Dunn and Wong, 2012). This supports the assertion that the mature retina has some capacity for remodeling to replace lost synaptic partners.

Another contrasting result is the coordination of input and output synapses observed with developmental perturbations. It has been shown that the number of presynaptic release sites in type 6 bipolar cell axon terminals can increase or decrease based on the level of spontaneous activity incident on bipolar cells in germ line mutations (Kerschensteiner et al., 2009; Soto et al., 2012). Despite decreased numbers of input to type 6 bipolar cells in our manipulation, we do not see an increase or decrease in the number of presynaptic release sites. This indicates either that the decrease in inputs does not alter spontaneous activity enough to activate this mechanism, or that this mechanism is not present in mature type 6 bipolar cells.

Relationship to retinal disease

Mice have been widely used to understand human outer retinal diseases. The challenge remains in the interpretation of effects on the retina across organisms with vast differences in lifespan and onset of retinal degeneration. Cone loss has been identified as the instigator for broader retinal damage (Marc and Jones, 2003). Here, our methods allowed us to test whether partial cone loss would cause rearrangement of the retina. We limited our observation to two months after diphtheria toxin injection. In this period, we did not see obvious rearrangement of the inner retina, as evidenced by intact axons stratifying in the appropriate layers and gross anatomy of retinal layers

(Figure S1.1). However, the acute and limited cell loss induced by diphtheria toxin injection may not mimic the slow and severe death observed in certain types of retinal degeneration. Nevertheless, our data suggest several salient findings that may inform the development and optimization of therapies for retinal degeneration: (1) type 6 cone bipolar cells preferentially contact cones following cone death, increasing the likelihood of successful synaptic integration of newly transplanted photoreceptors in cellular therapies; (2) structural and synaptic features of the bipolar cell to retinal ganglion cell synapse are intact even after an extended period of cone loss, enabling therapeutic strategies that either aim to replace lost cones or interface directly, through optogenetics or prosthetic devices, with bipolar cells to restore phototransduction to the retinal circuit; (3) $A_{ON\text{-}S}$ ganglion cells maintain center-surround receptive field structure at least through 50% cone loss, opening the possibility of developing strategies that specifically target these cells; (4) overall, the degree of retinal remodeling is relatively limited in comparison to previous reports made over longer time windows, suggesting that vision restoration therapies may have increased efficacy earlier in the disease course. Furthermore, at these early stages the functional resilience observed in our study may help explain why patients with photoreceptor degeneration do not report visual deficits until the majority of photoreceptors are gone and suggest that resilience within the visual system may arise first within the retina.

Potential compensatory circuit changes

In DTR retina, we observed what might be considered a compensatory gain of function in the cone-mediated ganglion cell receptive field. By removing 50-75% of cones, our manipulation effectively decreases the cone-mediated signal-to-noise ratio at ganglion cells. The efficient coding hypothesis laid out by Atick and Redlich predicts that the optimal receptive field for ganglion cells has a wider, weaker surround as the signal-to-noise ratio decreases (Atick and Redlich, 1990). The

increased size of the surround that we observe in the receptive fields of ganglion cells from DTR retina is consistent with these predictions.

Atick and Redlich's efficient coding hypothesis further predicts that the optimal receptive field for ganglion cells at an even lower signal-to-noise ratio should be a single wide Gaussian without a spatially opponent surround. Indeed, we observed that one third of ganglion cells in DTR retina could not be captured by a difference of Gaussians and exhibited a wide receptive field best captured by a single Gaussian (Figure S1.5C). These ganglion cells in the no-fit category often had far fewer remaining cones within the dendritic field than those in the categories where a difference of Gaussians could be fit. Thus, those ganglion cells in the no-fit category could be considered the condition with the lowest signal-to-noise ratio. The widening of the surround and the eventual loss of a spatially-opponent receptive field we observe are consistent with theory and indicate that the receptive field changes we see may maintain better signal encoding in the cone-depleted retina.

Atick and Redlich's efficient coding hypothesis also predicts an increase in the size of the center, which our data did not show. An increase in center size consistent with theory may require formation of new excitatory synapses, evidence of which we did not see at these time points at the first- nor second-order synapses within retina. The adjustments in receptive field sizes in DTR retina could be explained by a loss in excitatory synapses, originating at the cone-to-cone bipolar cell synapses, which contribute to the center, and a gain in inhibitory synapses, which contribute to the surround. In our examination of excitatory and inhibitory input currents that contribute to the voltage receptive field, we identified the potential sources of receptive field changes following partial cone loss in mature retina. First, the narrower receptive field center of excitatory inputs, via bipolar cell input, suggests that the rare observation of bipolar cell dendritic extension is not reflected in the receptive field profiles across the population of ganglion cells (Figures 1.2H, 1.7E). Second, the

decrease in center-to-surround ratio and the constant surround width in the receptive field of excitatory inputs suggests that the spatial contribution of horizontal cells to the surround has not changed while the weight of its influence has diminished following cone loss (Figure 1.7F, G). Consistent with this interpretation, horizontal cell populations were morphologically unaffected in DTR retina (Figure S1.2A, Table S1.1). This decrease in surround weight could potentially compensate for the loss of bipolar cell input observed in the ERGs. Finally, the wider receptive field surround of inhibitory inputs, via amacrine cells, suggests that direct amacrine cell influence on ganglion cells has expanded following partial cone loss (Figure 1.7J). Such an expansion could arise from *de novo* inhibitory synapses with pre-existing or new amacrine cell partners with the $A_{ON\text{-}S}$ ganglion cells. Such changes in the receptive field structure are consistent with the greater dynamics of inhibitory circuits compared to excitatory circuits in visual cortex following monocular deprivation (Villa et al., 2016). Villa and colleagues proposed that the modulation of activity following changes in sensory input may be more parsimoniously achieved by adjusting lateral inhibitory synapses compared to feedforward excitatory synapses, and our findings are consistent with their proposal. These results will direct our future studies of the compensatory mechanisms active in the retina after cone loss to the amacrine cell inputs onto these ganglion cells.

Stability and plasticity across central nervous system circuits

As Wandell and Smirnakis aptly wrote, "There can be no serious debate as to whether the brain is plastic or not: it is both. It is more worthwhile to investigate distinct systems and understand conditions under which each system is plastic or stable" (Wandell and Smirnakis, 2009). Previous work on sensory deprivation has reported cortical rewiring of both excitatory and inhibitory circuits (Keck et al., 2008; 2011; 2013; Hickmott and Merzenich, 2002; reviewed in Harding-Forrester and Feldman, 2018). Lack of evidence for rewiring in the mature retina and lateral geniculate nucleus in

vision (Eysel, 1982) and in thalamus in somatosensation (Wallace and Fox, 1999; Wallace et al., 2001) reduced the interest in searching for pre-cortical mechanisms of plasticity. Here, we have revived the search for plasticity within retina, and indeed we find supporting evidence with dendritic remodeling in bipolar cells and with *de novo* changes to the ganglion cell receptive field structure following input loss. While we also find evidence in support of pre-existing mechanisms to withstand partial cone loss, e.g. stability of synaptic structures at the second-order synapse, our results highlight that circuits of the retina and lateral geniculate nucleus may not be distinct from those in cortex with respect to the capacity for plasticity. Rather, these circuits are subject to similar constraints. A comprehensive body of work demonstrating cortical rewiring following sensory deprivation showed that remodeling is possible only after partial retinal lesions, rather than complete retinal ablation (Keck et al., 2008; 2011; 2013; but see Horton and Hocking, 1998; Smirnakis et al., 2005). In other words, persistence of existing activity is necessary to induce and regulate plasticity, as has been demonstrated in developing visual cortex (Reiter et al., 1986; Hata et al., 1999) and the adult somatosensory cortex (Wallace and Fox, 1999). Complete loss of sensory input also failed to induce remodeling in mature visual cortex (Keck et al., 2008; 2011; 2013). Our system of ablation spared a random population of cones, which could be distinct from previous methods of focal laser lesion (Bier et al., 2017). Indeed, our targeted cone ablation may have been appropriately sparse to induce plasticity/compensation and/or uncover pre-existing mechanisms, e.g. redundancy or adaptation, that underlie resilience in specific retinal circuits.

With the unique accessibility to a specific circuit, we have demonstrated both plasticity and stability, likening the retina to the rest of the brain in this respect. The cell-type specific accessibility of the retina allowed us to garner insights about the contributions of individual synapses to functional resilience of a circuit following input loss.

Experimental Procedures

Experimental model and subject details

Mice

All procedures were done in accordance with the University of California, San Francisco and the University of Washington Institutional Animal Care and Use protocols. The following transgenic mouse lines were crossed: *OPN1SW-Cre* (Akimoto, 2004) for Cre-recombinase expression in cones containing S opsin or *OPN1MW-Cre* (Le et al., 2004) for Cre-recombinase expression in cones containing M opsin, *Rosa26-loxP-stop-loxP-DTR* (Buch et al., 2005) for Cre-dependent expression of the diphtheria toxin receptor, *hLMcone-GFP* for visualization of cones containing M opsin (Fei and Hughes, 2001) or *Ai6* as a reporter for the Cre expression (Madisen et al., 2009), and *Grm6-TdTomato* for visualization of a sparse population of ON bipolar cells (Kerschensteiner et al., 2009). The *Grm6-TdTomato* line labels a variable number of type 5, 6, 7, 8 ON cone bipolar cells and rod bipolar cells. When crossed to a fluorescent reporter line *Ai6,* the *OPN1SW-Cre* revealed labeled cone photoreceptors and a small population of rod photoreceptors, amacrine cells, and ganglion cells (Figure S1.1G-K). When crossed to a fluorescent reporter line *Ai6,* the *OPN1MW-Cre* revealed labeled cone photoreceptors and a dozen neurons in the ganglion cell layer across the entire retina (Figure S1.1L-P). All transgenic mice were backcrossed into the *C57Bl/6J* background. Mice lacking either the Cre-recombinase or DTR or both, with either diphtheria toxin or saline injection, were used as littermate controls. Mice that had all 4 genotypes *OPN1SW-Cre or OPN1MW-Cre* x *Rosa26-loxP-stop-loxP-DTR* x *hLMcone-GFP or Ai6* x *Grm6-TdTomato* were used for cone ablations. Male and female mice were used for experiments. Between P30-35 mice were anesthetized with 1-4% isoflurane, weighed, and injected with diphtheria toxin at dosages of 100ng/g. Injections were made intramuscularly into the quadriceps. Double injections were given 1-4 days apart into the quadriceps

of different legs. The animals were monitored daily following diphtheria toxin injection. Mice survived for intervals between 3 days and 2 months following the second toxin injection.

Method details

Tissue preparation for immunostaining

Mice were euthanized by isoflurane overdose or carbon dioxide followed by cervical dislocation. The mice were enucleated and the retinas were dissected and mounted on nitrocellulose filter paper (Millipore) in bicarbonate-based Ames solution equilibrated with 95% O_2/5% CO_2. The orientation and sidedness of retinas were noted so that dorsal-ventral and temporal-nasal axes could be distinguished in the whole mount retina. The retinas were fixed in 4% paraformaldehyde for 15 min or 2% paraformaldehyde for 20 min at room temperature, rinsed in PBS, pH 7.42, then immersed in blocking solution (5% normal donkey serum, 0.5% Triton X-100 in PBS) overnight, incubated in primary antibodies for 5 days at 4°C, then rinsed in PBS and incubated in secondary antibodies for 1 day at 4°C, and rinsed with PBS and mounted with Vectashield underneath a coverslip. For quantification of cell types in sections, the whole eye was fixed in 4% paraformaldehyde for 90 min, 20 μm frozen sections were rinsed in PBS, incubated in primary antibodies for 1 day at 4°C, rinsed with PBS, incubated in secondary antibody for 1 hr at room temperature, rinsed with PBS, and mounted with Vectashield underneath a coverslip. Reagents are listed in the Key Resources Table.

Biolistic transfection

Mice were anesthetized by carbon dioxide overdose, euthanized by cervical dislocation, and enucleated. Retinas were dissected in oxygenated mouse ACSF and mounted whole on filter paper. DNA coated gold particles were prepared by coating 12.5 mg of 1.6 μm gold particles (Bio-Rad) with 20 μg of *CMV:CFP* and 7 μg of *CMV:PSD95-YFP* plasmids. A suspension of DNA-coated

gold particles in ethanol was precipitated onto the inner surface of Teflon tubing (Bio-Rad) and subsequently cut into 12-mm segments. A Helios gene gun (Bio-Rad) was used to biolistically deliver plasmid-coated gold particles to whole-mounted retinas. Gold particles were propelled onto the tissue using helium gas at 40 psi. Retinas were then transferred to an oxygenated and humidified chamber and maintained for 27 h at 30 deg C to allow fluorescent protein to be sufficiently expressed for subsequent imaging (Santina and Ou, 2018). Once sufficient expression was observed, retina were fixed in 4% paraformaldehyde for 15 min and immunostained according to the procedure described above.

Confocal imaging

To image type 6 bipolar cells, genetically-encoded fluorescence in the retinas was first viewed through the eyepieces using epifluorescence. Isolated type 6 bipolar cells were identified by their distinct axonal morphology (Dunn and Wong, 2012). Bipolar cells were chosen by high signal-to-noise ratio of the bipolar fluorescence without regard to the cone density in the immediate vicinity. Isolated bipolar cells in the retina were imaged on a Zeiss LSM700 confocal microscope or a Leica SP8 with the oil immersion 63x (NA 1.4) objective. High-resolution image stacks were taken of the bipolar dendrites with voxel sizes of 0.05-0.08 μm/pixel (x axis, y axis) and 0.2 μm/pixel (z-axis). Lower resolution image stacks were taken of the entire bipolar cell to verify cell type 0.10 μm/pixel (x axis, y axis) and 0.4 μm/pixel (z-axis). Each plane was acquired 2-4 times to obtain the average.

To image the biolistically-transfected ganglion cells, we identified cells with bright fluorescent expression first through the eyepieces using epifluorescence and mapped their location in the retina. To identify $A_{ON\text{-}S}$ ganglion cells, we chose ganglion cells with large polygonal somas colocalized with SMI-32 and whose dendrites stratified within the type 6 ON cone bipolar cell axon layer of

synaptotagmin-2 (Syt2) staining. We used the 40x (NA 1.3) objective on a Leica SP8 to acquire image stacks at 0.098 x 0.098 x 0.3 μm/pixel.

Electrophysiology tissue preparation

Mice were dark-adapted overnight. Dissections were performed in the dark with infrared illumination and image converters. Mice were euthanized by cervical dislocation and enucleated. Retinas were dissected in warmed bicarbonate-based Ames solution, equilibrated with 95% O_2/5% CO_2, and cut into halves or quadrants to keep track of sidedness and topography. To control for topographical variation in ganglion cell size, recordings were made in dorsal-nasal retina where the largest alpha ON-sustained ganglion cells (abbr. $A_{ON\text{-}S}$ ganglion cells reside (Bleckert et al., 2014). For patch-clamp recordings, retina quadrants were stored in a light-tight chamber with the retinal pigment epithelium attached in equilibrated bicarbonate-based Ames heated to 32 deg C for 30 minutes before recording. The retinal pigment epithelium was then removed, retina quadrants were mounted ganglion cell side up on glass coverslips and continuously perfused at 8-10 mL/min with equilibrated bicarbonate-based Ames heated to 35 deg C. After recordings, retina were mounted on filter paper and processed for immunostaining and imaging as described above.

Patch-clamp recordings

Patch electrodes were pulled from borosilicate glass (Sutter Instruments) on a DMZeitz or Narishige puller to 3 MOhm resistance. Cells in the ganglion cell layer were targeted based on their large polygonal somas visualized under infrared light (950nm). An empty patch pipette was used to dissect away the inner limiting membrane to expose cells for recording. Targeted cells were first recorded in cell-attached configuration with an electrode filled with HEPES buffered Ames. This configuration allowed for recording of extracellular spikes from the targeted cells. Following cell attached recordings, the same targeted cells were recorded in current clamp with a patch pipette filled with

internal solution containing (in mM): 104.7 cesium methane sulfonate, 10 TEA Cl, 20 HEPES, 10 EGTA, 2 QX-314, 5 ATP, 0.5 GTP, adjusted to pH 7.3 with CsOH and the 0.04% Lucifer Yellow dye. Signals were amplified with an Axopatch MultiClamp 700B amplifier (Molecular Devices, Palo Alto, CA), digitized with an Instrutech ITC-18, and acquired with Symphony.

Cell identification

$A_{ON\text{-}S}$ ganglion cells were identified during recording by their characteristic sustained spiking response to a 500ms light step. Putative $A_{ON\text{-}S}$ ganglion cells were confirmed after recording with immunolabeling for SMI-32, a neurofilament marker that labels alpha-type cells and for Syt2, a calcium sensor found in the axon terminals of type 6 ON cone bipolar cells, which co-stratify with the dendrites of $A_{ON\text{-}S}$ ganglion cells.

Light stimuli

Light stimuli were generated by a DLP Lightcrafter projector (Texas Instruments DLPLCR4500EVM). The projector stimulus had red, green, and blue LED (420-700nm) output more effective for driving M opsin than S opsin (Wang et al., 2011). Spatial stimuli were created in Stage and consisted of binary flickering bars (width of 40μm) whose intensity was drawn from a Gaussian distribution with mean intensity of 8,400 Rh*/rod/sec and standard deviation 0.3. Stimuli were generated from random seeds and were shown for 50 seconds.

Electroretinogram recordings

Mice were dark adapted overnight. On the day of experiment, mice were anesthetized with i.p. injection of Ketamine/Xylazine (80mg/kg, 10mg/kg, respectively) and positioned on the recording apparatus (Celeris, Diagnosys LLC, Gaithersburg, MD). Pupils were dilated using drops of 1%

tropicamide and corneas protected by application of a thin layer of methylcellulose. Body temperature was constantly maintained at 37°C with a heating pad.

Electroretinograms (ERGs) were recorded in complete darkness via coiled silver electrodes making contact with the moist cornea. A gold needle electrode was placed under the skin between shoulders to serve as both reference and ground. Responses were amplified differentially, band-pass filtered (0.1 to 500 Hz), digitized at 10 kHz and stored on disc for processing. Responses to flashes were averaged with an interstimulus interval ranging from 2s for dim lights to 10s for the brightest flashes. Five responses were averaged for each light intensity to eliminate electrical noise.

Full field illumination of the eyes was achieved with the miniaturized Ganzfeld spheres integrated with the recording electrodes (Celeris Bright RGB stimulators, Diagnosys LLC). Brief (10ms) white flashes were delivered under dark adapted and light adapted conditions, generating the typical flash ERG response ranging from 0.33 to 97 photons/$\mu m^2 s^{-1}$ (Makous, 1997). ERG waveforms were stored to disk and analyzed by measuring a- and b-wave amplitudes and their relative implicit times. The a-wave was measured from baseline to the trough of the first negative peak and the b-wave was measured from the a-wave peak to the peak of the large positive wave.

Quantification and statistical analysis

Image analysis of bipolar cells

Image stacks were median filtered (3 pixels). The bipolar cell, cone, and mGluR6 channels were interpreted into three-dimensional binary masks using Amira (FEI) (Dunn et al., 2013). The bipolar soma was separately masked in a single plane to determine the centroid of the bipolar cell. Each

cone within the bipolar cell's dendritic field was labeled with a unique identity. The binary masks were analyzed with custom-written routines in Matlab (Mathworks) for the volume overlap between bipolar dendrites and cones. Nonzero overlap between the bipolar cell and cone channel determined whether a contact was made. The binary mask was used to perform the following analyses manually: primary branch length, claw count, number of secondary branches, area of the dendritic and axonal territories. Primary branch lengths were analyzed in FIJI using Simple Neurite Tracer to trace the dendrite in three dimensions along the longest route from the soma to the dendritic tip. Claws were defined as any 3 branches within a 10μm diameter circle. Higher order branches (≥ secondary branches) were counted that fell outside a claw.

Quantification of cone numbers

To count cones in ganglion cell dendritic fields, image stacks were loaded into Imaris (Bitplane) and the Spots function was used. The count was checked and corrected manually.

Quantification of synaptic density

To measure the synaptic puncta within the bipolar cell axon, images of individual type 6 bipolar cell axons were binarized (Amira). Presynaptic CtBP2 puncta within the axonal region were manually counted in a maximum projection with FIJI's Cell Counter plug-in.

To measure ganglion cell dendritic arbor parameters and count postsynaptic puncta, images of individual $A_{ON\text{-}S}$ ganglion cells were skeletonized in Imaris and dendritic parameters were measured from a two-dimensional projection of the skeleton using custom Matlab routines (Santina et al., 2013). Dendritic area was defined as the area of the convex hull enclosing the dendritic arbor. Dendritic complexity was calculated using the Sholl analysis function within Imaris. To determine PSD95-YFP puncta distribution on dendrites of individual ganglion cells, we used a semiautomated

method for quantifying synapse density as previously described (Morgan et al., 2008), with modifications (Object Finder; Santina et al., 2013). ImageJ was used to median filter the images to remove the thermal noise from the microscope's photomultipliers. Using the 3D dendritic skeleton generated in Imaris, custom-written Matlab routines then created a binary mask to include PSD95-YFP signal only within the dendrites of the ganglion cell of interest. Details of candidate puncta identification and final validation are previously described (Santina et al., 2013). Linear density of puncta as a function of distance from the cell soma is calculated by quantifying puncta density along the dendritic skeleton within a moving window of 10 μm.

Quantification of cell death

To count photoreceptor and interneuron cell bodies, mice were euthanized and eyes enucleated and immediately immersed in cold fixative (2% PFA, 2.5% glutaraldehyde, and 0.1 M phosphate buffer, pH 7.4) for 24 hours, after which they were transferred to cold 0.1 M phosphate buffer and dehydrated in graded ethanol. Samples were embedded in Technovit 7100 Glycol Methacrylate (Electron Microscopy Sciences, Hatfield, PA) and serial sagittal sections (3μm) passing through the optic nerve were cut and stained with Hematoxylin and Eosin (H&E). For each retina, the number of cell bodies in the inner nuclear layer and outer nuclear layer was obtained by averaging four measurements taken from two cross sections from the same eye. Measurements from both nuclear layers were taken at equidistant points around the eye approximately 3/8 of the distance between the optic nerve and the periphery, i.e., slightly short of the midpoint. These values were used for statistical analysis for control and DTR conditions (Figure S1.1Q-T).

To visualize retinal cell populations in the flat mount and sectioned retina, we immunostained for bipolar (PKC alpha; Syt2), horizontal (calbindin), amacrine (syntaxin-1) and ganglion cells (RBPMS), and Muller glia (Sox9; GFAP) and microglia (Iba1; CD68). Quantification was either done in Fiji

with Cell Counter or in Imaris with Spots function. These values were used for statistical analysis for control and DTR conditions (Table S1.1).

Electrophysiology analysis: spatio-temporal receptive field maps

To measure the receptive field we followed Baccus et al. (Baccus and Meister, 2002). Briefly, the linear temporal filters were computed for the location in space of each of the bars of the stimulus by correlating the stimulus at that location over time with the response and dividing by the autocorrelation of the stimulus to normalize for a finite stimulus presentation. The nonlinearity was found by plotting the actual response amplitude by the predicted response amplitude and smoothing across neighboring points after sorting by the predicted response amplitude. The spatiotemporal receptive field maps were generated by arranging the temporal filters according to the corresponding spatial location of the stimulus.

To extract the spatial receptive field we used principal components analysis. All temporal filters were projected along the first principal component of the temporal filters (capturing at least 60% of the variance of the filters) to generate the cell's spatial receptive field. To increase the signal, particularly of the surround, we assumed that the spatial receptive field was symmetric and averaged the two sides of the receptive field about the midline. The resulting shape was fit with a difference of Gaussians. The parameters of this fit describe the size and weight of the center Gaussian and surround Gaussian and statistical tests were performed across control and DTR conditions (rank sum). Parameters were averaged and used to generate the average receptive field Gaussian, where w_c (w_s) is the center (surround) weights, and σ_c (σ_s) is the center (surround) standard deviation width.

For partial stimulation experiments (Figure 1.6), every other bar was held constant at the mean intensity value while neighboring bars varied in intensity. Subsequent analysis was identical to that

described above. Receptive field parameters were compared for the same cells stimulated with the full bar array or partially blanked bar array.

Statistical analysis

Data presented as median±interquartile range (IQR). Histograms are plotted with bin values to the left of each bar (Figures 1.1-1.4). Medians are indicated by arrowheads on top of the histograms. A Wilcoxon rank sum test (abbr. rank sum) was used to identify significant differences between conditions. A Wilcoxon sign rank test (abbr. sign rank) was used to identify significant differences between conditions with paired data (Figure 1.6). All p values are indicated in the Results. Asterisks in Figures indicate the following p values: * ≤0.05, **≤0.01, ***≤0.005.

Data and software availability

Software used to analyze the PSD95 puncta on ganglion cells can be found at https://lucadellasantina.github.io/ObjectFinder/. Software used to acquire physiology data can be found at https://github.com/Symphony-DAS/symphony-v1/wiki. Software used to drive the projector can be found at https://github.com/Stage-VSS/stage-v1.

Key Resources Table

REAGENT or RESOURCE	**SOURCE**	**IDENTIFIER**
Antibodies		
Rabbit polyclonal anti-calbindin	Swant	Cat# CB38; RRID: AB_2721225
Monoclonal mouse anti-CD68	Biorad	Cat# MCA1957; RRID: AB_322219

REAGENT or RESOURCE	SOURCE	IDENTIFIER
Goat anti-ChAT	Millipore	Cat# AB144P; RRID: AB_2079751
Rabbit polyclonal anti-cone arrestin	Millipore	Cat# AB15282; RRID:AB_1163387
Mouse monoclonal anti-CtBP2	BD Bioscience	Cat# 612044; RRID:AB_399431
Mouse monoclonal anti-GFAP	Biolegend	Cat# 835301; RRID: AB_2565344
Rabbit polyclonal anti-Iba1	Wako	Cat# 019-19741; RRID: AB_839504
Sheep polyclonal anti-mGluR6	Catherine Morgans, Kirill Martemyanov, Theodore Wensel	
Mouse monoclonal anti-PKCalpha	Sigma-Aldrich	Cat# P5704; RRID:AB_477375
Rabbit anti-RBPMS	Phosphosolutions	Cat# 1830; RRID: AB_2492225
Mouse monoclonal anti-SMI-32	Stenberger Monoclonals	Cat# SMI-32P; RRID: AB_2314912
Rabbit anti-Sox9	Millipore	Cat#AB5535; RRID: AB_2239761
Mouse monoclonal anti-synaptotagmin II	Zebrafish International Resource Center	Cat# znp-1; RRID: AB_10013783
Mouse monoclonal anti-syntaxin1	Sigma-Aldrich	Cat# S0664; RRID: AB_477483
Mouse monoclonal anti-Trpm1-274	Melina Agosto and Theodore Wensel	
Donkey polyclonal anti-rabbit-Alexa 488	Jackson Immunoresearch	Cat# 711-545-152; RRID:AB_2313584
Donkey polyclonal anti-sheep-Alexa 633	Molecular Probes	Cat# A21100; RRID:AB_10374307
Donkey polyclonal anti-mouse-Dylight 405	Jackson Immunoresearch	Cat# 715-475-150; RRID:AB_2340839

REAGENT or RESOURCE	SOURCE	IDENTIFIER
Donkey polyclonal anti-mouse-Alexa 647	Jackson Immunoresearch	Cat# 715-605-151; RRID:AB_2340863
Donkey polyclonal anti-sheep-Alexa 647	Jackson Immunoresearch	Cat# 713-605-147; RRID:AB_2340751
Donkey polyclonal anti-goat-Alexa 594	Jackson Immunoresearch	Cat# 705-585-147; RRID:AB_2340433
Donkey polyclonal anti-rabbit-Alexa 647	Jackson Immunoresearch	Cat# 711-605-152; RRID:AB_2492288
Rabbit polyclonal anti-red/green opsin	Millipore	Cat# AB5405; RRID:AB_177456
Goat polyclonal anti-OPN1SW	Santa Cruz Biotechnology	Cat# Sc-14363; RRID:AB_2158332
Chemicals, Peptides, and Recombinant Proteins		
Normal Donkey Serum	Jackson Immunoresearch	Cat# NC9624464
Ames' Medium	United States Biological	Cat# A1372-25
Gold particles/microcarriers (1.6μm diameter)	Bio-Rad	Cat# 165-2264
Vectashield	Vector Laboratories	Cat# H-1000; RRID: AB_2336789
Experimental Models: Organisms/Strains		
Mouse model: *Grm6-tdTomato*	(Kerschensteiner et al., 2009)	N/A
Mouse model: *C57BL/6-Gt(ROSA)26Sortm1(HBEGF)Awai/J (DTR)*	The Jackson Laboratory	Cat# JAX:007900; RRID:IMSR_JAX: 007900
Mouse model: *OPNSW1-Cre (BP-Cre)*	(Akimoto et al., 2004)	N/A
Mouse model: OPNMW1-Cre (*HRGP-Cre)*	(Le et al., 2004)	N/A
Mouse model:*B6.Cg-Gt(ROSA)26Sortm6(CAG-ZsGreen1)Hze/J (Ai6)*	The Jackson Laboratory	Cat# JAX:007906; RRID:IMSR_JAX: 007906

REAGENT or RESOURCE	SOURCE	IDENTIFIER
Mouse model: *hLMcone-GFP*	(Fei and Hughes, 2001)	N/A
Recombinant DNA		
Plasmid: pCMV-CFP	(Morgan et al., 2011)	N/A
Plasmid: pCMV-PSD95-YFP	A.M. Craig, University of British Columbia (Morgan et al., 2008)	N/A
Software and Algorithms		
ImageJ	NIH	https://imagej.nih.gov/ij/, RRID: SCR_003070
Amira	Thermo-Fisher Scientific	https://www.fei.com/software/amira-avizo/, RRID: SCR_014305
Imaris	Bitplane	http://www.bitplane.com/, RRID: SCR_007370
Matlab	Mathworks	https://www.mathworks.com/products/matlab.html, RRID: SCR_001622
Igor Pro	Igor Pro	RRID:SCR_000325
Object Finder	(Della Santina et al., 2013)	https://lucadellasantina.github.io/ObjectFinder/
Symphony and Stage	Mark Cafaro and Fred Rieke	https://github.com/Symphony-DAS/symphony-v1/wiki https://github.com/Stage-VSS/stage-v1

REFERENCES

Akimoto, M., 2004. Transgenic mice expressing cre-recombinase specifically in M- or S-cone photoreceptors. Invest Ophthalmol Vis Sci 45, 42–47.

Applebury, M., Antoch, M., Baxter, L., Chun, L., 2000. The murine cone photoreceptor a single cone type expresses both S and M opsins with retinal spatial patterning. Neuron 27, 513-523.

Atick, J.J., Redlich, A.N., 1990. Towards a theory of early visual processing. Neural computation 2, 308–320.

Baccus, S.A., Meister, M., 2002. Fast and slow contrast adaptation in retinal circuitry. Neuron 36, 909–919.

Beier, C., Hovhannisyan, A., Weiser, S., Kung, J., Lee, S., Yeong Lee, D., Huie, P., Dalal, R., Palanker, D., Sher, A., 2017. Deafferented adult rod bipolar cells create new synapses with photoreceptors to restore vision. Journal of Neuroscience 37, 4635–4644.

Bleckert, A., Schwartz, G.W., Turner, M.H., Rieke, F., Wong, R.O.L., 2014. Visual space is represented by nonmatching topographies of distinct mouse retinal ganglion cell types. Curr Biol 24, 310–315.

Buch, T., Heppner, F.L., Tertilt, C., Heinen, T.J.A.J., Kremer, M., Wunderlich, F.T., Jung, S., Waisman, A., 2005. A Cre-inducible diphtheria toxin receptor mediates cell lineage ablation after toxin administration. Nat Meth 2, 419–426.

Dunn, F.A., 2015. Photoreceptor ablation initiates the immediate loss of glutamate receptors in postsynaptic bipolar cells in retina. Journal of Neuroscience 35, 2423–2431.

Dunn, F.A., Santina, Della, L., Parker, E.D., Wong, R.O.L., 2013. Sensory experience shapes the development of the visual system's first synapse. Neuron 80, 1159–1166.

Dunn, F.A., Wong, R.O.L., 2012. Diverse strategies engaged in establishing stereotypic wiring patterns among neurons sharing a common input at the visual system's first synapse. Journal of Neuroscience 32, 10306–10317.

Enroth-Cugell, C., Freeman, A.W., 1987. The receptive-field spatial structure of cat retinal Y cells. J Physiol (Lond) 384, 49–79.

Eysel, U.T., 1982. Functional reconnections without new axonal growth in a partially denervated visual relay nucleus. Nature 299, 442–444.

Fei, Y., Hughes, T.E., 2001. Transgenic expression of the jellyfish green fluorescent protein in the cone photoreceptors of the mouse. Vis Neurosci 18, 615–623.

Han, D.P., Croskrey, J.A., Dubis, A.M., Schroeder, B., Rha, J., Carroll, J., 2012. Adaptive optics and spectral- domain optical coherence tomography of human photoreceptor structure after short-duration [corrected] pascal macular grid and panretinal laser photocoagulation. Arch. Ophthalmol. 130, 518–521.

Harding-Forrester, S., Feldman, D.E., 2018. Somatosensory maps. Handb Clin Neurol 151, 73–102.

Hata, Y., Tsumoto, T., Stryker, M.P., 1999. Selective pruning of more active afferents when cat visual cortex is pharmacologically inhibited. Neuron 22, 375–381.

Haverkamp, S., Michalakis, S., Claes, E., Seeliger, M.W., Humphries, P., Biel, M., Feigenspan, A., 2006. Synaptic plasticity in CNGA3(-/-) mice: cone bipolar cells react on the missing cone input and form ectopic synapses with rods. Journal of Neuroscience 26, 5248–5255.

Hickmott, P.W., Merzenich, M.M., 2002. Local circuit properties underlying cortical reorganization. J Neurophysiol 88, 1288–1301.

Horton, J.C., Hocking, D.R., 1998. Monocular core zones and binocular border strips in primate striate cortex revealed by the contrasting effects of enucleation, eyelid suture, and retinal laser lesions on cytochrome oxidase activity. J Neurosci 18, 5433–5455.

Jeon, C.J., Strettoi, E., Masland, R.H., 1998. The major cell populations of the mouse retina. J Neurosci 18, 8936–8946.

Johnson, R.E., Tien, N.-W., Shen, N., Pearson, J.T., Soto, F., Kerschensteiner, D., 2017. Homeostatic plasticity shapes the visual system's first synapse. Nat Commun 8, 1220.

Keck, T., Keller, G.B., Jacobsen, R.I., Eysel, U.T., Bonhoeffer, T., Hübener, M., 2013. Synaptic scaling and homeostatic plasticity in the mouse visual cortex in vivo. Neuron 80, 327–334.

Keck, T., Mrsic-Flogel, T.D., Vaz Afonso, M., Eysel, U.T., Bonhoeffer, T., Hübener, M., 2008. Massive restructuring of neuronal circuits during functional reorganization of adult visual cortex. Nat Neurosci 11, 1162–1167.

Keck, T., Scheuss, V., Jacobsen, R.I., Wierenga, C.J., Eysel, U.T., Bonhoeffer, T., Hübener, M., 2011. Loss of sensory input causes rapid structural changes of inhibitory neurons in adult mouse visual cortex. Neuron 71, 869–882.

Kerschensteiner, D., Morgan, J.L., Parker, E.D., Lewis, R.M., Wong, R.O.L., 2009. Neurotransmission selectively regulates synapse formation in parallel circuits in vivo. Nature 460, 1016–1020.

Le, Y.-Z., Ash, J.D., Al-Ubaidi, M.R., Chen, Y., Ma, J.-X., Anderson, R.E., 2004. Targeted expression of Cre recombinase to cone photoreceptors in transgenic mice. Mol Vis 10, 1011–1018.

Madisen, L., Zwingman, T.A., Sunkin, S.M., Oh, S.W., Zariwala, H.A., Gu, H., Ng, L.L., Palmiter, R.D., Hawrylycz, M.J., Jones, A.R., Lein, E.S., Zeng, H., 2009. A robust and high-throughput Cre reporting and characterization system for the whole mouse brain. Nat Neurosci 13, 133–140.

Makous, W.L., 1997. Fourier models and the loci of adaptation. J Opt Soc Am A Opt Image Sci Vis 14, 2323–2345.

Marc, R.E., Jones, B.W., 2003. Retinal remodeling in inherited photoreceptor degenerations. Mol Neurobiol 28, 139–147.

Michalakis, S., Schäferhoff, K., Spiwoks-Becker, I., Zabouri, N., Koch, S., Koch, F., Bonin, M., Biel, M., Haverkamp, S., 2012. Characterization of neurite outgrowth and ectopic synaptogenesis in response to photoreceptor dysfunction. Cell. Mol. Life Sci 70, 1831–1847.

Morgan, J.L., Schubert, T., Wong, R.O.L., 2008. Developmental patterning of glutamatergic synapses onto retinal ganglion cells. Neural Dev 3, 8.

Morgan, J.L., Soto, F., Wong, R.O.L. & Kerschensteiner, D., 2011. Development of cell type-specific connectivity patterns of converging excitatory axons in the retina. Neuron 71, 1014–1021.

Naoi, M., Maruyama, W., 1999. Cell death of dopamine neurons in aging and Parkinson's disease. Mech. Ageing Dev. 111, 175–188.

Okawa, H., Santina, Della, L., Schwartz, G.W., Rieke, F., Wong, R.O.L., 2014. Interplay of cell-autonomous and nonautonomous mechanisms tailors synaptic connectivity of converging axons in vivo. Neuron 82, 125–137.

Ratnam, K., Carroll, J., Porco, T.C., Duncan, J.L., Roorda, A., 2013. Relationship between foveal cone structure and clinical measures of visual function in patients with inherited retinal degenerations. Invest Ophthalmol Vis Sci 54, 5836–5847.

Reiter, H.O., Waitzman, D.M., Stryker, M.P., 1986. Cortical activity blockade prevents ocular dominance plasticity in the kitten visual cortex. Exp Brain Res 65, 182–188.

Santina, Della, L., Inman, D.M., Lupien, C.B., Horner, P.J., Wong, R.O.L., 2013. Differential progression of structural and functional alterations in distinct retinal ganglion cell types in a mouse model of glaucoma. Journal of Neuroscience 33, 17444–17457.

Santina, L.D., Ou, Y., 2018. Biolistic labeling of retinal ganglion cells. Methods Mol. Biol. 1695, 161–170.

Schwartz, G.W., Okawa, H., Dunn, F.A., Morgan, J.L., Kerschensteiner, D., Wong, R.O., Rieke, F., 2012. The spatial structure of a nonlinear receptive field. Nat Neurosci 15, 1572–1580.

Sher, A., Jones, B.W., Huie, P., Paulus, Y.M., Lavinsky, D., Leung, L.-S.S., Nomoto, H., Beier, C., Marc, R.E., Palanker, D., 2013. Restoration of retinal structure and function after selective photocoagulation. Journal of Neuroscience 33, 6800–6808.

Smirnakis, S.M., Brewer, A.A., Schmid, M.C., Tolias, A.S., Schüz, A., Augath, M., Inhoffen, W., Wandell, B.A., Logothetis, N.K., 2005. Lack of long-term cortical reorganization after macaque retinal lesions. Nature 435, 300–307.

Sorensen, S.A., 2006. The level and integrity of synaptic input regulates dendrite structure. Journal of Neuroscience 26, 1539–1550.

Soto, F., Ma, X., Cecil, J.L., Vo, B.Q., Culican, S.M., Kerschensteiner, D., 2012. Spontaneous activity promotes synapse formation in a cell-type-dependent manner in the developing retina. Journal of Neuroscience 32, 5426–5439.

Strettoi, E., Pignatelli, V., Rossi, C., Porciatti, V., Falsini, B., 2003. Remodeling of second-order neurons in the retina of rd/rd mutant mice. Vision Res 43, 867–877.

Strettoi, E., Porciatti, V., Falsini, B., Pignatelli, V., Rossi, C., 2002. Morphological and functional abnormalities in the inner retina of the rd/rd mouse. Journal of Neuroscience 22, 5492–5504.

Sweeney, L.B., Chou, Y.-H., Wu, Z., Joo, W., Komiyama, T., Potter, C.J., Kolodkin, A.L., Garcia, K.C., Luo, L., 2011. Secreted semaphorins from degenerating larval ORN axons direct adult projection neuron dendrite targeting. Neuron 72, 734–747.

Tien, N.-W., Soto, F., Kerschensteiner, D., 2017. Homeostatic plasticity shapes cell-type-specific wiring in the retina. Neuron 94, 656–665.e4.

Vessey, K.A., Greferath, U., Aplin, F.P., Jobling, A.I., Phipps, J.A., Ho, T., De Iongh, R.U., Fletcher, E.L., 2014. Adenosine triphosphate-induced photoreceptor death and retinal remodeling in rats. J Comp Neurol 522, 2928–2950.

Villa, K.L., Berry, K.P., Subramanian, J., Cha, J.W., Oh, W.C., Kwon, H.-B., Kubota, Y., So, P.T.C., Nedivi, E., 2016. Inhibitory synapses are repeatedly assembled and removed at persistent sites in vivo. Neuron 89, 756–769.

Wallace, H., Fox, K., 1999. The effect of vibrissa deprivation pattern on the form of plasticity induced in rat barrel cortex. Somatosens Mot Res 16, 122–138.

Wallace, H., Glazewski, S., Liming, K., Fox, K., 2001. The role of cortical activity in experience-dependent potentiation and depression of sensory responses in rat barrel cortex. Journal of Neuroscience 21, 3881–3894.

Wandell, B.A., Smirnakis, S.M., 2009. Plasticity and stability of visual field maps in adult primary visual cortex. Nat Rev Neurosci 10, 873–884.

Wang, Y.V., Weick, M., Demb, J.B., 2011. Spectral and temporal sensitivity of cone-mediated responses in mouse retinal ganglion cells. Journal of Neuroscience 31, 7670–7681.

Wässle, H., Puller, C., Müller, F., Haverkamp, S., 2009. Cone contacts, mosaics, and territories of bipolar cells in the mouse retina. Journal of Neuroscience 29, 106–117.

Wong, R.O.L., Ghosh, A., 2002. Activity-dependent regulation of dendritic growth and patterning. Nat Rev Neurosci 3, 803–812.

Zayit-Soudry, S., Duncan, J.L., Syed, R., Menghini, M., Roorda, A.J., 2013. Cone structure imaged with adaptive optics scanning laser ophthalmoscopy in eyes with nonneovascular age-related macular degeneration. Invest Ophthalmol Vis Sci 54, 7498–7509.

CHAPTER 2: MATURE RETINA COMPENSATES FUNCTIONALLY FOR PARTIAL LOSS OF ROD PHOTORECEPTORS

Summary

Loss of primary neuronal inputs inevitably strikes every neural circuit. How the deafferented circuit endures input loss determines the degree of deficit incurred by the output. This is poorly understood because of lack of control over ablation and access to circuit elements. Each neuron within a multi-layered circuit has the capacity to react to loss of input, resulting in an output that either amplifies or mitigates the input deficit, or leaves it unchanged. Here, we control the timing and degree of rod photoreceptor ablation in mature mouse retina and determine that there is compensation in well-defined pathways. Following loss of half the rods, rod bipolar cells mitigate this loss by preserving voltage output. Such compensation allows only partial recovery of responses in ganglion cells. We determine that rod death is compensated for in the retinal circuit because the ganglion cell response to stimulation of half of the rods in an unperturbed circuit is weaker than the response after death of half of the rods. The dominant mechanism of such compensation includes homeostatic regulation of inhibition to balance the loss of excitation.

Introduction

Degenerative diseases, injury, and normal aging can cause the death of primary neurons. Understanding the changes that happen in the resulting deafferented neural circuits is critical for diagnostic and therapeutic efforts to preserve and rescue function. Input loss may be propagated through a deafferented circuit, resulting in a decrease in output proportional to the decrease in input. Input loss may also be exacerbated, for example through degeneration of initially unaffected neurons, leading to a decrease in output more severe than the decrease in input. Alternatively, input loss may be compensated for within a deafferented circuit, resulting in a full or partial recovery of the output signal. To differentiate between these possibilities, we must investigate a circuit with known, controllable inputs and highly stereotypic outputs. Classic studies of the deafferented circuit have been done in the lesioned vestibular system. This literature describes compensation in vestibuloocular and vestibulospinal functions for input lost after removal of one vestibular labyrinth. Because the vestibular circuit integrates across multiple sensory systems, the origin of the compensation described remains unclear. To pinpoint the origin of compensation within a deafferented circuit we use the retina, a system with accessible interneurons.

In patients it is not known what the functional effects of partial rod loss are due to the difficulty of imaging rods. Research efforts in the retina have focused on models of rod degenerations which begin during development (Strettoi and Pignatelli, 2000; Marc and Jones, 2003; Haverkamp et al., 2006; Stasheff, 2008; Kerschensteiner et al., 2009; Puthussery et al., 2009; Soto et al., 2012; Margolis et al., 2014). However, degenerative diseases often begin after maturation is complete. To understand the mature retina's capacity to compensate for input loss, we need to dissociate developmental plasticity from input loss. Previous studies of input loss in mature retina have performed focal photoreceptor lesions and have demonstrated that ganglion cell spatial receptive fields fill in the

resulting scotoma (Sher et al., 2013; Beier et al., 2017). These findings suggest the mature retina may compensate for focal input loss, but the mechanisms and extent of such compensation remain unclear.

In this study, we induce death in about 50% of rod photoreceptors in mature mouse retina and measure function throughout the partially deafferented circuit to identify potential sites of compensation. We record the output of the retina from alpha ON sustained ganglion cells ($A_{ON\text{-}S}$ GCs) (Margolis and Detwiler, 2007; van Wyk et al., 2009; Krieger et al., 2017). These cells are arguably the most well-characterized and sensitive ganglion cells in the mouse retina and would therefore reflect changes in the retinal circuit at low light levels dominated by rod input (Murphy and Rieke, 2006; Margolis and Detwiler, 2007; van Wyk et al., 2009; Krieger et al., 2017). $A_{ON\text{-}S}$ GCs s also receive input from both rod and cone pathways. Light responses initiated by rods proceed via synaptic transmission to rod bipolar cells (RBCs) and then to AII amacrine cells, which are electrically coupled to ON cone bipolar cells (CBCs) (Figure 2.1A). The rod and cone pathways converge in the axon terminal of the CBC, which makes synapses onto ganglion cell dendrites. Here, we use these well-defined pathways to examine the consequences of rod death on the partially deafferented circuit.

We show that by the output of the retina, the $A_{ON\text{-}S}$ ganglion cells have largely compensated for 50% rod loss in their rod-mediated spikes and excitatory input currents. Perforated patch recordings allow us to eliminate ganglion cell intrinsic excitability as a possible mechanism of compensation. However, we localize compensation at the level of the rod bipolar cell, where significantly reduced excitatory input currents are compensated for by significantly reduced inhibitory currents which recover voltage outputs. Intriguingly, in the same $A_{ON\text{-}S}$ ganglion cells that show recovered rod-mediated light responses, cone-mediated light responses are enhanced, indicating that cone signaling

uses a common pathway with rods. Finally, in control retina responses of $A_{ON\text{-}S}$ ganglion cells to stimulation of 50% of rods are distinct from ablation of 50% of rods, allowing us to differentiate reduced rod input from subsequent compensatory changes within the partially deafferented circuit.

Results

Selective ablation of half of rod photoreceptors in mature mouse retina

To generate retina with partial rod loss, we injected diphtheria toxin (DT) into mice expressing the diphtheria toxin receptor (DTR) under the rhodopsin promoter at postnatal day 30 (Rho-DTR) (Figure 2.1A). In this system, rod death is dose-dependent, where two intramuscular injections of 100ng/g one week apart achieve death of about 50% of the rod population (Figure 2.1B). Control mice were either DTR-positive or -negative and were injected with saline. Rod death was confirmed in cross-sections of retina by quantifying the rows of somata present in the outer nuclear layer (ONL), which is composed of 95% rods (Jeon et al., 1998), Figure 2.1C). Two injections of DT consistently reduced the rod population by about 50% (Figure 2.1D, ONL) (Control 10.3±0.44, n=10; DTR 4.1±0.22 rows of somas, n=7; median±IQR, p=4.57e-05, rank sum). To examine off-target effects in this system, we also quantified the rows of somata present in the inner nuclear layer (INL), which is composed of bipolar and amacrine cell somas, and found no change after rod death (Figure 2.1D, INL) (Control 4.47±0.27, n=10; DTR 4.33±0.20 rows of somas, n=7; median±IQR, p=0.371, rank sum). Furthermore, when we crossed the Rho-DTR mouse line to a fluorescent reporter mouse line we found that fluorescence was confined to rods (Supplementary Figure 2.1). With this system that selectively ablates rods, we aimed to understand how the mature retina reacts to input loss. The retinal reaction to input loss may be understood functionally either as propagation, exacerbation, or compensation of such loss (Figure 2.1E). For instance, the functional effect of loss

of 50% of the rod input may be propagated through the circuit, resulting in a loss of 50% of the retinal output. This would be evident as a loss in sensitivity (Figure 2.1E, curve 1) or maximum amplitude (Figure 2.1E, curve 2). If, on the other hand, the functional effect in the circuitry is exacerbated from 50% input loss, then downstream neurons will likely perform worse than input loss alone predicts. Alternatively, the functional effect of 50% rod input loss may be compensated for within the circuit, i.e. by an increase in gain, resulting in a restoration of the retinal output. Compensation would be evident as a response equal to (Figure 2.1E, curve 3) or even greater than that of control (Figure 2.1E, curve 4). We discriminate among these possibilities by using the well-defined retinal pathways to $A_{ON\text{-}S}$ ganglion cells.

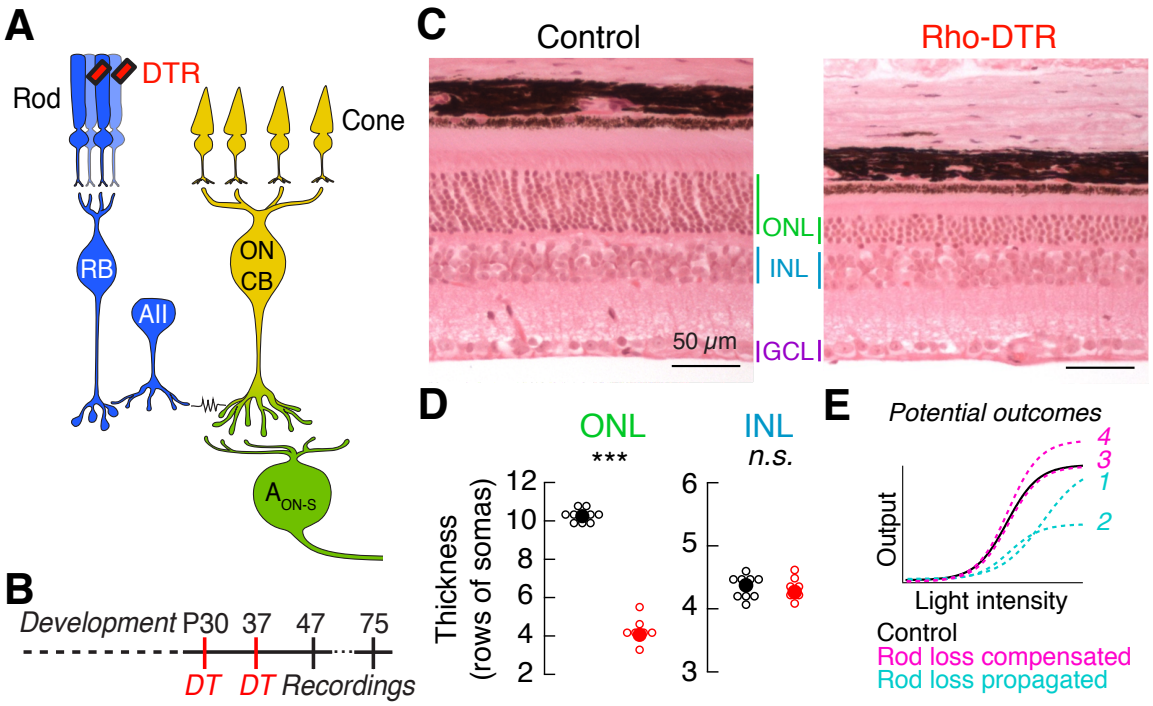

Figure 2.1. Diphtheria toxin receptor system ablates half the rod population while preserving inner retinal neurons in adult mice.
(A) Schematic of the primary rod bipolar cell pathway: rods → rod bipolar cells (RB) → AII amacrine cell (AII) → ON cone bipolar cells (ON CB) → ganglion cell, including the alpha ON sustained ganglion cell ($A_{ON\text{-}S}$). Rod-mediated signals (blue) and cone-mediated signals (yellow) converge at the synapses between ON cone bipolar cells and ganglion cells (green). Red rectangles indicate the expression of the simian diphtheria toxin receptor (DTR) driven under the promoter

for rhodopsin and selectively expressed in rods. Cartoons of the rod and cone photoreceptors are used in subsequent figures to denote the photoreceptor pathway stimulated and cartoons of the rod bipolar and ganglion cells are used to denote the cell type recorded.
(B) Time course of diphtheria toxin (DT) injection at postnatal day 30 (P30) and a second injection at P37 allows the retina to develop before ablation of rods.
(C) Retinal sections stained with Hematoxylin and Eosin with the retinal pigment epithelium on top in control (left) and Rho-DTR (right) conditions. Select retinal layers are labeled: outer nuclear layer (ONL) containing 95% rods, inner nuclear layer (INL) containing bipolar and amacrine cell bodies, and the ganglion cell layer (GCL) containing ganglion and displaced amacrine cell bodies.
(D) Quantification of the number of cell bodies in each column of the ONL and INL for control (black) and Rho-DTR (red) conditions. The number of cell bodies is only significantly different in the ONL. Points are median±IQR.
(E) Schematic of an ideal input-output relationship for light stimuli and functional responses within the retina. If the effects of rod ablation are propagated through the retinal circuit, then light responses postsynaptic to the rod could exhibit loss of inputs, e.g., decrease or loss of sensitivity in the response (curves 1 or 2). If, however, the effects of rod ablation are partially or fully compensated by postsynaptic neurons, then light responses postsynaptic to the rod could exhibit partial or full recovery, e.g., response that is greater than predicted based on the degree of rod loss (curves 3 or 4).

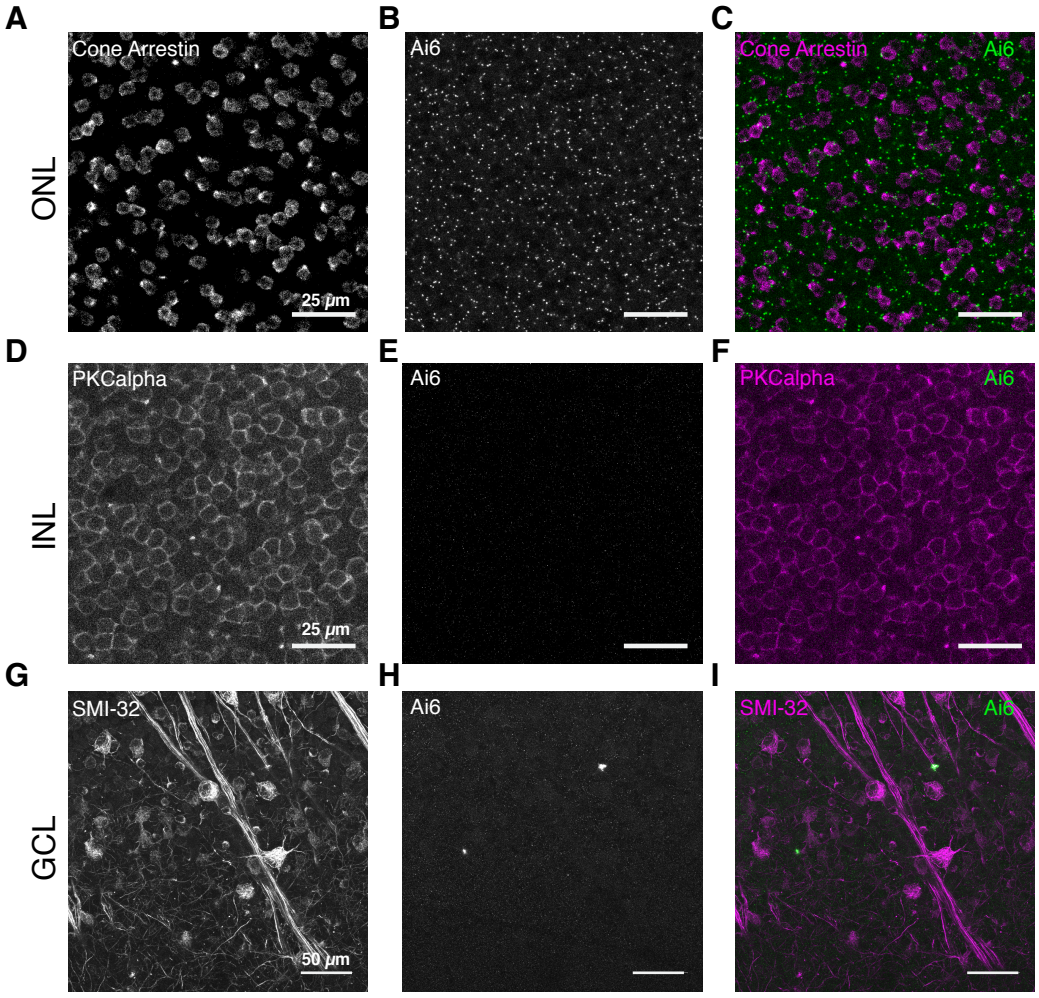

Figure S2.1. Diphtheria toxin system restricts diphtheria toxin receptor expression to rods. Related to Figure 2.1.
Confocal images of cell somas in the indicated layer from the *Rho-iCre x Ai6* mouse line.
(A) Cone somas labeled by cone arrestin in the outer nuclear layer.
(B) Rod somas that express Ai6 fluorescence.
(C) Overlay of cone arrestin (magenta) and Ai6 fluorescence (green). Ai6 expression is restricted to rods and not present in cones.
(D) Rod bipolar cell somas labeled by PKCalpha in the inner nuclear layer.
(E) Ai6 expression is absent from the inner nuclear layer.
(F) Overlay of PKCalpha (magenta) and Ai6 fluorescence (green).
(G) Alpha-type ganglion cells labeled by SMI-32 in the ganglion cell layer.
(H) Ai6 expression is absent from the ganglion cell layer.
(I) Overlay of SMI-32 (magenta) and Ai6 fluorescence (green).

After rod loss, rod-mediated charge and spiking output recover partially in $A_{ON\text{-}S}$ ganglion cells

To understand how rod pathways in mature retina react to the loss of 50% of rod input, we measured the output of the retina by recording rod-mediated spikes from $A_{ON\text{-}S}$ ganglion cells. To ensure constant cell size and response amplitude, we recorded exclusively from cells in ventral-nasal retina (Bleckert et al., 2014). To stimulate rods, we presented a stimulus series of 10-millisecond flashes of blue light (470nm) doubling in intensity from darkness. We used this stimulus in all studies reported here in which rods were stimulated. We recorded rod-mediated spike responses from control and Rho-DTR retina in cell-attached patch-clamp recordings (Figure 2.2A) and quantified responses by plotting the total number of spikes elicited by each flash in an intensity-response relationship (Figure 2.2B). We fit these data with the Hill equation and used the fit parameters to compare responses from control and Rho-DTR retina (Figure 2.2C, Supplementary Table 2.1). After the loss of 50% of rods, the rod-mediated spike response of $A_{ON\text{-}S}$ ganglion cells showed a decrease in the maximum response (R_{max}) and light intensity at half the maximum response ($I_{½}$). This indicates that after partial rod loss, the rod-mediated response of $A_{ON\text{-}S}$ ganglion cells has fewer spikes but is more sensitive. Such results could be consistent with the propagation of reduced rod

input through the mature retinal circuit. However, the average loss of rod-mediated spikes (by R_{max}, 22%) is less than the average loss of rods (50%), suggesting that compensatory mechanisms in the mature retinal circuit act to mitigate the functional effects of rod loss. Furthermore, the increase in sensitivity of the rod-mediated spikes suggests that gain of function can occur after partial rod loss.

To understand how these spike responses are generated, we next recorded the rod-mediated input currents onto $A_{ON\text{-}S}$ ganglion cells (Figure 2.2D,E). Excitatory current amplitude was unchanged, but the R_{max} of the integrated rod-mediated excitatory currents (charge) was reduced after partial rod loss (Figure 2.2F, Supplementary Table 2.1). This indicates that the amplitude or duration of rod responses are diminished. The reduced charge may explain the reduction in rod-mediated spikes that we observed. The charge transfer due to rod-mediated inhibitory currents did not change (Figure 2.2G-I, Supplementary Table 2.1). This indicates that rod-mediated inhibitory currents onto $A_{ON\text{-}S}$ ganglion cells are unaffected by partial rod loss.

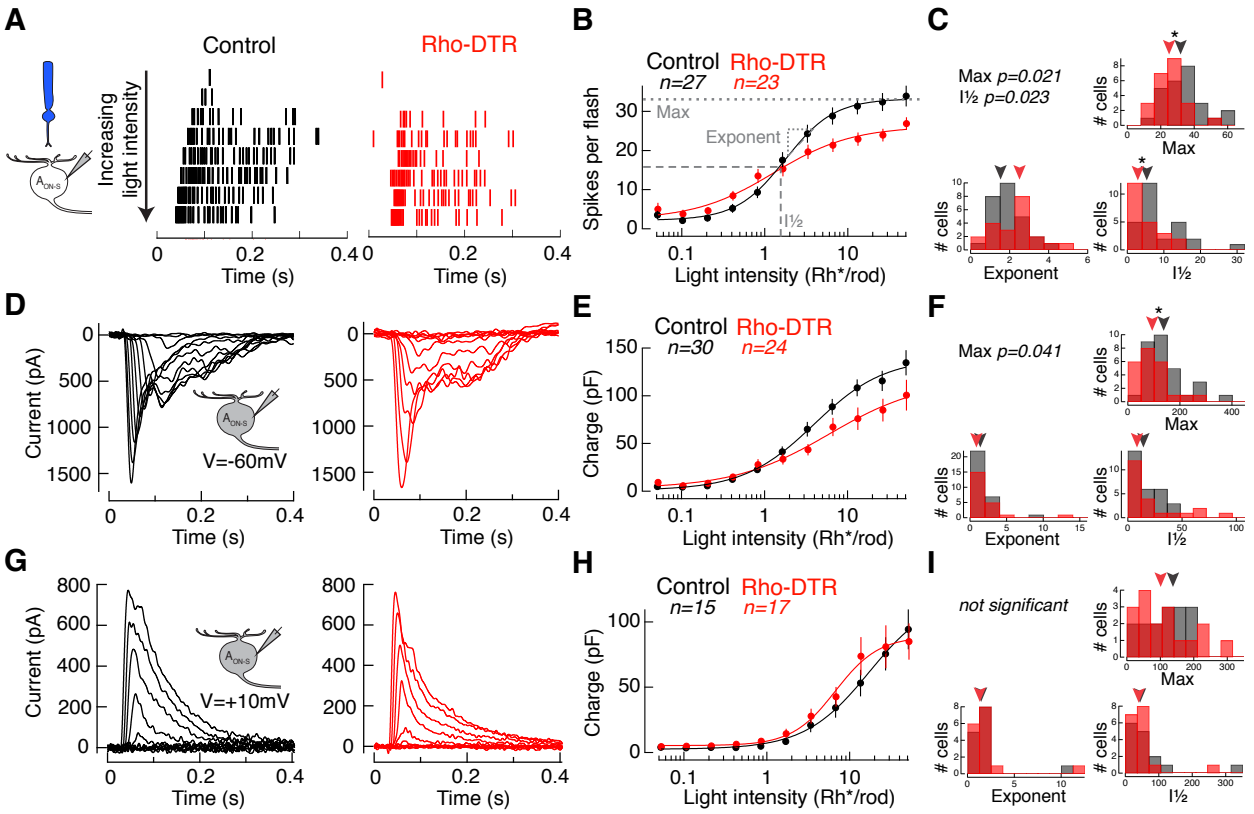

Figure 2.2. Rod-mediated light responses in $A_{ON\text{-}S}$ ganglion cells have partially recovered excitatory currents and spike output.

(A) Spike rasters from cell-attached recordings of $A_{ON\text{-}S}$ ganglion cells in response to a rod-preferring stimulus: 10ms flash at time 0 with the 470nm LED on a dark background. Each row shows the response to a flash doubling in intensity from top to bottom in control (black) and Rho-DTR (red) conditions.

(B) Average intensity-response relationship for the total number of spikes in response to each flash intensity. Points are mean±sem, n is number of cells. (B, E, H) Data points fit with a Hill equation, which can be captured by a maximum response (R_{max}), intensity at half maximum response ($I_{½}$), and exponent.

(C) Histogram of these three parameters of the fits for the population of $A_{ON\text{-}S}$ ganglion cells in control and Rho-DTR conditions. (C, F, I) Triangles above represent the median of each distribution and stars denote significant differences between control and Rho-DTR populations by the rank sum test. Significant p-values are reported in the upper left corner.

(D) Excitatory currents from voltage-clamped recordings of $A_{ON\text{-}S}$ ganglion cells (V = -60mV) in response to the same rod-mediated stimulus described above.

(E) Intensity-response relationship for the integral of the excitatory current.

(F) As described above for fits to the excitatory charge for individual cells.

(G) Inhibitory currents from voltage-clamped recordings of $A_{ON\text{-}S}$ ganglion cells (V = +10mV to +60mV, determined by reversal of the light response) in response to the same rod-mediated stimulus described above.

(H) Intensity-response relationship for the integral of the inhibitory current.

(I) As described above for fits to the inhibitory charge for individual cells.

Table S2.1. Parameters of rod-mediated $A_{ON\text{-}S}$ ganglion cell intensity-response curves fit with the Hill equation. Related to Figure 2.2.

		Control			DTR				
Figure number	**Figure panel**	**Measure**	**Median**	**IQR**	**Measure**	**Median**	**IQR**	**Statistical test**	**p-value**
2	C	R_{max}	32.85	14.6	R_{max}	25.49	12.2	Rank sum	0.022
		$I_{½}$	5.54	8.52	$I_{½}$	2.78	6.86		0.023
		Exponent	1.78	0.91	Exponent	2.44	1.56		0.083
	F	R_{max}	132.58	65.0	R_{max}	88.45	90.0		0.041
		$I_{½}$	14.02	20.4	$I_{½}$	11.94	46.5		0.924
		Exponent	1.63	0.97	Exponent	1.36	1.73		0.801
	I	R_{max}	124.82	316	R_{max}	99.65	419		0.706
		$I_{½}$	48.00	42.9	$I_{½}$	42.81	27.8		0.450
		Exponent	1.50	0.54	Exponent	1.38	0.47		1.000

At rod light levels intrinsic excitability is maintained in $A_{ON\text{-}S}$ ganglion cells after rod loss

One possible cause of a decrease in rod-mediated spikes is a change in current-to-spike transformation in the ganglion cell, i.e., intrinsic excitability. The transformation from currents to spikes includes voltage-gated conductances that are eliminated in the voltage-clamp recordings described above. Thus, to measure the current-to-spike gain in the cells for which intensity-response relationships were constructed, we calculated the ratio of the number of spikes to the peak charge elicited at each flash intensity (Figure 2.3A), for cells from which both spikes and currents had been recorded. A change in this ratio between control and Rho-DTR conditions would indicate that changes in voltage-gated conductances contribute to the observed decrease in spikes. We found no significant difference between the current-to-spike gain of cells from control and Rho-DTR retina at any of the flash intensities tested. This suggests that compensation for input loss is not due to changes in intrinsic excitability of $A_{ON\text{-}S}$ ganglion cells, but rather due to a change within the circuitry that provides input to those cells.

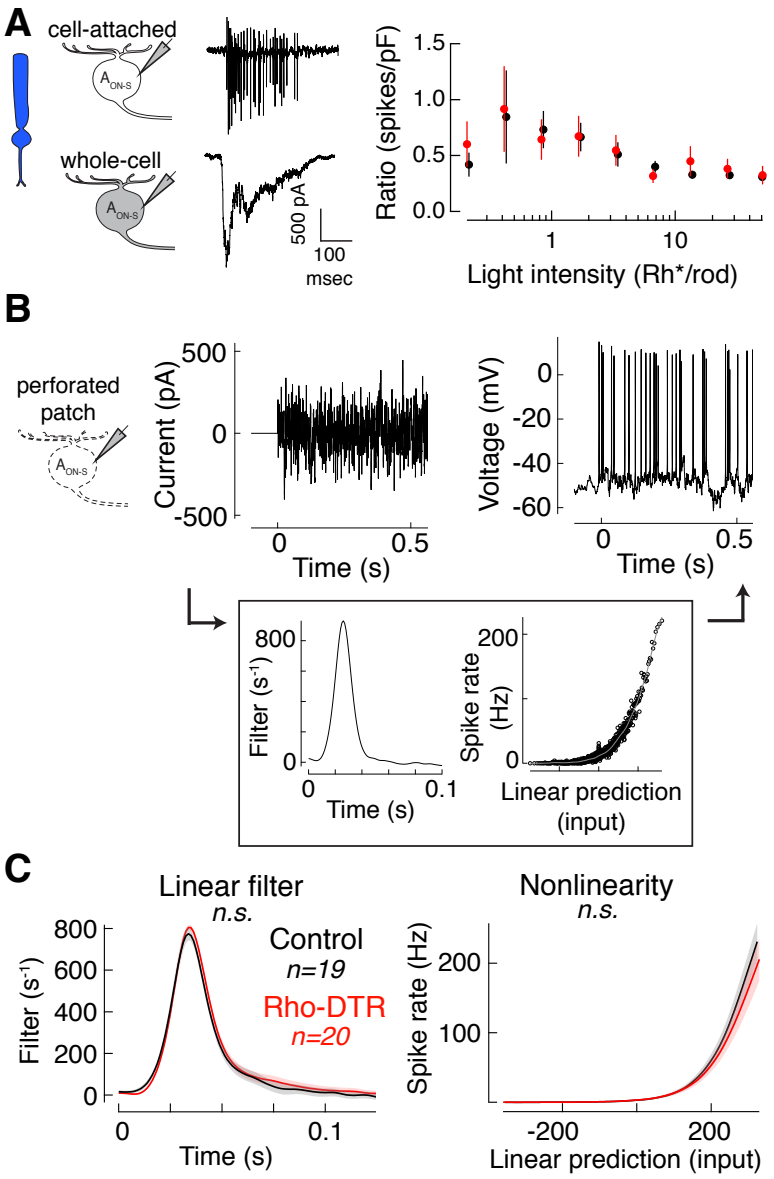

Figure 2.3. Intrinsic excitability of $A_{ON\text{-}S}$ ganglion cells is maintained at rod light levels after rod loss.

(A) Cartoons and example traces of the recordings used (left) in the calculation of the ratio of rod-mediated spike count to charge for each $A_{ON\text{-}S}$ ganglion cell in which both measurements were made sequentially in the same cell (right). Points are mean±sem.

(B) Test of intrinsic excitability. Example of current injected through the patch pipette (left) and the resulting spikes (right) recorded in perforated patch configuration. Background was kept dark during the duration of the current injections, which were 40 sec epochs ≥ 6 repeats. (box) Time-reversed spike-triggered average (left in box) and the nonlinearity for the example cell (right in box). Nonlinearity fit with a sigmoid function (grey).

(C) Time-reversed spike-triggered average (left) and average nonlinearity (right) of the linear-nonlinear model calculated from spike responses to white noise current injections (mean±SEM). For the nonlinearity, abscissa represents the convolution between the spike-triggered average and the

stimulus in units of standard deviation, i.e., linear prediction or generator potential. Ordinate represents the spike rate. The nonlinearity for each cell was interpolated and smoothed with a spline function. Permutation test shows that neither the linear filter nor nonlinearity are significantly different between control and Rho-DTR conditions.

The above observation was confirmed in a separate set of experiments, where we directly measured the current-to-spike transformation by injecting current into $A_{ON\text{-}S}$ ganglion cells in perforated patch-clamp configuration. This technique enables the simultaneous injection of a fluctuating white-noise current and measurement of the cell's spiking response (Kim and Rieke, 2001) (Figure 2.3B). To capture the current-to-spike transformation, we estimated the linear filter and nonlinearity that generated the spike response from the input current for each cell (Figure 2.3B, box). We found no significant differences in the linear filters or nonlinearities between cells from control and Rho-DTR retina in darkness, the condition that best simulates rods (Linear Filter: Control vs. DTR p=0.522; Nonlinearity: Control vs. DTR p=0.667; Control(DTR) n = 19(20), Permutation test). This result agrees with that from the current-to-spike ratio calculation and supports the conclusion that intrinsic excitability is maintained in $A_{ON\text{-}S}$ ganglion cells after rod loss. Therefore, we conclude that site(s) of compensation are prior to the ganglion cell.

The rod bipolar cell is a site of compensation

Next, we examined other potential site(s) of compensation within the retinal circuit, upstream of $A_{ON\text{-}S}$ ganglion cells. For a population readout of the responses of photoreceptors and bipolar cells, we measured the electroretinogram (ERG) *in-vivo* in control and Rho-DTR mice under scotopic (dark-adapted) conditions (Figure 2.4A). In Rho-DTR mice, we found a significant reduction in the a-wave amplitude of the scotopic ERG, a measure that is proportional to the rod dark current. This finding indicates an overall decreased rod response in Rho-DTR retina (Figure 2.4B). In contrast,

the amplitude of the b-wave, which is a measure proportional to the overall rod bipolar cell (RBC) and Müller glia cell responses, was maintained at these same light levels. This indicates that RBC output can be maintained despite a decrease in rod input (Figure 2.4C). This finding suggests that compensation for rod loss occurs between the inner segment of the rods and the voltage output of the RBCs, which could include the rod pedicle, the RBC postsynaptic sites and the current-to-voltage transformation within the RBC.

The same mice were also stimulated under photopic (light-adapted) conditions. In photopic conditions, in which the a-wave reflects cone activity and the b-wave reflects primarily ON cone bipolar cell responses, we observed no reduction in the amplitude of the a- or b-waves, indicating that population responses of cone photoreceptors and ON cone bipolar cells are not affected after 50% rod death (Figure 2.4D-F).

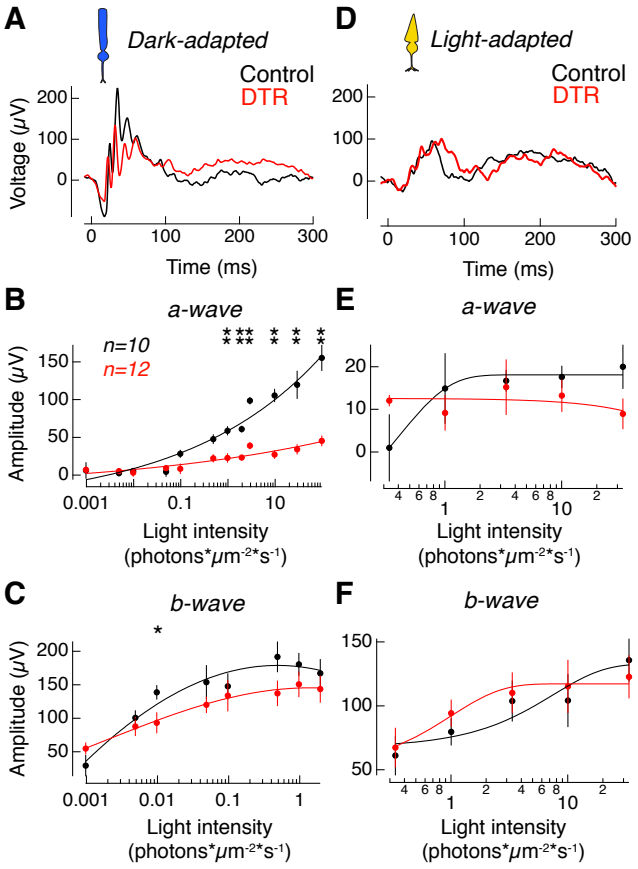

Figure 2.4. Rod-mediated responses compromised but postsynaptic and cone-mediated responses preserved in the ERG.
(A) Example *in vivo* electroretinogram (ERG) of control (black) and Rho-DTR (red) mice taken in the dark-adapted, rod-mediated condition at 2.919 photons*μm^{-2}*s^{-1}. Amplitude of a-wave was measured from baseline to the trough of the first negative peak. Amplitude of b-wave was measured from the trough of the first negative peak to the second-highest positive peak.
(B) Average amplitude of the dark-adapted a-wave, which is the rod-mediated voltage response in the waveform, as a function of light intensity. Points are mean±sem. Significant differences between response amplitudes at each light intensity are denoted by asterisks above each pair of points (t-test). (Light intensity [p-value]; 0.973 [0.030]; 1.946 [0.0173]; 2.919[0.0043]; 9.73 [0.0043]; 29.19 [0.0087]; 97.3 [0.0043])
(C) Average amplitude of the dark-adapted b-wave, which is the rod bipolar-mediated voltage response in the waveform, as a function of light intensity. Points are mean±sem. (Light intensity [p-value]; 0.04865 [0.030])
(D) Example *in vivo* ERGs taken in the light-adapted, cone-mediated condition.
(E) Average amplitude of the light-adapted a-wave, which is the cone-mediated voltage response in the waveform, as a function of light intensity. Points are mean±sem. No significant differences across light intensities.
(F) Average amplitude of the light-adapted b-wave, which is the ON cone bipolar-mediated voltage response in the waveform, as a function of light intensity. Points are mean±sem. No significant differences across light intensities.

Decreased excitatory and inhibitory input to rod bipolar cells yields a recovered voltage response

To further investigate the suggestion that compensation for rod loss occurs between the rod inner segments and the RBC voltage output, we recorded from RBCs directly. We measured rod-mediated responses from RBCs in whole-cell current-clamp and voltage-clamp configurations (Figure 2.5). Recordings were made in the slice preparation and confirmed in the whole-mount preparation. RBCs were identified by their location within the slice and ON-polarity light response in combination with current reversal at the reversal potential for inhibition. Similar polarity ON cone bipolar cells had light responses that could not be reversed at positive potentials because of gap junctions (Veruki and Hartveit, 2002). The peak amplitude of the rod-mediated response was used to construct intensity-response relationships for individual RBCs. As described for the ganglion cells, these curves were then fit with the Hill equation and the parameters for the best-fit curve were used

to compare across cells. After partial rod loss, we found no change in the peak amplitude of the voltage response of RBCs (Figure 2.5A-C, Supplementary Table 2.2). This aligns with results from the ERG and indicates that full compensation for the decreased rod input is achieved before the rod-mediated signal leaves the RBC.

To understand how this voltage response is generated, we measured the excitatory (Figure 2.5D-F) and inhibitory currents onto the RBCs under voltage-clamp configuration (Figure 2.5G-I). Following partial rod loss, we found a significant decrease in the R_{max} for both excitatory and inhibitory currents (Supplementary Table 2.2). Excitatory currents were reduced on average by 53%, which reflects the percentage of rod loss. Inhibitory currents were reduced on average by 94%. The nearly complete loss of inhibition indicates that the effect of rod loss on inhibition is greater than the loss of excitatory input.

One explanation for this enhanced response is that a compensatory mechanism is engaged to further reduce inhibition in order to balance reduced excitation. Alternatively, these data may suggest that inhibition is stimulated in an all-or-nothing manner. In addition to a loss of input, 50% rod death could also change the RBC response to remaining rods. Such a change would be evident as an increase or decrease in sensitivity, represented by the I½ parameter. We found no change in the sensitivity of excitatory currents, which suggests that the remaining rod-to-RBC synapses are unchanged, and that the site of compensation is the inhibitory currents. Here, we have found that a reduction in inhibition potentially balances the reduction in excitation due to rod loss, allowing RBCs in Rho-DTR retina to generate voltage outputs comparable to control retina.

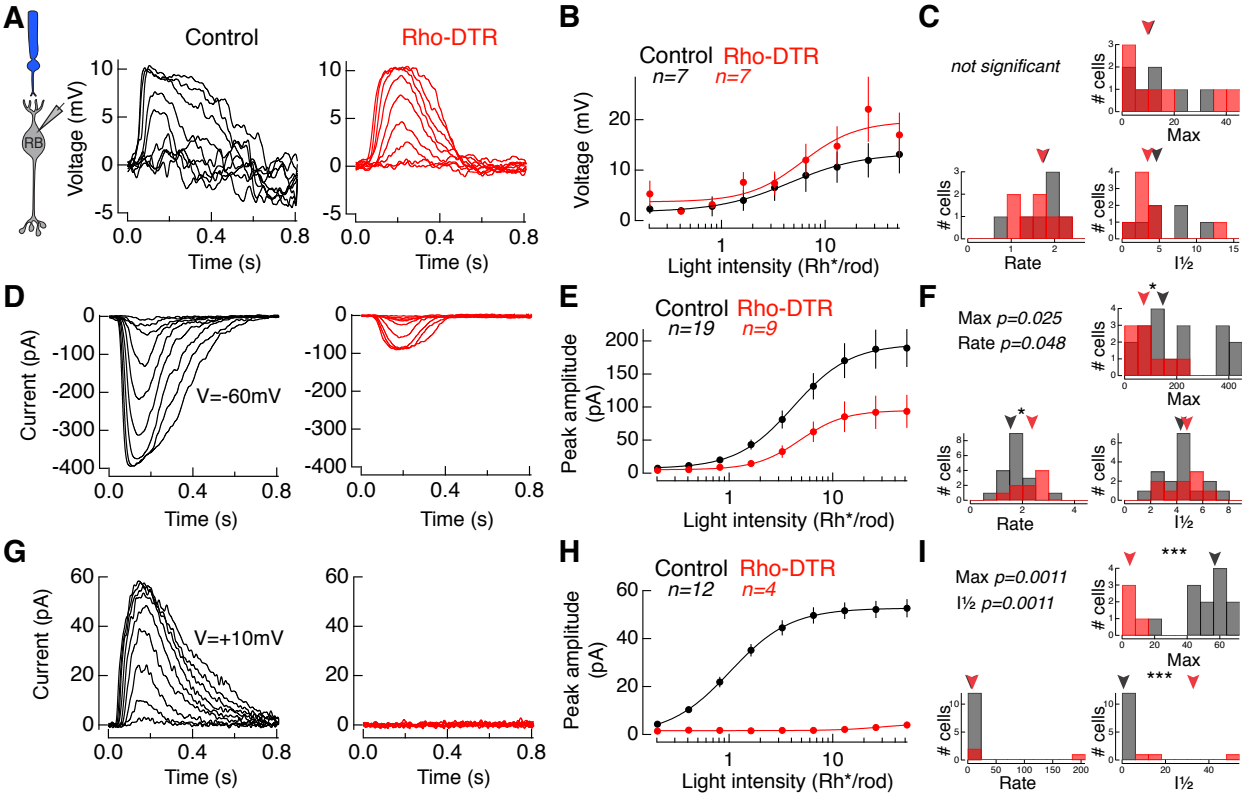

Figure 2.5. Compensated voltage responses in rod bipolar cells explained by diminished excitatory and inhibitory inputs.

(A) Example rod-mediated voltage responses to a family of flashes in rod bipolar cells in current clamp in control (black) and Rho-DTR (red) conditions.

(B) Average intensity-response relationship for peak voltage response at each light intensity across rod bipolar cells. Points are mean±sem. Data fit with a Hill equation.

(C) Histogram of these three parameters of the fits for the population of rod bipolar cell voltages in control and Rho-DTR conditions. (C, F, I) Triangles above represent the median of each distribution and stars denote significant differences between control and Rho-DTR populations by the rank sum test. Significant p-values are reported in the upper left corner.

(D) Example rod-mediated excitatory current responses to a family of flashes in rod bipolar cells under voltage-clamp (V = -60mV) in control (black) and Rho-DTR (red) conditions.

(E) Average intensity-response relationship for peak excitatory current responses at each light intensity across rod bipolar cells. Points are mean±sem. Data fit with a Hill equation.

(F) Histogram of these three parameters of the fits for the population of rod bipolar cell excitatory inputs in control and Rho-DTR conditions.

(G) Example rod-mediated inhibitory current responses to a family of flashes in rod bipolar cells under voltage-clamp (V = +10mV) in control (black) and Rho-DTR (red) conditions.

(H) Average intensity-response relationship for peak inhibitory current responses at each light intensity across rod bipolar cells. Points are mean±sem. Data fit with a Hill equation.

(I) Histogram of these three parameters of the fits for the population of rod bipolar cell inhibitory inputs in control and Rho-DTR conditions.

Table S2.2. Parameters of rod-mediated rod bipolar cell intensity-response curves fit with the Hill equation. Related to Figure 2.5.

		Control			DTR				
Figure number	**Figure panel**	**Measure**	**Median**	**IQR**	**Measure**	**Median**	**IQR**	**Statistical test**	**p-value**
5	C	R_{max}	10.31	9.41	R_{max}	10.12	21.6	Rank sum	0.955
		I½	4.28	4.42	I½	3.21	2.79		0.281
		Exponent	1.83	0.43	Exponent	1.70	0.89		1.000
	F	R_{max}	150.02	266	R_{max}	70.87	86.4		0.025
		I½	4.36	1.76	I½	4.81	2.08		0.777
		Exponent	1.65	0.60	Exponent	2.35	0.72		0.048
	I	R_{max}	56.52	16.8	R_{max}	3.48	7.34		0.001
		I½	0.93	0.63	I½	34.67	1.6e4		0.001
		Exponent	1.53	0.29	Exponent	6.41	164		0.170

To summarize thus far, after 50% rod death, the output of the rod population is reduced as measured in ERG, and both excitation and inhibition onto RBCs is reduced as measured in single-cell recordings. Consistent with the larger reduction in inhibition than in excitation, the voltage output of RBCs is maintained. The excitatory input onto $A_{ON\text{-}S}$ ganglion cells is thus partially recovered, which generates partially recovered spike responses to rod stimuli.

Cone-mediated charge and spiking output increase in $A_{ON\text{-}S}$ ganglion cells after rod loss

In the primary rod pathway, rod-mediated signals reach ganglion cells via the axon terminals of ON cone bipolar cells (CBCs) (Figure 2.1A). Thus, another possible site for alteration of signals through the primary rod pathway is at the cone bipolar to ganglion cell synapse. To isolate this section of the circuit, we used an S-cone-preferring stimulus composed of 10-millisecond flashes from a UV LED (370nm) doubling in intensity on a blue mean that adapts rods. To understand whether signaling through the cone pathway is affected by partial loss of rods, we first recorded the cone-mediated

spike response from $A_{ON\text{-}S}$ ganglion cells (Figure 2.6A-C). We found a significant increase in the R_{max} and I½ parameters over control as well as a decrease in the rate parameter describing the number of spikes per flash after partial rod loss (Supplementary Table 2.3). This finding indicates that the cone-mediated spike response is increased in amplitude and decreased in sensitivity after rod loss, and more generally, that the loss of rods affects signaling through the cone pathway. To further investigate the source of this increased spiking, we measured the cone-mediated excitatory (Figure 2.6D-F) and inhibitory (Figure 2.6G-I) currents onto $A_{ON\text{-}S}$ ganglion cells in response to the same stimulus. We found that cone-mediated excitatory currents, similarly to the cone-mediated spike output, showed an increase in R_{max} and decrease in the rate of charge transferred (Supplementary Table 2.3). Cone-mediated inhibitory currents showed no change after rod loss. This suggests that the increased spiking in response to cone-preferring stimuli may be driven by increased excitatory charge transferred between the ON cone bipolar and ganglion cell. Alternatively, the loss of rods might directly affect cone signals.

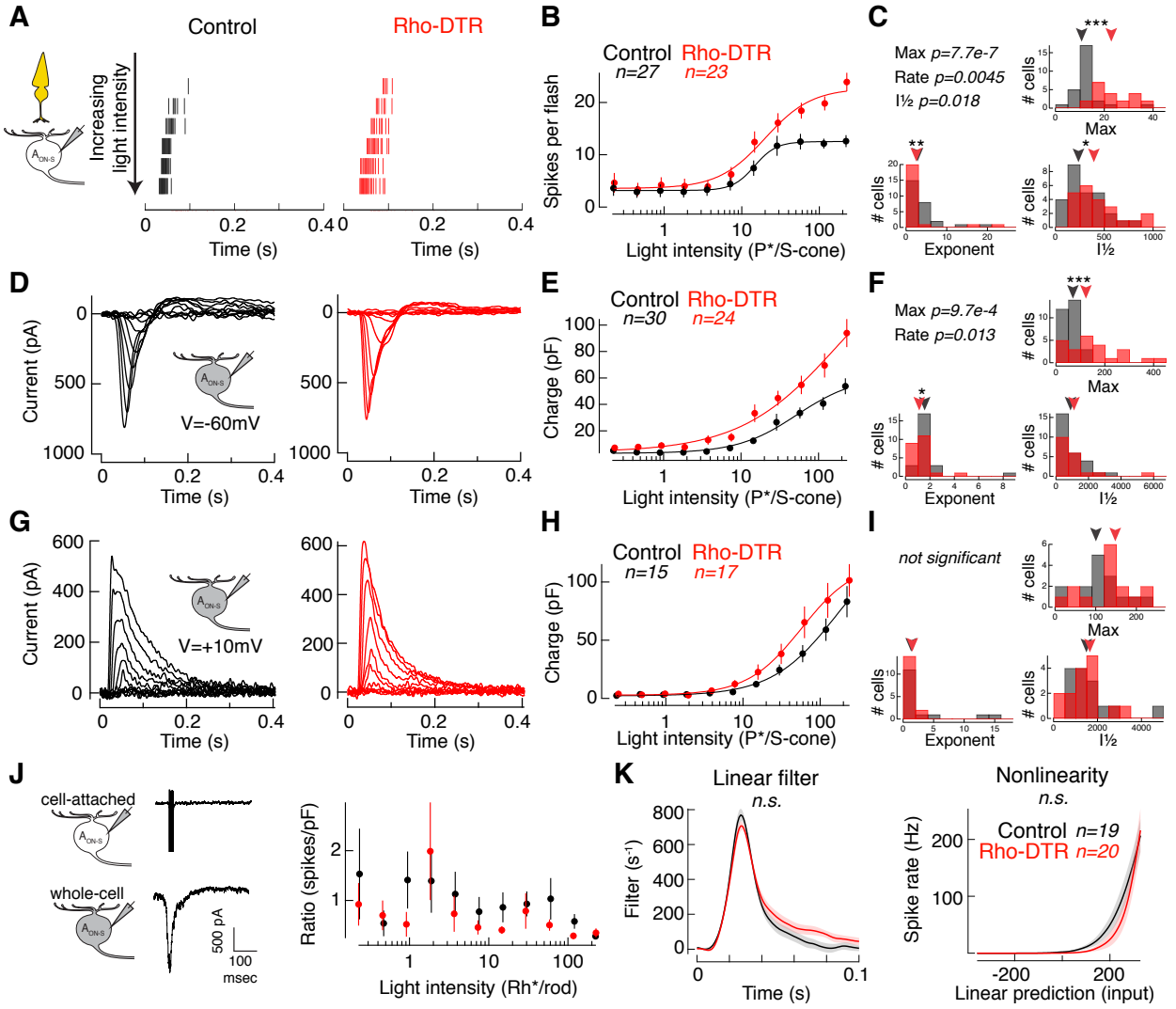

Figure 2.6. Cone-mediated spiking and input currents in $A_{ON\text{-}S}$ ganglion cells increase after rod loss.

(A) Spike rasters from cell-attached recordings of $A_{ON\text{-}S}$ ganglion cells in response to a cone-preferring stimulus: 10ms flash at time 0 with the 370nm LED on a mean of 4000Rh*/rod/sec produced by the 470nm to adapt down rods. Each row shows the response to a flash doubling in intensity from top to bottom in control (black) and Rho-DTR (red) conditions.

(B) Average intensity-response relationship for the total number of spikes in response to each flash intensity. Points are mean±sem. (B, E, H) Data points for each cell fit with a Hill equation, which can be captured by a maximum response (R_{max}), intensity at half maximum response (I½), and exponent.

(C) Histogram of these three parameters of the fits for the population of $A_{ON\text{-}S}$ ganglion cells in control and Rho-DTR conditions. (C, F, I) Triangles above represent the median of each distribution and stars denote significant differences between control and Rho-DTR populations by the rank sum test. Significant p-values are reported in the upper left corner.

(D) Excitatory currents from voltage-clamped recordings of $A_{ON\text{-}S}$ ganglion cells (V = -60mV) in response to the same cone-mediated stimulus described above.

(E) Intensity-response relationship for the integral of the excitatory current.

(F) Histogram of Hill equation fits to the excitatory charge for individual cells.

(G) Inhibitory currents from voltage-clamped recordings of $A_{ON\text{-}S}$ ganglion cells (V = +10mV to +60mV, determined by reversal of the light response) in response to the same cone-mediated stimulus described above.
(H) Intensity-response relationship for the integral of the inhibitory current.
(I) Histogram of Hill equation fits to the inhibitory charge for individual cells.
(J) Cartoons and example traces of the recordings used (left) in the calculation of the ratio of cone-mediated spike count to charge calculated for each $A_{ON\text{-}S}$ ganglion cell in which both measurements were made in the same cell (right). Points are mean±sem.
(K) Time-reversed spike-triggered average (left) and average nonlinearity (right) of the linear-nonlinear model calculated from spike responses to white noise current injections (mean±SEM). Blue mean of 4000Rh*/rod/sec was applied to adapt rods during the duration of the current injections. For the nonlinearity, abscissa represents the convolution between the spike-triggered average and the stimulus in units of standard deviation, i.e., linear prediction or generator potential. Ordinate represents the spike rate. The nonlinearity for each cell was interpolated and smoothed with a spline function. Permutation test shows that neither the linear filter nor nonlinearity are significantly different between control and Rho-DTR conditions.

Table S2.3. Parameters of cone-mediated $A_{ON\text{-}S}$ ganglion cell intensity-response curves fit with the Hill equation. Related to Figure 2.6.

		Control			DTR				
Figure number	**Figure panel**	**Measure**	**Median**	**IQR**	**Measure**	**Median**	**IQR**	**Statistical test**	**p-value**
6	C	R_{max}	11.99	2.64	R_{max}	23.29	16.4	Rank sum	7.7e-7
		I½	251.89	232	I½	384.52	315		0.018
		Exponent	2.76	1.74	Exponent	1.76	1.39		0.005
	F	R_{max}	71.75	60.5	R_{max}	122.03	140		0.001
		I½	692.73	1.0e3	I½	1168.7	3.5e3		0.233
		Exponent	1.69	0.83	Exponent	1.23	0.95		0.013
	I	R_{max}	105.96	569	R_{max}	148.46	388		0.141
		I½	1473.5	1.5e3	I½	1543.4	485		0.940
		Exponent	1.36	0.34	Exponent	1.62	1.48		0.910

We had previously eliminated the possibility that changes in intrinsic excitability in the $A_{ON\text{-}S}$ ganglion cells underlay changes in rod-mediated spikes. Here we examine the possibility that retinal neurons are in a different light-adaptation state at cone light levels, thus explaining the increased spiking in $A_{ON\text{-}S}$ ganglion cells. We compared the ratio of cone-mediated spikes to excitatory current responses and found no significant differences between control and Rho-DTR conditions (Figure

2.6J). Furthermore, we injected white noise current on top of a rod-adapting mean to measure the intrinsic excitability of $A_{ON\text{-}S}$ ganglion cells for cone-mediated signals and found no change in either the linear filter or the nonlinearity after rod loss (Linear Filter: Control vs. DTR p=0.125; Nonlinearity: Control vs. DTR p=0.410; Control (DTR) n = 12(12); Permutation test). Both these experiments demonstrate that the increased spiking does not arise from increased intrinsic excitability within the ganglion cell itself.

Partial stimulation of rods in control retina does not mimic rod-mediated light responses after partial rod death

We next aimed to understand whether the changes measured in the light response of $A_{ON\text{-}S}$ ganglion cells after 50% rod death reported above were purely the result of propagation of the effect of lost rod input through the retinal circuit or of active compensation for lost rod input. To answer this question, we designed an experiment to measure the retinal response to 50% of inputs without the contribution of any circuitry changes, e.g., caused by cell death or prolonged deficit of input. Control cells were stimulated with flashes spatially restricted to half the size of the full stimulus. The response to this half stimulus is a direct readout of 50% of inputs, thus providing a benchmark for what the light response in Rho-DTR retina might be if no compensatory mechanisms were active after the death of 50% of rods. Comparison of responses to the full and half stimulation against control and Rho-DTR retina reveals how the remaining partially deafferented circuit in Rho-DTR retina differs from control retina.

In the rod-mediated spike response to the half stimulus, we found a highly significant reduction in the R_{max}, indicating a decrease in response amplitude, as well as an increase in the $I_{½}$, indicating a decrease in sensitivity (Figure 2.7A-B). R_{max} decreased on average by 49% and the sensitivity

decreased on average by 52% (Supplementary Table 2.4), suggesting that stimulating half of rods generates a proportional decrease in response amplitude and sensitivity. In contrast, in Rho-DTR retina the R_{max} of the rod-mediated spike response decreased by only 22%, suggesting that compensatory mechanisms have partially recovered the response after rod death. Furthermore, the sensitivity of the spike response decreased with half stimulation but increased in Rho-DTR retina, a further indication that the Rho-DTR light response is not a passive readout of reduced rod stimulation. Since these rod-mediated responses to half stimulation differ from those in the Rho-DTR retina, these data demonstrate that stimulating 50% of rods is functionally distinct from killing 50% of them (Figure 2.7C).

Partial stimulation of cones mimics cone-mediated light responses after partial rod death

To understand whether the changes we observed in the cone-mediated light responses in Rho-DTR retina were caused by rod death or by subsequent compensatory mechanisms, we also presented cone stimuli in the full versus half stimulus experiment. To half stimulation we found an increase in the R_{max} and the I½ of the cone-mediated spike response in control retina (Figure 2.7D-E, Supplementary Table 2.4). This finding mimics the results from Rho-DTR retina, and therefore indicates that this increase in cone-mediated spiking is generated by a mechanism that is present in control retina and not a result of rod death. The half stimulation fails to replicate the condition of 50% rod stimulation and 100% cone stimulation, which occurs with Rho-DTR retina, because cones can only be selectively stimulated with the rod-adapting background. Instead the half stimulation achieves 50% rod stimulation and 50% cone stimulation. Despite this partial stimulation of cones, the result from of half stimulation is in line with the result from Rho-DTR retina (Figure 2.7F). In erring on the side of less cone stimulation than occurs in Rho-DTR retina, we are unable to make conclusions about the magnitude of this result, but we are able to conclude that cone-mediated

signaling increases in the absence of rod-mediated signaling. Results show that cone-mediated spiking in $A_{ON\text{-}S}$ GCs is enhanced after partial rod stimulation, similarly to partial rod death. These findings suggest that mechanisms which compensate for rod death are confined to the rod pathway.

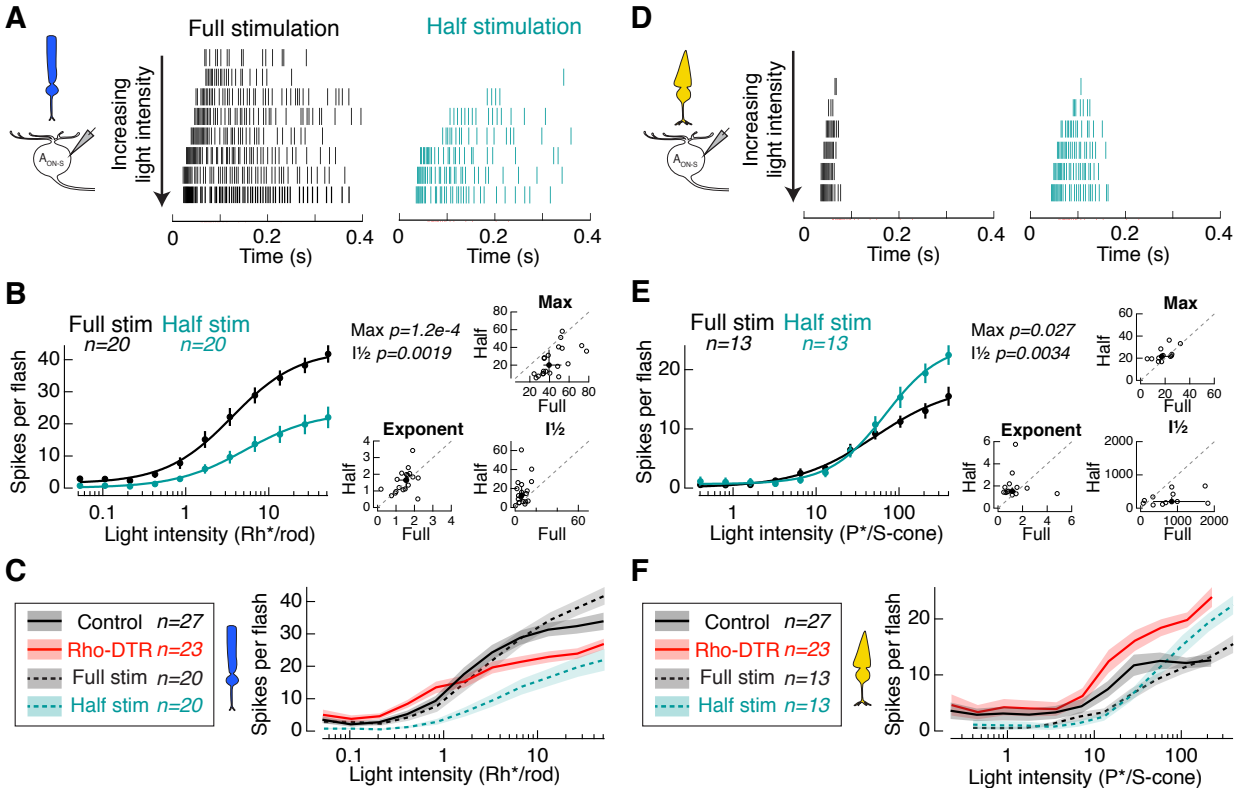

Figure 2.7. Half stimulation of control retina replicates cone- but not rod-mediated responses in Rho-DTR retina.

(A) Spike rasters from cell-attached recordings of $A_{ON\text{-}S}$ ganglion cells in response to the rod-preferring stimulus described previously. Each row shows the response to a flash doubling in intensity from top to bottom in full stimulation (black) and half stimulation (teal) conditions.

(B) (left) Average intensity-response relationship for the total number of spikes in response to each flash intensity. Points are mean±sem. (B, E) (left) Data points for each cell fit with a Hill equation, which can be captured by a maximum response (R_{max}), intensity at half maximum response ($I^1/_2$), and exponent. (right) Parameters of the fits for the $A_{ON\text{-}S}$ ganglion cells for which responses to both full and half stimulation were recorded in the same cell. (right) Individual cells (open circles) and median±IQR (closed circles with error bars). Dotted line indicates the line of slope unity. Significant p-values by the Wilcoxon sign rank test are reported in the upper left corner.

(C) Comparison of rod-mediated spike response from $A_{ON\text{-}S}$ ganglion cells from control retina (Control), control retina with full stimulation (Full stim), control retina with half stimulation (Half stim), and Rho-DTR retina indicates that Rho-DTR responses are partially recovered with respect to

cells receiving half stimulation. "Control" and "Full stim" are both control retinas stimulated with full stimuli but acquired as separate control datasets. Lines are mean±sem (shaded).
(D) Spike rasters from cell-attached recordings of $A_{ON\text{-}S}$ ganglion cells in response to the cone-preferring stimulus described previously. Each row shows the response to a flash doubling in intensity from top to bottom in full stimulation (black) and half stimulation (teal) conditions.
(E) (left) Intensity-response relationship for the total number of spikes in response to each flash. (right) Parameters of the fits for the $A_{ON\text{-}S}$ ganglion cells for which responses to both full and half stimulation were recorded in the same cell.
(F) Comparison of cone-mediated spike response from $A_{ON\text{-}S}$ ganglion cells displayed as in (C).

Table S2.4. Parameters of half-stimulated control $A_{ON\text{-}S}$ ganglion cell intensity-response curves fit with the Hill equation. Related to Figure 2.7.

		Full Stimulation			Half Stimulation				
Figure number	**Figure panel**	**Measure**	**Median**	**IQR**	**Measure**	**Median**	**IQR**	**Statistical test**	**p-value**
7	B	R_{max}	39.44	18.4	R_{max}	20.16	27.0	Sign rank	1.2e-4
		I½	1.24	1.38	I½	2.60	3.20		0.002
		Exponent	1.55	0.59	Exponent	1.66	0.88		0.332
	E	R_{max}	17.13	9.55	R_{max}	21.70	4.05		0.079
		I½	842.65	1414	I½	201.34	190		0.550
		Exponent	1.15	0.681	Exponent	1.53	0.47		0.502

Discussion

To understand the functional impact of partial rod death on the mature retinal circuit requires control over the timing and extent of rod death. In this study we induced death of 50% of the rod population long after development (Figure 2.1) and recorded the light response throughout the retina. In $A_{ON\text{-}S}$ GCs, we found partial recovery of excitatory current charge and the number of spikes elicited by rod stimuli (Figure 2.2). This recovery was not due to a change in intrinsic excitability of $A_{ON\text{-}S}$ GCs (Figure 2.3). *In vivo* electroretinograms showed that rod output is reduced by 50% but rod bipolar cell output is not significantly reduced (Figure 2.4). These results suggest that recovery happens after rod output and before rod bipolar cell output. We pursued these

possibilities by making whole-cell patch-clamp recordings from rod bipolar cells, which indicated that decreased excitatory and inhibitory currents may balance to generate recovered voltage responses (Figure 2.5). To probe the circuitry components that are part of both the primary rod pathway and the cone pathway, we measured the $A_{ON\text{-}S}$ ganglion cell light response to cone stimuli and found an increase in cone-mediated spiking, driven by increased excitatory current charge and not by a change in intrinsic excitability (Figure 2.6). Finally, we demonstrated that these changes in cone-mediated light responses after death of 50% of rods in Rho-DTR retina are similar to those that occur with stimulation of 50% of rods in control retina, indicating that cone signaling remains intact after 50% rod death. In contrast, we demonstrated that rod-mediated light responses in Rho-DTR retina differ from those that occur with half stimulation of control retina, indicating that after rod death the mature retina engages novel mechanisms to restore functional output (Figure 2.7).

Effects of cell death on the resting activity in the deafferented circuit

The vestibular system and our DTR system in the retina have similar features that make them exemplary systems in which to study input loss, including precise control over the extent of the lesion, deep literature on normal function, and highly quantifiable outputs. In the following sections, we draw comparisons between the compensation for input loss demonstrated in each system. In the work described here, we kill rod photoreceptors in order to uncover mechanisms induced early in degenerative diseases of the retina. However, the death of rod photoreceptors may have additional effects on the retina which may obscure understanding how the loss of neural input alone affects the retinal circuit.

An important feature of retinal circuit function is the resting release of glutamate by photoreceptors. The vestibular system similarly has resting activity which is reduced after

deafferentation (Shimazu and Precht, 1966; Hoshino and Pompeiano, 1977). The half stimulation experiment was designed to distinguish between the effects of partial photoreceptor stimulation and partial photoreceptor ablation (Figure 2.7). Features present in responses from Rho-DTR retina, but absent in responses from control retina under half stimulation, may be due to rod death rather than the absence of rod signaling. It is also possible that further confounds may arise from the spatial continuity of the half stimulation condition. To more accurately capture the spatially uniform loss of rods as occurs in Rho-DTR retina, we would need to uniformly present 50% as much light. However, this would mean that rods present do not receive the same stimulus as in the Rho-DTR condition, thus making the results difficult to interpret. Instead, we performed half-stimulation by spatially segregating the stimulus and interpret results by considering the retina's adaptation states. The half stimulation of control retina and half rod ablation in the Rho-DTR had distinct consequences that allow us to draw conclusions about the partially deafferented circuit. We consider three conditions: (1) full stimulation of control retina, (2) half stimulation of control retina, and (3) full stimulation of Rho-DTR retina. First, we consider rod-mediated, then cone-mediated light responses.

In signaling rod-mediated light responses on a dark background, Rho-DTR is missing rods that would otherwise convey resting activity to the remainder of the retina. As a prediction, the Rho-DTR (condition 3) would be in a relatively light-adapted state, as compared to half stimulation of control retina (condition 2), because only half the resting activity is being conveyed by the remaining rods. In the absence of compensation, the expectation is that the Rho-DTR ganglion cells would have lower sensitivity and faster responses, both signatures of a light-adapted retina. Indeed, ganglion cells in Rho-DTR retina have rod-mediated responses that are faster. In addition, Rho-DTR ganglion cells have rod-mediated responses that are more, rather than less, sensitive, indicating that the deafferented circuit is compensating for the ablated rods.

In signaling cone-mediated light responses on a mean background, Rho-DTR mice are missing rods that would convey the mean background to the rest of the retina. In contrast, the half stimulation control retina has only half of its rods stimulated by the mean background, while the other half of rods convey darkness. As a prediction, half stimulation of control retina (condition 2) would be the most dark-adapted due to the presence of these rods in the dark, and full stimulation of control retina (condition 1) would be the least dark-adapted. Indeed, ganglion cells in both the half stimulation (condition 2) and Rho-DTR (condition 3) have greater sensitivities and qualitatively slower responses, both signatures of dark-adapted retina, than the full stimulation control (condition 1). In addition, the response in Rho-DTR (condition 3) shows greater sensitivity than those in the half stimulation (condition 2), despite the expectation that Rho-DTR is in a less dark-adapted state, providing further evidence for changes that occur after rod death but are not present after half stimulation.

The physical absence of a subset of rods can affect electrically coupled rods and cones as well as change horizontal cell feedback onto cones. Importantly, we did not observe cone death as a result of rod death, but may observe this at higher levels of rod death or more prolonged observation (Aït-Ali et al., 2015). Future studies to disentangle these phenomena could compare the effects of killing rods to the effects of silencing rods, for example in the *Gnat1-/-* mouse which lacks a functioning transducin in the photosensing cascade (Calvert et al., 2000). Importantly, rods would have to be silenced after normal development of the retina. To determine if photoreceptor activity influences recovery, one could place animals in fully light or dark environments after photoreceptor loss. Similar studies of vestibular lesions have shown that recovery is impaired when animals are deprived of sensory input after the lesion and improved when animals are subjected to training after the lesion (Putkonen et al., 1977; Schaefer and Meyer, 1974; Lacour and Xerri, 1981). Such studies would address whether functional compensation in the retina is activity dependent, which may

provide guidance for training regimes for patients with retinal degeneration, an avenue of therapy which is being actively pursued using virtual reality.

Influence of input loss on inhibitory circuits

A strength in our study is the access we have to the retinal circuit. In contrast to the vestibular system which integrates across multiple sensory inputs, we can measure functional output generated solely within the retina. By recording directly from photoreceptors, bipolar cells, and ganglion cells, we are able to pinpoint the site of compensation for input loss in Rho-DTR retina to the inhibitory currents onto the rod bipolar cell. Rod bipolar cells have excitatory currents reduced by 53%, and inhibitory currents reduced on the order of 94%. This dramatic effect of partial input loss on inhibitory currents could be the result of decreased drive of the inhibitory circuitry due to rod death, since 70% of the inhibitory inputs onto rod bipolar cells come from reciprocal feedback via the A17 amacrine cell. Alternatively, the decrease could be due to a homeostatic reduction that maintains the excitatory to inhibitory balance of currents onto the rod bipolar cell. Future studies will distinguish between these possibilities. Regardless of mechanism, the end result is that more distal sites of compensation in the rod pathway are obviated by recovery at the rod bipolar cell voltage.

Following input loss, inhibition is similarly decreased in the vestibular system (Shimazu and Precht, 1966; Markham et al., 1977). Previous work in visual cortex has also demonstrated that inhibitory circuits exhibit more structural plasticity than excitatory circuits after monocular deprivation (Villa et al., 2016). Similarly, our previous study on partial cone loss revealed that inhibitory surrounds of $A_{ON\text{-}S}$ GCs expanded, while excitatory centers of these same cells shrank, indicating not only that the inhibitory surround is affected by partial cone loss, but that it may also be a site of

compensation for input loss (Care et al., 2019). Consistent with these results, inhibition at the rod bipolar cell axon terminal is implicated as a dominant mechanism of compensation. In contrast to these findings, the present study demonstrates a situation where the inhibitory circuits onto ganglion cells remain relatively stable. The difference between our previous study with cone ablation and present study with rod ablation could be due to the relatively greater influence of inhibition on cone vs. rod processing, the larger proportion of cells lost in rod ablation than in cone ablation, or the greater convergence present in rod pathways than in cone pathways (Enroth-Cugell and Freeman, 1987).

Implications for diagnosis of sensory input loss

Our work provides evidence for the independence of rod and cone pathways despite the convergence at the cone bipolar-to-ganglion cell synapse. When rods are ablated, cone-mediated responses in ganglion cells in a control retina can be mimicked with half stimulation, i.e., the cone pathway remains intact. Such findings, alongside evidence for compensation within the deafferented circuit, may explain why photoreceptor degeneration evades detection both by the patient reporting vision loss and by diagnostics of visual sensitivity and acuity (Ratnam et al., 2013). Greater than half of the cones must be missing before visual deficits start to present clinically. In our simulation of photoreceptor loss by partial stimulation, we have uncovered how the deafferented retinal circuit, while generally functional, differs from that of an unperturbed retina. One prediction is that at a single background, changes in kinetics and sensitivity following photoreceptor loss may be subtle enough to be mistaken for normal. However, if threshold detection is measured at multiple backgrounds, photoreceptor loss may present as kinetic or sensitivity changes that are consistent with a more light-adapted state than expected in unperturbed retina. These predictions require that the rest of the visual system has not masked changes at the level of the retina or that the method of

testing isolates retinal responses, e.g., electroretinogram. The present study has the potential to link mechanistic insight gained from mouse retina to clinically relevant efforts to create diagnostic tests for earlier detection of photoreceptor loss.

Experimental Procedures

Experimental model and subject details

Mice

All procedures were done in accordance with the University of California, San Francisco Institutional Animal Care and Use protocols. The following transgenic mouse lines were crossed: *Rho-iCre* (Li et al., 2005) for Cre-recombinase expression in rods and *Rosa26-loxP-stop-loxP-DTR* (Buch et al., 2005) for Cre-dependent expression of the diphtheria toxin receptor. When crossed to a fluorescent reporter line *Ai6* (Madisen et al., 2009), the *Rho-iCre* revealed high specificity to the rod population, with no cone pedicles and extremely rare cell bodies in the inner nuclear layer and ganglion cell layer labeled (Supplementary Figure 2.1). These transgenic mice were backcrossed into the *C57Bl/6J* background. Male and female mice were used for experiments. Diphtheria toxin injections were done between P30-40 at dosages of 100ng/g for 2 injections administered 7 days apart (Care et al., 2019). Mice injected with an equivalent volume of saline were used as littermate controls.

Method details

Tissue preparation for immunostaining

Immunostaining protocols were identical to those described in Care et al. (Care et al., 2019). Reagents are listed in the Key Resources Table.

Electrophysiology tissue preparation

Procedures for the flat mount preparation of recording from alpha ON-sustained ganglion cells (abbr. $A_{ON\text{-}S}$ ganglion cells) (Bleckert et al., 2014) and rod bipolar cells were identical to those described in Care et al. (Care et al., 2019). Recordings were done in ventral-nasal retina where the largest of the $A_{ON\text{-}S}$ ganglion cells reside and where short (S)-wavelength sensitive opsin dominates.

Procedures for slice preparation for recording from rod bipolar cells were similar to those described (Dunn et al., 2006). Briefly, the isolated retina was embedded in 3% low melting agar in oxygenated HEPES buffered Ames and sliced at 200μm sections on a Vibratome 1200S (Leica). Slices were chosen based on the accessibility of the rod bipolar cells and the intactness of the entire section.

Patch-clamp recordings

Patch-clamp recordings from ganglion cells were identical to those described in Care et al. (Care et al., 2019). Patch-clamp recordings from rod bipolar cells were made with electrodes pulled from borosilicate glass (Sutter Instruments) on a DMZeitz to 10-15 MOhm resistance. The electrode internal solution was either cesium methane sulfonate (Care et al., 2019). or potassium aspartate containing (in mM): 125 potassium aspartate, 1 MgCl, 10 KCl, 1CaCl, 10 HEPES, 2 EGTA, 4 ATP, 0.5 GTP, adjusted to pH 7.2 with KOH, adjusted to 273-279 mosm with potassium aspartate, and 0.04% Lucifer Yellow dye.

Cell identification

Identification of $A_{ON\text{-}S}$ ganglion cells included sustained spiking response to a 500ms light step and immunolabeling described in Care et al. (Care et al., 2019).

Rod bipolar cells were targeted by the soma location in the outermost layer of the inner nuclear layer, next to the outer plexiform layer. Identification of rod bipolar cells included ON light responses that could be reversed at positive holding potentials and immunolabeling that revealed large axon terminals in the innermost layer of the inner plexiform layer and colocalization with protein kinase C alpha (PKCalpha).

Light stimuli

Light stimuli were generated by three LEDs with single peaks at 390nm, 405nm, and 470nm. For rod-mediated stimuli, a 10ms flash of the 470nm was presented on a dark background. For cone-mediated stimuli, a 10ms flash of the 370nm or 405nm LEDs was presented on a mean background of 4000 rod isomerizations per rod per second (Rh*/rod/sec) to adapt the rods.

Electroretinogram recordings

Procedures for the electroretinograms (ERGs) were identical to those described in Care et al. (Care et al., 2019) with the following differences. Diagnosys LLC is located in Lowell, MA. The b-wave amplitude was measured from the peak of the a-wave to the second highest positive peak to avoid confounds due to the oscillatory potentials which occur during the b-wave.

Quantification and Statistical Analysis

Quantification of intensity response relationship

Responses of each cell were measured 5-10 times at each light level. Analysis parameters (number of spikes, peak current amplitude, charge) were measured for each individual response and averaged at each light level within each cell. For each cell, these averages were plotted against the light intensity which elicited the response and the resulting plot was fit with the Hill equation in Igor Pro:

The parameters of this fit (max (referred to as Rmax), rate (referred to as Exponent), xhalf (referred to as I½) are shown as histograms in Figures 2.2, 2.5, and 2.6. To construct the average intensity response plots in panels B, E, and H of these figures, as well as the left side of panels B, E in Figure 2.7, the average intensity response plots generated for each cell before the Hill equation fit were averaged. Points at light intensities within 30% of each other were combined (shown with horizontal error bars which are too small to extend beyond the point marker in most cases).

Linear-Nonlinear Filters

To determine the intrinsic excitability of $A_{ON\text{-}S}$ ganglion cells, we made perforated current-clamp recordings with a patch pipette filled with internal solution containing (in mM): 125 potassium aspartate, 1 MgCl, 10 KCl, 1CaCl, 10 HEPES, 2 EGTA, 4 ATP, 0.5 GTP, adjusted to pH 7.2 with KOH, adjusted to 273-279 mosm with potassium aspartate, and 0.04% Lucifer Yellow dye and 0.05% amphotericin (Sigma A9528). After establishing access, either the background was kept dark or rods were adapted down with a constant blue mean at 4000 Rh*/rod/sec. White noise current was injected with a 1000 Hz frequency cutoff and 500pA standard deviation with an upper and lower limit of ±200pA. The standard deviation was determined empirically to obtain a full input-

output function. The mean was at 0 pA unless holding current was required to keep spontaneous spiking less than 1 Hz and to keep the resting membrane potential at approximately -60mV.

To calculate the linear filter we followed Baccus and Meister (Baccus and Meister, 2002). Briefly the linear filter, F(t), was the correlation of the stimulus, s(t), and the response, rt, normalized by the autocorrelation of the stimulus. To then calculate the nonlinear response function, N(g), we convolved the stimulus with the linear filter, to get the generator potential g(t), which was then plotted against r(t), averaging over values of r over bins of g containing an equal number of points. Linear filters and nonlinearities from control and DTR conditions were compared by a permutation test (p-values reported in Figures 2.3 and 2.6).

Statistical analysis

In the histograms, medians are indicated by arrowheads. To identify significant differences between conditions, a Wilcoxon rank sum test (abbr. rank sum) was used for Figures 2.1-2.6, and a Wilcoxon sign rank test (abbr. sign rank) was used for paired data (Figure 2.7). A Permutation test was used to compare linear-nonlinear filters (Figures 2.3 and 2.6). The permutation test took the root mean squared difference between the average of the populations. This difference was compared to random chance by permuting the categories of cells to form two populations 10,000 times and calculating the root mean squared difference. The differences from the actual and permuted populations were compared to determine the p-values. All p values are indicated in the Results. Asterisks in Figures indicate the following p values: * ≤0.05, **≤0.01, ***≤0.005.

Key Resources Table

REAGENT or RESOURCE	SOURCE	IDENTIFIER
Antibodies		
Rabbit anti-Lucifer Yellow	Life Technologies	Cat# A5750;RRID:AB_1501344
Mouse monoclonal anti-CtBP2	BD Bioscience	Cat# 612044; RRID:AB_399431
Mouse monoclonal anti-PKCalpha	Sigma-Aldrich	Cat# P5704; RRID:AB_477375
Mouse monoclonal anti-SMI-32	Stenberger Monoclonals	Cat# SMI-32P; RRID: AB_2314912
Donkey polyclonal anti-rabbit-Alexa 488	Jackson Immunoresearch	Cat# 711-545-152; RRID:AB_2313584
Donkey polyclonal anti-sheep-Alexa 633	Molecular Probes	Cat# A21100; RRID:AB_10374307
Donkey polyclonal anti-mouse-Dylight 405	Jackson Immunoresearch	Cat# 715-475-150; RRID:AB_2340839
Donkey polyclonal anti-mouse-Alexa 647	Jackson Immunoresearch	Cat# 715-605-151; RRID:AB_2340863
Chemicals, Peptides, and Recombinant Proteins		
Normal Donkey Serum	Jackson Immunoresearch	Cat# NC9624464
Ames' Medium	United States Biological	Cat# A1372-25
Agarose, low gelling temperature Type VII A	Sigma Aldrich	Cat# A0701
Vectashield	Vector Laboratories	Cat# H-1000; RRID: AB_2336789
Experimental Models: Organisms/Strains		
Mouse model: *C57BL/6-Gt(ROSA)26Sortm1(HBEGF)Awai/J (DTR)*	The Jackson Laboratory	Cat# JAX:007900; RRID:IMSR_JAX:007900
Mouse model: *B6;SJL-Pde6b+ Tg(Rho-icre)1Ck/Boc (Rho-iCre)*	The Jackson Laboratory (Li et al., 2005)	Cat# JAX:015850 RRID: IMSR_JAX:015850

REAGENT or RESOURCE	SOURCE	IDENTIFIER
Mouse model: *B6.Cg-Gt(ROSA)26Sortm6(CAG-ZsGreen1)Hze/J (Ai6)*	The Jackson Laboratory	Cat# JAX:007906; RRID:IMSR_JAX:007906
Software and Algorithms		
ImageJ	NIH	https://imagej.nih.gov/ij/, RRID: SCR_003070
Amira	Thermo-Fisher Scientific	https://www.fei.com/software/amira-avizo/, RRID: SCR_014305
Imaris	Bitplane	http://www.bitplane.com/, RRID: SCR_007370
Matlab	Mathworks	https://www.mathworks.com/products/matlab.html, RRID: SCR_001622
Igor Pro	Igor Pro	RRID:SCR_000325
Object Finder	(Santina et al., 2013)	https://lucadellasantina.github.io/ObjectFinder/
Symphony and Stage	Mark Cafaro and Fred Rieke	https://github.com/Symphony-DAS/symphony-v1/wiki https://github.com/Stage-VSS/stage-v1

REFERENCES

Aït-Ali, N., Fridlich, R., Millet-Puel, G., Clérin, E., Delalande, F., Jaillard, C., Blond, F., Perrocheau, L., Reichman, S., Byrne, L.C., Olivier-Bandini, A., Bellalou, J., Moyse, E., Bouillaud, F., Nicol, X., Dalkara, D., van Dorsselaer, A., Sahel, J.-A., Léveillard, T., 2015. Rod-derived cone viability factor promotes cone survival by stimulating aerobic glycolysis. Cell 161, 817–832.

Baccus, S.A., Meister, M., 2002. Fast and slow contrast adaptation in retinal circuitry. Neuron 36, 909–919.

Beier, C., Hovhannisyan, A., Weiser, S., Kung, J., Lee, S., Yeong Lee, D., Huie, P., Dalal, R., Palanker, D., Sher, A., 2017. Deafferented adult rod bipolar cells create new synapses with photoreceptors to restore vision. Journal of Neuroscience 37, 4635–4644.

Bleckert, A., Schwartz, G.W., Turner, M.H., Rieke, F., Wong, R.O.L., 2014. Visual space is represented by nonmatching topographies of distinct mouse retinal ganglion cell types. Curr Biol. 24, 310-315

Buch, T., Heppner, F.L., Tertilt, C., Heinen, T.J.A.J., Kremer, M., Wunderlich, F.T., Jung, S., Waisman, A., 2005. A Cre-inducible diphtheria toxin receptor mediates cell lineage ablation after toxin administration. Nat Meth 2, 419–426.

Calvert, P.D., Krasnoperova, N.V., Lyubarsky, A.L., Isayama, T., Nicoló, M., Kosaras, B., Wong, G., Gannon, K.S., Margolskee, R.F., Sidman, R.L., Pugh, E.N., Makino, C.L., Lem, J., 2000. Phototransduction in transgenic mice after targeted deletion of the rod transducin alpha - subunit. Proc Natl Acad Sci USA 97, 13913–13918.

Care, R.A., Kastner, D.B., la Huerta, De, I., Pan, S., Khoche, A., Santina, Della, L., Gamlin, C., Santo Tomas, C., Ngo, J., Chen, A., Kuo, Y.-M., Ou, Y., Dunn, F.A., 2019. Partial cone loss triggers synapse-specific remodeling and spatial receptive field rearrangements in a mature retinal circuit. Cell Rep 27, 2171–2183.e5.

Dunn, F.A., Doan, T., Sampath, A.P., Rieke, F., 2006. Controlling the gain of rod-mediated signals in the Mammalian retina. Journal of Neuroscience 26, 3959–3970.

Enroth-Cugell, C., Freeman, A.W., 1987. The receptive-field spatial structure of cat retinal Y cells. J Physiol (Lond) 384, 49–79.

Haverkamp, S., Michalakis, S., Claes, E., Seeliger, M.W., Humphries, P., Biel, M., Feigenspan, A., 2006. Synaptic plasticity in CNGA3(-/-) mice: cone bipolar cells react on the missing cone input and form ectopic synapses with rods. Journal of Neuroscience 26, 5248–5255.

Hoshino, K., Pompeiano, O., 1977. Crossed responses of lateral vestibular neurons to macular labyrinthine stimulation. Brain Res 131, 152–157.

Jeon, C.J., Strettoi, E., Masland, R.H., 1998. The major cell populations of the mouse retina. J Neurosci 18, 8936–8946.

Kerschensteiner, D., Morgan, J.L., Parker, E.D., Lewis, R.M., Wong, R.O.L., 2009. Neurotransmission selectively regulates synapse formation in parallel circuits in vivo. Nature 460, 1016–1020.

Kim, K.J., Rieke, F., 2001. Temporal contrast adaptation in the input and output signals of salamander retinal ganglion cells. Journal of Neuroscience 21, 287–299.

Krieger, B., Qiao, M., Rousso, D.L., Sanes, J.R., Meister, M., 2017. Four alpha ganglion cell types in mouse retina: Function, structure, and molecular signatures. PLoS ONE 12, e0180091.

Lacour, M. and Xerri, C., 1981. Vestibular compensation: new perspectives. In H. Flohr and W. Precht (Eds.), Lesion-induced Neuronal Plasticity in Sensorimotor Systems, Springer, Berlin, pp, 240-253.

Li, S., Chen, D., Sauvé, Y., McCandless, J., Chen, Y.-J., Chen, C.-K., 2005. Rhodopsin-iCre transgenic mouse line for Cre-mediated rod-specific gene targeting. Genesis 41, 73–80.

Madisen, L., Zwingman, T.A., Sunkin, S.M., Oh, S.W., Zariwala, H.A., Gu, H., Ng, L.L., Palmiter, R.D., Hawrylycz, M.J., Jones, A.R., Lein, E.S., Zeng, H., 2009. A robust and high-throughput Cre reporting and characterization system for the whole mouse brain. Nat Neurosci 13, 133–140.

Marc, R.E., Jones, B.W., 2003. Retinal remodeling in inherited photoreceptor degenerations. Mol Neurobiol 28, 139–147.

Margolis, D.J., Detwiler, P.B., 2007. Different mechanisms generate maintained activity in ON and OFF retinal ganglion cells. Journal of Neuroscience 27, 5994–6005.

Margolis, D.J., Gartland, A.J., Singer, J.H., Detwiler, P.B., 2014. Network oscillations drive correlated spiking of ON and OFF ganglion cells in the rd1 mouse model of retinal degeneration. PLoS ONE 9, e86253.

Markham, C.H., Yagi, T., Curthoys, I.S., 1977. Contribution of contralateral labyrinth to 2nd order vestibular neuronal-activity in cat. Brain Res 138, 99–109.

Murphy, G.J., Rieke, F., 2006. Network variability limits stimulus-evoked spike timing precision in retinal ganglion cells. Neuron 52, 511–524.

Puthussery, T., Gayet-Primo, J., Pandey, S., Duvoisin, R.M., Taylor, W.R., 2009. Differential loss and preservation of glutamate receptor function in bipolar cells in the rd10 mouse model of retinitis pigmentosa. Eur J Neurosci 29, 1533–1542.

Putkonen, P.T., Courjon, J.H., Jeannerod, M., 1977. Compensation of postural effects of hemilabyrinthectomy in the cat. A sensory substitution process? Exp Brain Res 28, 249–257.

Ratnam, K., Carroll, J., Porco, T.C., Duncan, J.L., Roorda, A., 2013. Relationship between foveal cone structure and clinical measures of visual function in patients with inherited retinal degenerations. Invest Ophthalmol Vis Sci 54, 5836–5847.

Santina, Della, L., Inman, D.M., Lupien, C.B., Horner, P.J., Wong, R.O.L., 2013. Differential progression of structural and functional alterations in distinct retinal ganglion cell types in a mouse model of glaucoma. Journal of Neuroscience 33, 17444–17457.

Schaefer, K. P. and Meyer, D. L. (1974) Compensation of vestibular lesions. In H. H. Kornhuber (Ed.), Handbook of Sensory Physiology, Vestibular System, Part 2: Psychophysics, Applied Aspects and General Interpretations, Vol. 6/2, Springer, Berlin, pp. 463490.

Sher, A., Jones, B.W., Huie, P., Paulus, Y.M., Lavinsky, D., Leung, L.-S.S., Nomoto, H., Beier, C., Marc, R.E., Palanker, D., 2013. Restoration of retinal structure and function after selective photocoagulation. Journal of Neuroscience 33, 6800–6808.

Shimazu, H., Precht, W., 1966. Inhibition of central vestibular neurons from the contralateral labyrinth and its mediating pathway. J Neurophysiol 29, 467–492.

Soto, F., Ma, X., Cecil, J.L., Vo, B.Q., Culican, S.M., Kerschensteiner, D., 2012. Spontaneous activity promotes synapse formation in a cell-type-dependent manner in the developing retina. Journal of Neuroscience 32, 5426–5439.

Stasheff, S.F., 2008. Emergence of sustained spontaneous hyperactivity and temporary preservation of OFF responses in ganglion cells of the retinal degeneration (rd1) mouse. J Neurophysiol 99, 1408–1421.

Strettoi, E., Pignatelli, V., 2000. Modifications of retinal neurons in a mouse model of retinitis pigmentosa. Proc Natl Acad Sci USA 97, 11020–11025.

van Wyk, M., Wässle, H., Taylor, W.R., 2009. Receptive field properties of ON- and OFF-ganglion cells in the mouse retina. Vis Neurosci 26, 297–308.

Veruki, M.L., Hartveit, E., 2002. Electrical synapses mediate signal transmission in the rod pathway of the mammalian retina. Journal of Neuroscience 22, 10558–10566.

Villa, K.L., Berry, K.P., Subramanian, J., Cha, J.W., Oh, W.C., Kwon, H.-B., Kubota, Y., So, P.T.C., Nedivi, E., 2016. Inhibitory synapses are repeatedly assembled and removed at persistent sites in vivo. Neuron 89, 756–769.

CHAPTER 3: REMAINING QUESTIONS

Summary

In this final chapter, I discuss how the work presented in the previous two chapters taken together informs our understanding of input loss in the adult retina and in a broader context. Throughout, I outline questions that remain for future studies.

A unifying framework

This dissertation describes the effects of input loss on two pathways through a central nervous system circuit. By comparing the response of the retina to input loss incurred in each pathway, I arrive at principles which more broadly describe the nervous system's function.

One key difference between ablation of half of the rod population and ablation of half of the cone population is the resulting number of cells that die. As rods outnumber cones 10:1, loss of 50% of rods results in the loss of nearly half of the entire cell population of the retina, whereas loss of

50% of cones results in the loss of only 1-2% of the entire cell population of the retina (Jeon et al., 1998). Thus we can more generally interpret differences in the retina's response to partial input loss through the rod and cone pathways as a function of the amount of cell death.

The work in Chapters 1 and 2 shows that the adult retina mitigates the detrimental effects of input loss in both the rod and cone pathways. In both the rod and cone pathways, changes in inhibitory circuits drive this mitigation. One key difference in the retina's response to these two insults, however, is the location within the circuit that this mitigation occurs. In the sections below, I interpret my results through this framework.

Influence of input loss on inhibitory circuits

In Chapter 1, I showed that after partial cone loss, compensatory changes in the spatial receptive fields of $A_{ON\text{-}S}$ GCs are generated by an expansion of the receptive field of inhibitory currents onto these cells, a change which was not present after partial stimulation of the cone mosaic in control retina. In Chapter 2, I showed that after partial rod loss, compensation for decreased excitatory currents occurs at the level of the rod bipolar cell, where inhibitory currents also dramatically decrease and the voltage output is restored. While inhibitory circuits support the compensation that occurs after both cone loss and rod loss, the location in the circuit where inhibition changes differs between them. A number of differences between the cone pathway and the primary rod pathway may explain this difference. In killing half of the rods, we kill a large proportion of the cells in the retina, an insult which may be more readily detected than the loss of 1-2% of cells after partial cone death. Second, there is significantly greater convergence in the rod pathway, where 20-50 rods converge onto one rod bipolar cell, while only 2-6 cones converge onto one Type 6 cone bipolar cell. This pooling of inputs may enable the rod pathway to detect the decrease in rod input earlier in the

circuit than the cone pathway detects the decrease in cone input. Thirdly, inhibition is known to figure more prominently at cone light levels than at rod light levels, such that inhibition onto $A_{ON\text{-}S}$ GCs is more tuned to changes in the cone pathway than to changes in the rod pathway.

After both partial stimulation and partial death of rods, rod-mediated excitatory currents onto $A_{ON\text{-}S}$ GCs diminished significantly while inhibitory currents showed no significant changes in peak amplitude or charge. This suggests that inhibitory currents onto $A_{ON\text{-}S}$ GC are not as sensitive to rod loss as excitatory currents onto $A_{ON\text{-}S}$ GC. There could be several reasons for this. First, the inhibitory spatial surround is largely absent at rod light levels, meaning that inhibition of the $A_{ON\text{-}S}$ GC response at rod light levels is already minimal (Enroth-Cugell and Robson, 1966). A change in input in this regime would thus be expected to have a minimal effect. Furthermore, inhibition may be less spatially tuned than excitation, and thus generate a more all-or-nothing response, which is equally activated by both the half- and full-spot stimuli.

Interestingly, inhibitory currents onto rod bipolar cells, 70% of which come from reciprocal feedback via the A17 amacrine cell, were dramatically affected by input loss. This may be due to the largely reciprocal nature of inhibition onto rod bipolar cells, such that reduced excitatory input in turn elicits less inhibitory feedback.

In contrast, cone-mediated inhibitory currents onto $A_{ON\text{-}S}$ GCs were the source of the compensatory adjustments in spatial receptive field size that occur after cone death. They were affected in partial cone death, but not in partial stimulation of cones. Inhibition figures more prominently at cone light levels than at rod light levels, so it may be that inhibition's larger influence made changes more obvious. Alternatively, it may be that less cell loss in Cone-DTR retina means that detection of signaling changes does not occur until a deeper layer of the retina, i.e., at amacrine

cells rather than bipolar cells. This could also be compounded by the smaller degree to which convergence of photoreceptor signals occurs in the cone pathway.

One way to address this difference would be to expand the spectrum of assault on each pathway. The dose-dependence of the DTR system makes possible studies in which controlled fractions of photoreceptors are killed. We may expect to find certain mechanisms or location of compensation active only after a certain degree of input has been lost. We may also find that the timecourse of input loss influences which mechanisms are active. To more closely mimic input loss as it occurs in degenerative diseases, we could kill smaller fractions of photoreceptors over longer amounts of time and study how the timecourse of degeneration influences the activation of compensatory mechanisms.

Interdependence of cone and rod signaling

In both Rod-DTR and Cone-DTR systems, signaling through the unperturbed pathway remained intact (Figure 3.1). In Cone-DTR, changes in responses of $A_{ON\text{-}S}$ GCs occurred in amacrine cells that may not interface with the rod pathway, or may respond differently at cone and rod light levels. In Rod-DTR, homeostatic mechanisms within the rod bipolar cell mitigated rod loss, thus confining change to the primary rod pathway. However, there are at least two locations in the retinal circuit where rod and cone signals could interact: rod-cone electrical coupling, and the cone bipolar-to-ganglion cell synapse. How signaling through the secondary and tertiary rod pathways is affected after 50% rod loss remains unexplored. Additionally, the loss of rods has both direct and indirect effects on cones regardless of compensatory mechanisms that may occur downstream.

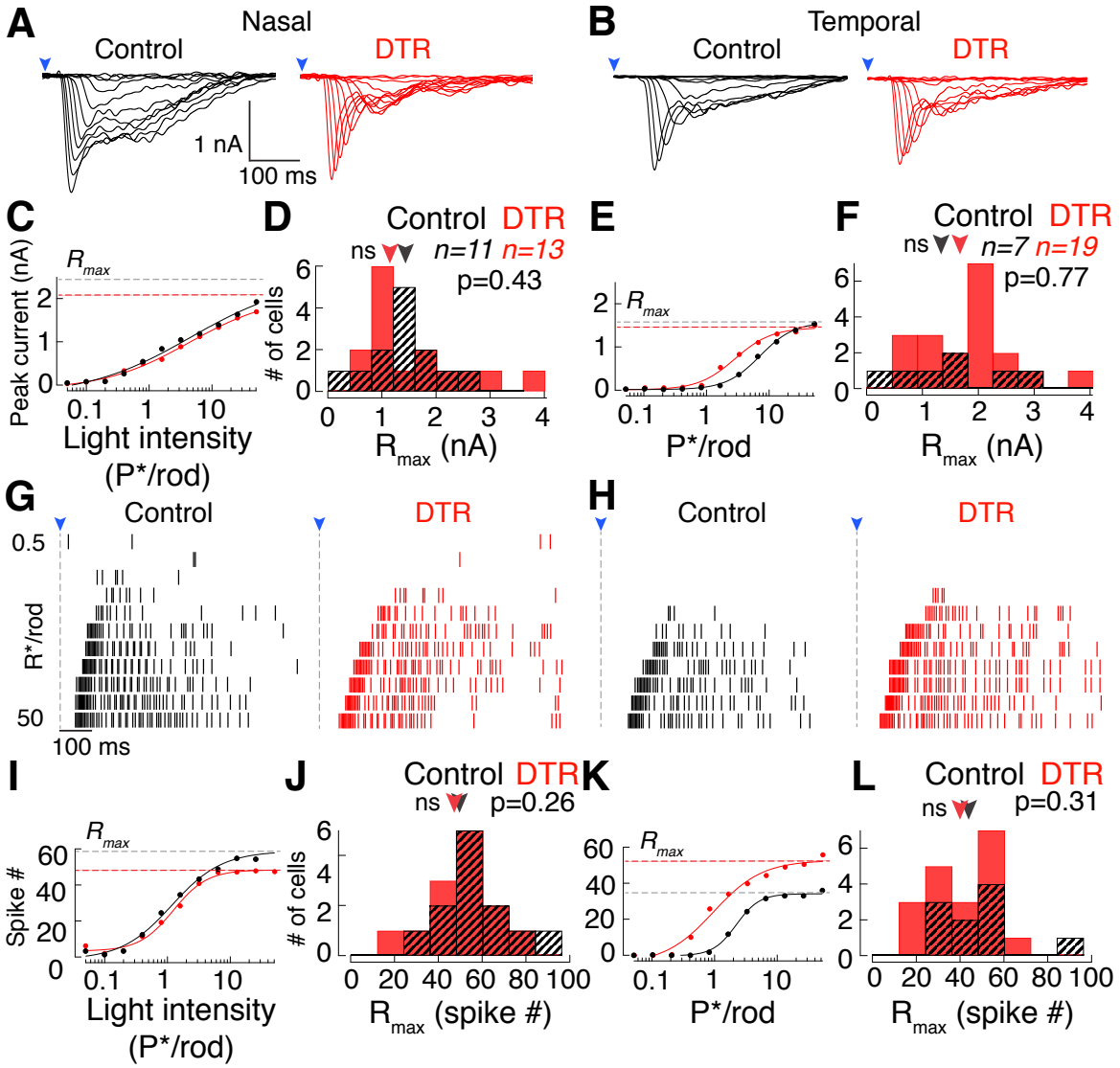

Figure 3.1. Rod-mediated excitatory input currents and output spikes are maintained across $A_{ON\text{-}S}$ ganglion cells after cone loss.

(A, B) Rod-mediated excitatory input currents in response to a 10ms pulse of blue light delivered from darkness at the time of the arrow. Flashes double in intensity from 0.5-50 Rh*/rod in control and DTR retina in (A) nasal and (B) temporal regions.

(C, E) Intensity-response functions of the peak amplitude of the rod-mediated excitatory currents for the examples in A and B. Points fit with a Hill equation. R_{max} defines the maximum current amplitude.

(D, F) Histograms of maximum excitatory current from the Hill equation fit (R_{max}) to each individual cell for control and DTR retina in (D) nasal and (F) temporal regions. Arrowheads indicate median. Rod-mediated maximum excitatory current response amplitudes are not significantly different between control and DTR conditions for either temporal or nasal retina (statistics in Results).

(G, H) Cell-attached rod-mediated spike responses of the same ganglion cell and stimulus in A, B.

(I, K) Intensity-response functions of the rod-mediated spike counts for the examples in G and H. Maximum number of spikes in the 600ms following the stimulus onset at each flash strength for the $A_{ON\text{-}S}$ ganglion cells from either (I) nasal or (K) temporal regions. Points fit with the Hill equation. R_{max} defines the maximum spike count.
(J, L) Histogram of maximum spike count from the Hill equation fit (R_{max}) to each individual cell for control and DTR retina in (J) nasal and (L) temporal regions.

The physical absence of dead rods impacts the cones to which they are coupled by gap junctions. The loss of coupled rods decreases the capacitance of remaining cones and likely increases their change in glutamate release per photon absorption. This increased gain may be a source of the increased cone-mediated signaling we observed in light responses from Rho-DTR retina, but not in light responses stimulated with the half-spot in control retina. Another possibility is that suppression of cones by rods via horizontal cells is alleviated after partial rod death. Horizontal cell somata receive inputs from both rods and cones via gap-junction coupling between rods and cones and feed this signal back onto cone photoreceptors to adjust cone gain to different light levels (Trümpler et al., 2008). A decrease in this signal due to the absence of rods may decrease the gain control on cones and result in more transmitter release from cones. Though we did not see a significant change in the photopic a-wave, which measures the output of cones, in Rho-DTR retina, the effect on cone signaling may be smaller than is resolvable with *in vivo* ERG.

The convergence of the rod and cone pathways at the cone bipolar axon terminal is another site at which cone signaling relies on rods. Cone bipolar axon terminals are electrically coupled to AII amacrine cells, which carry the rod-mediated light response from rod bipolar cells to ON cone bipolar cells and finally to ganglion cells. Changes in the resting potential of AIIs would correspondingly affect the resting potential in cone bipolar cell axon terminals and thus affect cone-mediated transmitter release at this synapse. It is of note that rod-mediated signaling was unaffected in Cone-DTR retina. Our manipulation showed no change in the density of synaptic puncta at the

cone bipolar-to-$A_{ON\text{-}S}$ GC synapse, which may spare the rod pathway which uses the same machinery. If a more severe manipulation did give rise to changes in these synaptic puncta, we would have the opportunity to observe whether physical changes in synapses shared by the rod and cone pathways cause bleedthrough of compensatory changes from one pathway into the other.

Relation to human disease

The work described in Chapter 1 stemmed partially from the finding that patients with a vast majority of cone photoreceptors absent from the fovea still see with decent acuity (Seiple et al., 1995; Rossi and Roorda, 2010; Ratnam et al., 2013). Unexplained were the mechanisms that enabled a many-fold reduction in cone density to generate passing acuity, and where those mechanisms were active. Similar to our approach with partial stimulation, studies in humans degraded the stimulus rather than the photoreceptor mosaic to tease apart innate circuit architecture and compensatory plasticity in the diseased retina (Green, 1968; Geller et al., 1992). They developed a prediction that patients with 50% cone loss should still have near 20/20 visual acuity due to mechanisms present within the retina. In reality, patients with more than 50% cone loss may also have excellent acuity, while other patients with less than 50% cone loss may have poor acuity. The sources of this variability remain unexplained. Below I will discuss the possible contributions of the degree of cell death and retinal subregions to this variability.

In the studies described in Chapter 1, I found a weak correlation between the density or number of cones remaining with a ganglion cell's receptive field and the magnitude of the cell's response, or the shape of the cell's spatial receptive field (Figure 3.2). Cells with fewer cones within their dendritic field sometimes had stronger cone-mediated responses than cells with more cones in their dendritic field. These results may indicate that ganglion cell responses are not linearly dependent on the

number of cone inputs they receive, in addition to compensation that may increase the magnitude of response when inputs are diminished. Furthermore, the responses of ganglion cells varied by spatial location within the retina, along similar axes which govern the size and dendritic overlap of these cells (Figure 3.3) (Bleckert et al., 2014). This variation suggests that ganglion cells may be highly tuned to precisely the arrangement of photoreceptors from which they receive input, and that there is more variability in this arrangement than previously appreciated.

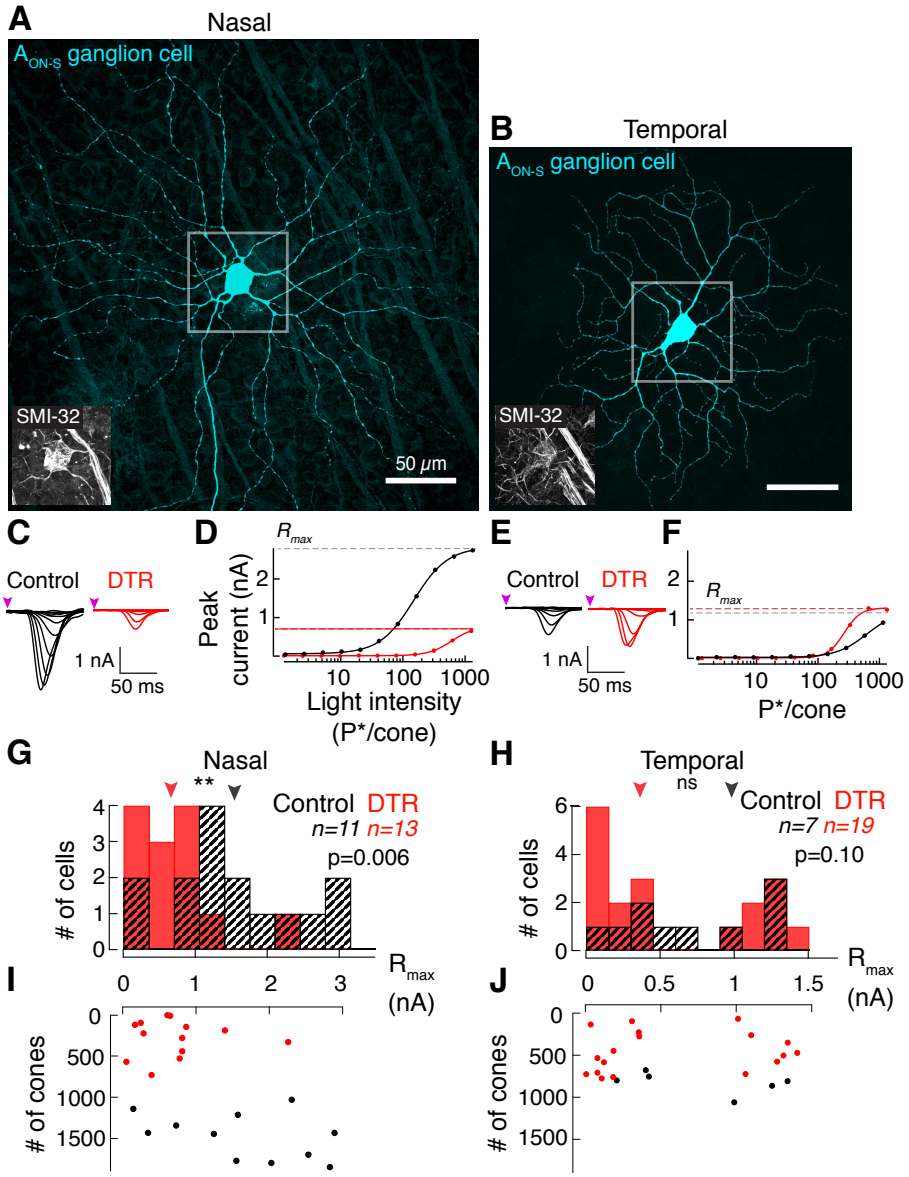

Figure 3.2. Cone-mediated excitatory input currents maintain amplitude in a subset of $A_{ON\text{-}S}$ ganglion cells after cone loss.
(A, B) Confocal images of $A_{ON\text{-}S}$ ganglion cells filled with Lucifer yellow dye during recording (cyan). Inset shows SMI-32 staining around the soma and primary dendrites (gray), which is unique to $A_{ON\text{-}S}$ ganglion cells in both (A) nasal and (B) temporal regions. Pictured cells are from control retina, but cells from DTR retina showed no morphological differences.
(C, E) Average excitatory current of $A_{ON\text{-}S}$ ganglion cells to a 10ms UV flash doubling in intensity from 1.5 to 1300 P*/S-cone delivered at the time marked by the purple arrow on top of a blue mean of 4000 rod isomerizations (Rh*) /rod/sec from control (black) and DTR (red) retina in (C) nasal and (E) temporal regions. Ganglion cells voltage clamped at -60mV.
(D, F) Peak excitatory current as a function of light intensity in isomerizations per S cone (P*/cone). Curves are from the best fit Hill equation (Base, Max, Rate, $I_{1/2}$ ± 95% confidence interval: Nasal control 61±8.7, 2826±20, 1.6±0.04, 148±2.4; Nasal DTR 11±1.7, 776±15, 2.3±0.08, 607±14; Temporal control 29.2±4.7, 1243±73, 1.74±0.12, 626±52; Temporal DTR: 15.7±12, 1312±27, 3.26±0.30, 267±9.0). R_{max} defines the maximum current amplitude.
(G, H) Histograms of maximum current amplitudes taken from the best fit Hill equation (R_{max}) in control (black) and DTR (red) retina in (G) nasal and (H) temporal regions. Arrowheads indicate median. In DTR retina, nasal large $A_{ON\text{-}S}$ ganglion cells are significantly different from control; whereas, on average, temporal small $A_{ON\text{-}S}$ ganglion cells are not significantly different from control (statistics in Results). Distribution shows that a subset of temporal $A_{ON\text{-}S}$ ganglion cells cannot recover currents; whereas another subset can recover currents.
(I, J) Maximum current amplitudes (R_{max}) plotted as a function of the number of cones within the dendritic field of the recorded ganglion cell for control and DTR retina in (I) nasal and (J) temporal regions.

The relationship between rod density and rod function in the human eye also remains unknown, due to the difficulty of imaging rods. We can begin to understand how cell density and function are related in our system, where rod death is dose-dependent upon Diphtheria toxin injected. Furthermore, the effect of the degree of cone loss on other more specialized retinal functions, such as direction selectivity and contrast sensitivity, has yet to be determined.

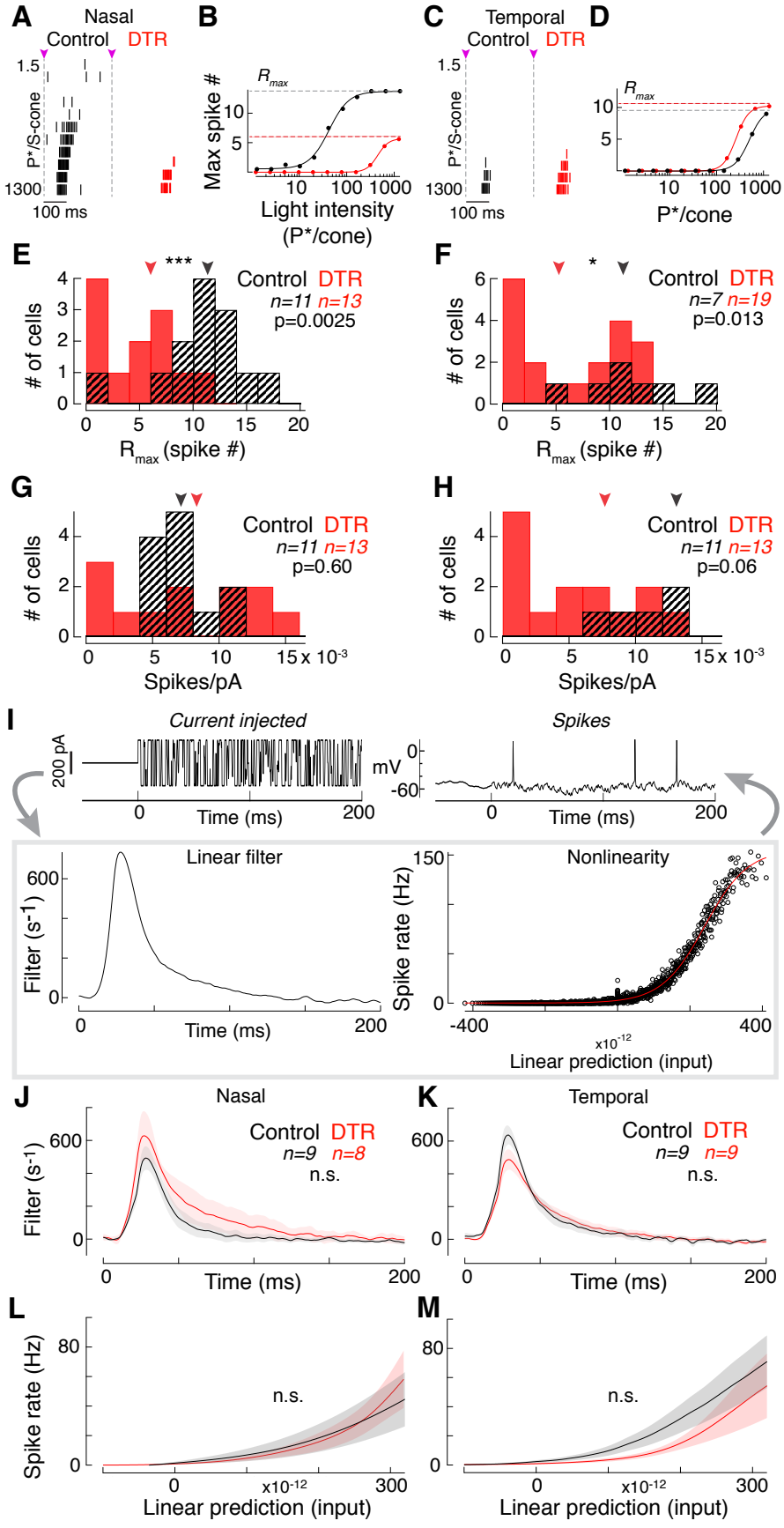
A
Nasal
Control DTR
1.5
P*/S-cone
1300
100 ms
B
Max spike #
R_{max}
10
5
10 100 1000
Light intensity
(P*/cone)
C
Temporal
Control DTR
1.5
P*/S-cone
1300
100 ms
D
R_{max}
10
5
10 100 1000
P*/cone
E
***
Control DTR
n=11 n=13
p=0.0025
# of cells
0 5 10 15 20
R_{max} (spike #)
F
*
Control DTR
n=7 n=19
p=0.013
# of cells
0 5 10 15 20
R_{max} (spike #)
G
Control DTR
n=11 n=13
p=0.60
# of cells
0 5 10 15 x 10-3
Spikes/pA
H
Control DTR
n=11 n=13
p=0.06
# of cells
0 5 10 15 x 10-3
Spikes/pA
I
Current injected
200 pA
0
Time (ms)
200
Spikes
mV
0
-60
0
Time (ms)
200
Linear filter
Filter (s-1)
600
0
0
Time (ms)
200
Nonlinearity
Spike rate (Hz)
150
0
-400
400
x10-12
Linear prediction (input)
J
Nasal
Control DTR
n=9 n=8
n.s.
Filter (s-1)
600
0
0
Time (ms)
200
K
Temporal
Control DTR
n=9 n=9
n.s.
600
0
0
Time (ms)
200
L
Spike rate (Hz)
80
0
n.s.
0
x10-12
300
Linear prediction (input)
M
80
0
n.s.
0
x10-12
300
Linear prediction (input)

Figure 3.3. $A_{ON\text{-}S}$ ganglion cells maintain intrinsic excitability after cone loss.
(A, C) Cell-attached spike responses to a 10ms UV flash doubling in intensity from 1.5 to 1300 P*/S-cone on top of a blue mean of 4000Rh*/rod/sec. Flash delivered at the time of the purple arrow. $A_{ON\text{-}S}$ ganglion cells are either from control or DTR retina in (A) nasal or (C) temporal regions.
(B, D) Maximum number of spikes in the 600ms following the stimulus onset at each flash strength for the $A_{ON\text{-}S}$ ganglion cells from either (B) nasal or (D) temporal regions. Points fit with the Hill equation (Base, Max, Rate, $I_{1/2}$ ± 95% confidence interval: Nasal control 0.55±0.23, 13.7±0.23, 2.1±0.21, 42±2.3; Nasal DTR -0.01±0.02, 5.72±0.05, 3.7±0.1, 449±5.1; Temporal control -0.03±0.04, 9.9±0.24, 2.8±0.16, 502±14; Temporal DTR: -0.03±0.04, 10.3±0.08, 3.2±0.11, 260±3.4). R_{max} defines the maximum spike count.
(E, F) Histograms of maximum responses from the Hill equation fits (R_{max}) for all $A_{ON\text{-}S}$ ganglion cells from either control or DTR retina in (E) nasal or (F) temporal regions. Arrowheads indicate median. Statistics in Results.
(G, H) Histograms of the ratio between maximum spikes and currents from the Hill equation fits (R_{max}) for all $A_{ON\text{-}S}$ ganglion cells from control or DTR retina in (G) nasal or (H) temporal regions.
(I) Test of intrinsic excitability. Example of current injected through the patch pipette (left) and the resulting spikes (right). Blue mean of 4000Rh*/rod/sec was applied to adapt rods during the duration of the current injections, which were 40 sec epochs ≥ 6 repeats. (box) Time-reversed spike-triggered average (left in box) and the nonlinearity for the example cell (right in box). Nonlinearity fit with a sigmoid function (red).
(J-M) (J, K) Time-reversed spike-triggered average and (L, M) average nonlinearity of the linear-nonlinear model calculated from spike responses to white noise current injections (mean±SEM). For the nonlinearity, abscissa represents the convolution between the spike-triggered average and the stimulus in units of standard deviation, i.e., generator potential. Ordinate represents the spike rate. The nonlinearity for each cell was interpolated and smoothed with a spline function. $A_{ON\text{-}S}$ ganglion cells from either (J, L) nasal or (K, M) temporal regions.

Opportunity to uncover salient features of the neural code

In the studies described here, the ganglion cell responses are not exactly the same in control and DTR conditions. In Rho-DTR retina, some parameters of the response are unchanged from control while others differ significantly. For example, the charge of the excitatory current response was predictive of the spike response, which was slightly smaller than control, while the peak amplitude of the excitatory currents was unchanged compared to control. Interestingly, in the half-spot experiment, the opposite held true: the peak amplitude of the excitatory currents was predictive of the spike response, while the charge of the excitatory currents was unchanged compared to full-spot stimulation. In the translation of currents to spikes, the peak amplitude of the current may

correspond to the highest spike rate in the response, while the charge of the current may correspond to the duration of the spike response. It could be that the peak amplitude of the current response is more sensitive to the number of inputs than the charge of the current response is, and is thus affected first when input decreases. In Rho-DTR retina, compensatory mechanisms may restore the excitatory current peak amplitude, perhaps at the cost of the charge of the response. This may indicate that the peak amplitude of the excitatory current, and therefore the highest spike rate of the spike response, is the more salient feature of the rod-mediated light response.

In Cone-DTR, spatial receptive fields take on features that might be considered more optimal (Atick and Redlich, 1990) in lower cone density conditions than in control conditions. However, the ratio of center to surround magnitude remains unchanged. In some cases, the center-surround structure degrades. Different recovery conditions, i.e., in light vs. in darkness, may help uncover efficacy of different compensatory mechanisms at restoring salient aspects of the neural code. Understanding how these responses are interpreted in further stations of visual processing is beyond the scope of this work but provides an interesting opportunity to uncover the salient features of the neural code that carries information to the rest of the brain. This information would in turn inform the development of prostheses that aim to restore vision.

REFERENCES

Atick, J.J., Redlich, A.N., 1990. Towards a theory of early visual processing. Neural computation 2, 308–320.

Bleckert, A., Schwartz, G.W., Turner, M.H., Rieke, F., Wong, R.O.L., 2014. Visual space is represented by nonmatching topographies of distinct mouse retinal ganglion cell types. Curr Biol. 24, 310-315.

Enroth-Cugell, C., Robson, J.G., 1966. The contrast sensitivity of retinal ganglion cells of the cat. J Physiol (Lond) 187, 517–552.

Geller, A.M., Sieving, P.A., Green, D.G., 1992. Effect on grating identification of sampling with degenerate arrays. Journal of the Optical Society of America A, Optics and image science 9, 472–477.

Green, D.G., 1968. The contrast sensitivity of the colour mechanisms of the human eye. J Physiol (Lond) 196, 415–429.

Jeon, C.J., Strettoi, E., Masland, R.H., 1998. The major cell populations of the mouse retina. J Neurosci 18, 8936–8946.

Ratnam, K., Carroll, J., Porco, T.C., Duncan, J.L., Roorda, A., 2013. Relationship between foveal cone structure and clinical measures of visual function in patients with inherited retinal degenerations. Invest Ophthalmol Vis Sci 54, 5836–5847.

Rossi, E.A., Roorda, A., 2010. The relationship between visual resolution and cone spacing in the human fovea. Nat Neurosci 13, 156–157.

Seiple, W., Holopigian, K., Szlyk, J.P., Greenstein, V.C., 1995. The effects of random element loss on letter identification: implications for visual acuity loss in patients with retinitis pigmentosa. Vision Res 35, 2057–2066.

Trümpler, J., Dedek, K., Schubert, T., de Sevilla Müller, L.P., Seeliger, M., Humphries, P., Biel, M., Weiler, R., 2008. Rod and cone contributions to horizontal cell light responses in the mouse retina. Journal of Neuroscience 28, 6818–6825.

Publishing Agreement

It is the policy of the University to encourage the distribution of all theses, dissertations, and manuscripts. Copies of all UCSF theses, dissertations, and manuscripts will be routed to the library via the Graduate Division. The library will make all theses, dissertations, and manuscripts accessible to the public and will preserve these to the best of their abilities, in perpetuity.

Please sign the following statement:

I hereby grant permission to the Graduate Division of the University of California, San Francisco to release copies of my thesis, dissertation, or manuscript to the Campus Library to provide access and preservation, in whole or in part, in perpetuity.

Author Signature

8.28.2019
Date